On-Site 3D LPT for Automotive Underbody Aerodynamics

3D Lagrangian Particle Tracking using the Ring of Fire

Coen Holland

Delft University of Technology

TU Delft

On-Site 3D LPT for Automotive Underbody Aerodynamics

3D Lagrangian Particle Tracking using the Ring of Fire

by

Coen Holland

Supervisor:	Dr. ir. A. Sciacchitano
Daily Supervisor:	Ir. A. Grille Guerra
Institution:	Delft University of Technology
Faculty:	Faculty of Aerospace Engineering
Project Duration:	May, 2024 - March, 2025

Cover: Renault Sport F1 Team R.S. 18, Singapore GP 2018

TU Delft

Preface

This thesis is the final piece of work produced in my pursuit to obtain my master's degree in Aerodynamics at the Delft University of Technology. It shows the result of a project that I started in May 2024, lead me to an experimental campaign in September and the final writing of this thesis document, ending now in March 2025. Starting all the way back in 2017, I have certainly had an eventful number of years, and I feel proud of all the things that I have achieved in those years.

With my passion for race car aerodynamics, as well as the joy of doing things in a practical manner, picking up the project based on the work done by Andrea Battegazzore before me could not have been more suiting. Preparing for the experimental campaign, in all its details ranging from designing the car bodywork and test driving the car, to buying sand and leveling the not very smooth road was something I truly enjoyed doing.

I am very grateful to my supervisor Andrea Sciacchitano, to suggest the topic to me, and for making it into a thesis opportunity. I learned a lot from our weekly update meetings, where you were always able to understand and help me with my questions, suggest new ways to look at results, and keep me on-track when I needed to focus on the right things.
Secondly, a big thanks goes to Adrian Grille Guerra, being my daily support/supervisor. It was so nice to be able to ask you any question I might have, and for teaching me about 3D LPT. Your support was invaluable before, during and after the experiment, and I admire the way you manage things in a efficient and orderly way.
Thirdly, I want to thank Luuk, for the countless times we talked over a *bakkie*, almost on a daily basis. Your extra viewpoint and practical experience with the setup was very much appreciated, and I could count you almost as a second daily supervisor. I'm sure your PhD will be 2 more years of hard but useful work, and I'm curious to see where you will end up after your time in Delft. As we did most of our Bachelors degree as friends together, being able to share some time again during my thesis was very enjoyable.
I cannot forget to thank Kaj for his support during the experimental campaign, and in general for being such a good friend during my whole TU Delft career. You have kept amazing me all those years with the apparent ease at which you tackle any problem, project or assignment, and I'm happy to see you continuing in that in your PhD.

Having spend all these months at the HSL, I need to thank all of the PhD students of the high speed lab for the intersting discussions we had during lunch time, quick chats and inviting me for game nights. I enjoyed your company, as you provided me with some much appreciated social interactions outside the HSL basement.

Finally, I need to thank both of my parents, as well as my sister. Pap en mam, jullie vertrouwen en steun hebben mij de vrijheid gegeven om alle dingen te doen die ik tijdens mijn studie kunnen doen. Ik ben echt heel dankbaar voor de mogelijkheden die jullie mij hebben geboden, waardoor ik nu sta waar ik sta. Dan Noor, ik kan mij geen Delft voorstellen zonder jou. Het was zo fijn om altijd een zus in de buurt te hebben, en ik ben erg blij dat we deze tijden met elkaar hebben kunnen delen!

Coen Holland
Delft, March 2025

Abstract

This thesis presents an innovative approach to investigating automotive underbody aerodynamics through the development and application of an on-site 3D Lagrangian Particle Tracking (LPT) system. Automotive performance, particularly in high-speed racing applications, is significantly influenced by the aerodynamic efficiency of vehicle diffusers. The work addresses the challenges associated with accurately capturing complex three-dimensional flow structures beneath a moving vehicle, where traditional flow measurement techniques struggle to capture underbody flows, especially in an experimental setting.

The research builds upon a previous study on a diffuser equipped radio-controlled car, which uses a measurement technique known as the Ring of Fire. By improving the camera setup, as well as creating better seeding and illumination, the setup allowed for successful particle tracking of neutrally buoyant Helium Filled Soap Bubbles underneath a car model, driving at around 7.5 m/s. The particle tracks captured in a measurement domain the size of (300 x 150 x 200) mm^3 allow for the reconstruction of a velocity field around three tested car geometries, by combining data from multiple runs of the car driving through the measurement domain. These geometries are a flat floor car model, a car model fitted with a 15° planar diffuser, and a car model with the same diffuser, but also an additional strip of vortex generator fins placed ahead of the diffuser leading edge.

Using a pressure gradient integration method, a pressure field around the car models was obtained. Looking at both the velocity and pressure distribution around the models, the setup was able to capture the difference in peak velocity underneath the car, where the diffuser equipped model showed a maximum velocity of around 1.4 times the freestream velocity. Velocity and pressure coefficient profiles measured along the car's centerline closely match those reported in the literature, confirming that the diffuser primarily impacts the rear region of the vehicle.

Streamwise vortices introduced into the diffuser by the vortex generator strip showed to be primarily moving high momentum flow closer to the diffuser surface, while potentially resolving a laminar separation bubble near the diffuser leading edge, observed for the plain diffuser case.

Difference in local velocity magnitude and pressure coefficient measured at the diffuser leading edge between the flat floor and diffuser equipped models proved to be large enough to be statistically significant. An estimated 25 runs was needed to reach a velocity convergence inside the diffuser within 1% of the mean car velocity, where only 4 or 5 runs would be enough for the flat floor regions upstream of the diffuser.

This work shows the improvement made to the Ring of Fire setup developed to measure on-site automotive underbody aerodynamics. It proves the capabilities of applying 3D LPT to quantify underbody flows, and the potential to apply this setup on larger and faster vehicles.

Contents

List of Figures

List of Tables

List of Abbreviations

Abbreviation	Description
CFD	Computational Fluid Dynamics
F1	Formula One
FoV	Field of View
HFSB	Helium-Filled Soap Bubbles
LE	Leading Edge
LPT	Lagranian Particle Tracking
OTF	Optical Transfer Function
PIV	Particle Image Velocimetry
POI	Points of Interest
ppp	particles per pixel
PTV	Particle Tracking Velocimetry
RC	Radio-controlled
RoF	Ring of Fire
STB	Shake-The-Box
STD	Standard Deviation
TE	Trailing Edge
Tomo-PIV	Tomographic Particle Image Velocimetry
VG	Vortex Generator

List of Symbols

Notation	Description	Unit
C_L	Lift coefficient	[-]
C_P	Pressure coefficient	[-]
C_r	Relative convergence of the mean velocity	[-]
D	Drag force	$[N]$
L	Lift force	$[N]$
L_B	Flat floor model length	[mm]
N	Number of independent samples	[-]
Np_{avg}	Average number of particles per bin per run	[-]
Np_{total}	Total number of particles per bin for all runs	[-]
Q	Q criterion	$[1/s^2]$
U_∞	Free stream velocity	$[m/s]$
Δt	timestep length	$[ms]$
$\epsilon_{\bar{u}}$	Standard random uncertainty of the mean velocity	$[m/s]$
ν	Kinematic viscosity	$[m^2/s]$
ω_x	Streamwise vorticity	$[1/s]$
ρ_∞	Free stream air density	$[kg/m^3]$
σ_u	Standard deviation of the mean velocity	$[m/s]$
σ_{C_P}	Standard uncertainty of the pressure coefficient	[-]
σ_{mean}	Standard deviation of mean velocities inside a bin	$[m/s]$
$\mathbf{v}'(t)$	Particle velocity in lab reference frame	$[m/s]$
$\mathbf{v}(t)$	Particle velocity in car reference frame	$[m/s]$
$\mathbf{v}_{car}$	Car model velocity vector	$[m/s]$
$\mathbf{x}'(t)$	Particle position in lab reference frame	$[m/s]$
$\mathbf{x}'_{car-origin}$	Car origin marker at t_{ref}	$[m]$
$\mathbf{x}(t)$	Particle position in car reference frame	$[m/s]$
θ	Diffuser angle	$[^\circ]$
d	Diffuser half width	$[m]$
f	Focal lenght	[-]
$f_\#$	F-stop, lens aperture	[-]
f_{acq}	Acquisition frequency	[kHz]
h	Ride height	$[m]$
n	Number of particles per bin	[-]
p	Static pressure	$[Pa]$
p_∞	Free stream static pressure	$[Pa]$
r_{max}	Total number of runs per geometry	[-]
t_{ref}	Reference timestep of car origin marker	$[s]$
u	Local velocity in x-direction	$[m/s]$
u/U_∞	Normalized streamwise velocity	[-]
u_{tot}/U_∞	Normalized velocity magnitude	[-]

1. Introduction

Automotive aerodynamics plays a crucial role in vehicle performance, influencing efficiency, stability, and handling. In motorsport and high-performance vehicle design, aerodynamic optimization is primarily focused on reducing drag and generating downforce to enhance cornering capabilities [1]. By manipulating airflow around the car, engineers can improve grip without increasing vehicle weight, leading to higher speeds through corners and better overall performance [2].

Studies performed on diffuser aerodynamics have led to the identification of several performance factors that contribute to the working of an automotive diffuser. These factors are variables such as vehicle ride height, diffuser angle and the presence of streamwise vortices, originating from the diffuser sidewalls. Even without a diffuser, a flat floor car model will generate a low pressure region under its body when in close proximity to the ground. Air is forced under the car, accelerated at the floor leading edge due to the reduced streamtube height, lowering static pressure, as per Bernoulli's principle. When a diffuser is added to the rear of the body, the flow is allowed to expand (over the length of the diffuser) and increase in static pressure to the base pressure behind the body. This allows for a lower static pressure, compared to a flat floor model, at the diffuser leading edge, the so called diffuser pumping effect [3].

The diffuser angle, ride height, as well as the strength of streamwise vortices are of importance in determining the maximum downforce produced by the diffuser, as shown by for example Cooper et al., Senior and George [4–6]. Figure 1.1 below shows the effect of changing diffuser angle on the local pressure coefficient around a bluff body.

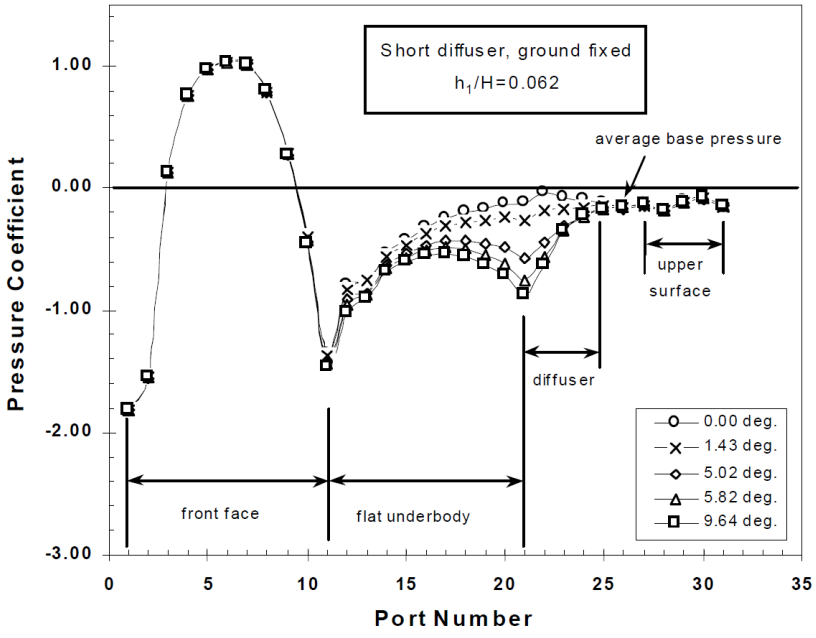

Figure 1.1: The effect of increasing diffuser angle on C_P around a bluff body [4]

Understanding and measuring the flow inside a diffuser is currently mostly done using a multitude of flow measurement techniques. Computational Fluid Dynamics is able to model the full 3D flow field around a car, but require a trade-off between modeling accuracy and computational cost. This is why much of the engineering on race cars is still being done in a combination of CFD and windtunnel testing. The wind tunnel testing can serve as a validation tool to CFD, as well as a source of flow measurements itself. Among the experimental

techniques, force balance and pressure tap measurements are most common ways of measuring aerodynamic performance. These techniques can give a good indication of the performance of a diffuser equipped body as a whole, however do not give direct measurements of the underlying flow structures and interactions that cause a certain diffuser geometry to perform the way it does.

Particle Image Velocimetry (PIV) is a method that can capture velocity field data in a 2D plane or even a 3D volume. PIV enables the visualization of velocity fields and vortex structures, allowing for direct comparisons with CFD simulations. However, its application in automotive aerodynamics, particularly underbody flows, is often constrained by limited optical access. Transparent diffuser sidewalls and specialized laser-sheet arrangements have been employed to overcome these challenges, yet practical limitations still exist.

3D PIV, or so-called Tomographic PIV, reconstructs particle positions based on 2D images and then relies on the cross-correlation of interrogation volumes within the measurement domain to obtain a velocity field. These interrogation volumes then produce a spatially averaged velocity vector per volume. With increasing measurement volumes, this technique becomes computationally expensive, and requires large amounts of data to be processed [7]. Individual particle tracking has been used for quite some years, but have become more and more popular with the introduction of the Shake-The-Box algorithm [7]. This allows for 3D particle tracking velocimetry (PTV) in large measurement volumes, at relatively high particle densities (in the order of 0.1 particles per pixel). 3D PTV has been applied as an on-site measurement technique for several applications, such as ice skating, cycling, and automotive aerodynamics, in the so-called Ring of Fire (RoF) setup [8]. The RoF has been used by Battegazzore [9] to perform 3D LPT on the flow underneath a radio-controlled (RC) diffuser equipped car model. By using a subterranean camera and illumination setup, Battegazzore was able to measure the difference in underbody velocity between diffuser angles, and capture flow separation at higher diffuser angle. Figure 1.2 below shows some of the results from the data captured using the on-site 3D LPT setup designed by Battegazzore.

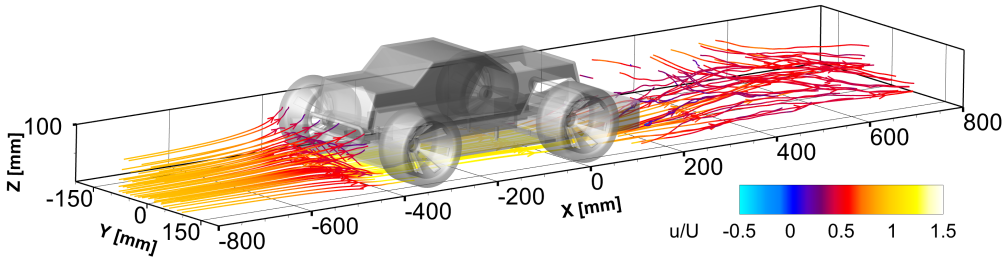

Figure 1.2: Streamlines from the flow around a 15° diffuser equipped car model, captured using on-site 3D LPT by Battegazzore [9]

This thesis project is aimed at further developing the on-site 3D LPT technique introduced by Battegazzore. Main goals are to improve the particle tracking capabilities of the setup, create better seeding distribution around the model and improve the aerodynamic performance of the diffusers in the model. Using the data captured by the RoF setup, this study aims to demonstrate the system's capabilities by addressing key questions related to the performance of automotive diffusers in ground effect.

This thesis is structured as follows: chapter 2 provides an overview of automotive aerodynamics, with a focus on underbody flows and diffusers. Chapter 3 discusses various flow measurement techniques used in diffuser research, leading to the motivation for using on-site 3D Lagrangian Particle Tracking (LPT). Chapter 4 presents the research objectives and questions. The experimental setup and methodology, including improvements to the Ring of Fire system, are detailed in chapter 5. Chapter 6 outlines the data processing techniques applied to extract velocity and pressure fields. Chapter 7 presents the results, including velocity distributions, pressure fields, and data uncertainty analysis. Finally, chapter 8 concludes the study, summarizing key findings and offering recommendations for future improvements.

2. Automotive Aerodynamics

This chapter will go over the interest and development of automotive aerodynamics in motorsport. Some more attention will be given to underbody aerodynamics, with a specific focus on diffuser equipped bluff bodies in ground effect.

2.1 Downforce on race cars

Within a motorsport setting, automotive aerodynamics have been of interest for some time now. In order to maximize performance of race cars, designers/engineers use aerodynamic devices such as wings, splitters, diffusers, etc. These devices are used to create negative lift, or downforce, which increases the grip a car has going around a circuit. As the downforce generates extra normal force on the tires of a car, the total grip can be increased, without increasing the vehicles weight. The effect of this increased grip is that a car can go around corners faster, as the tires are able to tolerate higher lateral loads [1]. With the ultimate goal of decreasing lap time, this is a direct benefit to a race car's performance. The effect of adding downforce to a racecar is illustrated by the following figure 2.1 below:

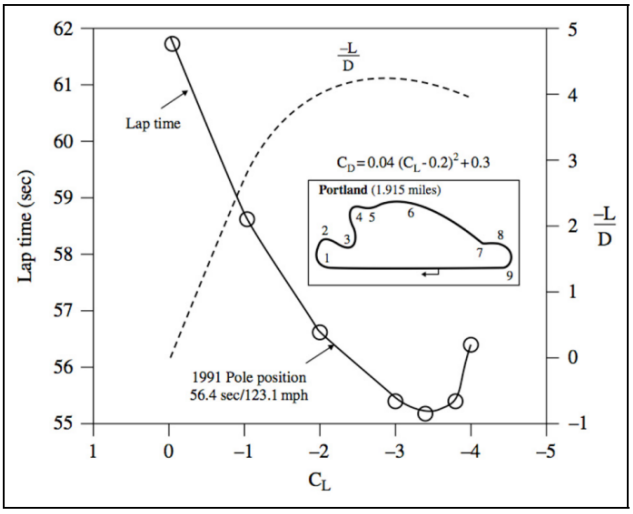

Figure 2.1: Relation between laptimes and downforce for a prototype car around the Portland Circuit, USA [10]

Figure 2.1 shows the improvement in laptime (i.e. a shorter time to cover the length of the circuit) when increasing the -C_L of a car. More important however is the fact that there is a certain point (around $C_l = -3.4$) after which there is no more improvement in adding downforce to the car in order to gain laptime. This is caused by the induced drag (from the added downforce on the car) negating the effects of adding even more downforce. There is a maximum aerodynamic efficiency ($\frac{-L}{D}$) point for which the laptime around this particular circuit is minimized. This aerodynamic efficiency point is the trade-off between straight line speed (hindered by drag, which is added with more downforce) and cornering speed. Hence, it is important to realize that one must not only try and maximize pure downforce, but also keep in mind the efficiency in which the downforce is being generated.

Within motorsport, Formula One is a very well known example of the application of automotive aerodynamics as one of the tools to maximize a racecars performance. Within the Formula One regulations, engineers have certain sections or assemblies of the car that produce downforce. An overview of the different parts generating downforce on a 2009 Formula One car are given by Toet (2013) [2], and summarized in figure 2.2.

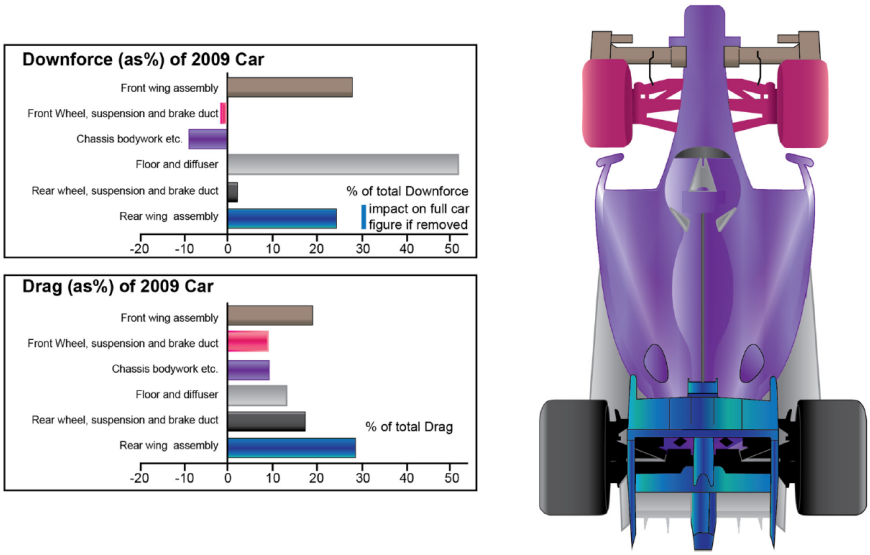

Figure 2.2: Downforce and Drag component breakdown of 2009 F1 car [2]

The main takeaway from figure 2.2 is that the floor and diffuser assembly generates over 50% of the total car downforce, but only account for about 15% of the drag of the vehicle. This is very efficient compared to the front and rear wing assemblies, which combined are also producing about 50% of the downforce, but adding about 3 times the amount of drag. Naturally, this makes the floor and diffuser area an interesting topic of research, as it is a "cheap" way of producing significant downforce.

2.2 Automotive diffusers in ground effect

In order to study the flow physics and behavior of automotive diffusers, usually a variation of the so called Ahmed body is studied [11]. To study the effect of a diffuser equipped on a bluff body, it is common to consider a "simple" plane walled single-plane-expansion diffuser fitted to a Ahmed like body. An example of such a body is shown in figure 2.3, with a flat floor and a rear diffuser at angle θ.

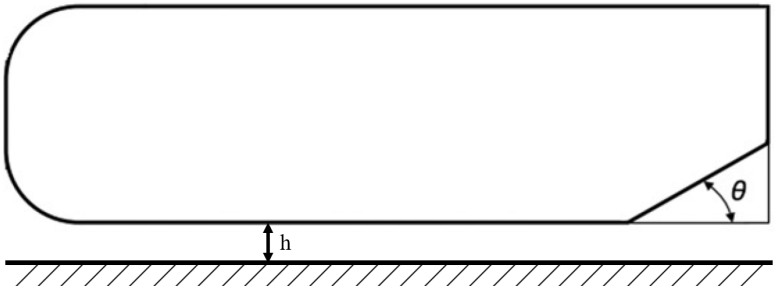

Figure 2.3: Sideview of a diffuser equipped Ahmed body with diffuser angle θ and ride height h

One of the driving mechanisms in the downforce generated by such a body is the so called ground effect, driven by Bernoulli's principle. As the body is placed at a height h above the ground/road surface, air is being forced from the front of the body into the narrow section of flat floor under the model, which, considering inviscid flow theory, leads to an acceleration of the flow under the car/model. In an inviscid quasi 1D case, this increase in velocity will directly lead to a decrease in static pressure through Bernoulli's principle. As h is reduced, velocity goes up, and static pressure keeps dropping, in turn increasing downforce. In the limit of h going to 0, this would lead to infinite downforce, however in reality viscous effects limit the acceleration of the

flow under the body when "ride" height h becomes small, and other 3D effects such as in or outflow also affect the maximum downforce generated by the body.

The addition to the flat floor section, the upsweeping diffuser section at the end of the Ahmed body from figure 2.3 introduces 2 other flow mechanisms which drive the downforce generation of the body. The first one is the diffuser pumping effect, first mentioned by Sovran in 1994 [3]. It describes the effect generated by the expanding area of the diffuser in the streamwise direction. As the area increases, and the flow is subsonic, the flow will decelerate, increasing its static pressure, until it has reached the base pressure which is close to the freestream pressure, behind the body at the exit of the diffuser. This in turn means that when looking upstream, if the pressure at the diffuser exit is at or around base pressure, the pressure must be lower at the diffuser leading edge, if the flow is attached. This makes the diffuser act as a "pump" to draw more air under the body compared to when there would be no diffuser.

Secondly, the added camber from the diffuser upsweep is a small mechanism that adds downforce to the body, in the same way as a cambered airfoil generates a lift component compared to a symmetric airfoil.

2.3 Typical C_P distribution for planar diffusers

A typical pressure distribution on the centerline of a diffuser equipped body is presented in figure 2.4 [12]. The pressure distribution is expressed in terms of the pressure coefficient C_P, which is defined in equation 2.1. Using Bernoulli's equation and applied in a potential flow, equation 2.1 can be rewritten to equation 2.2.

$$C_P = \frac{p - p_\infty}{\frac{1}{2}\rho_\infty U_\infty^2} \tag{2.1}$$

or

$$C_P = 1 - \left(\frac{u}{U_\infty}\right)^2 \tag{2.2}$$

Figure 2.4 shows the stagnation of the flow at the body's leading edge, where the C_P is equal to 1. Then the flow is accelerated under the floor, around the nose curvature, leading to the first pressure peak (in a negative sense). After that, there is a slight pressure recovery phase, until the flow is accelerated again at the diffuser inlet, leading to the second pressure peak. The pressure recovery phase between the floor leading edge and the diffuser leading edge is not very well described in literature, and is highly dependent on factors such as vehicle ride height, as shown by Cooper [4]. 3D flow effects such as spanwise in or outflow, the width of the body, the presence of front tires (and their wake) all influence this region. Throughout the diffuser length, the pressure rises with the increasing diffuser area, up until the base pressure behind the body, where the C_P goes towards 0.

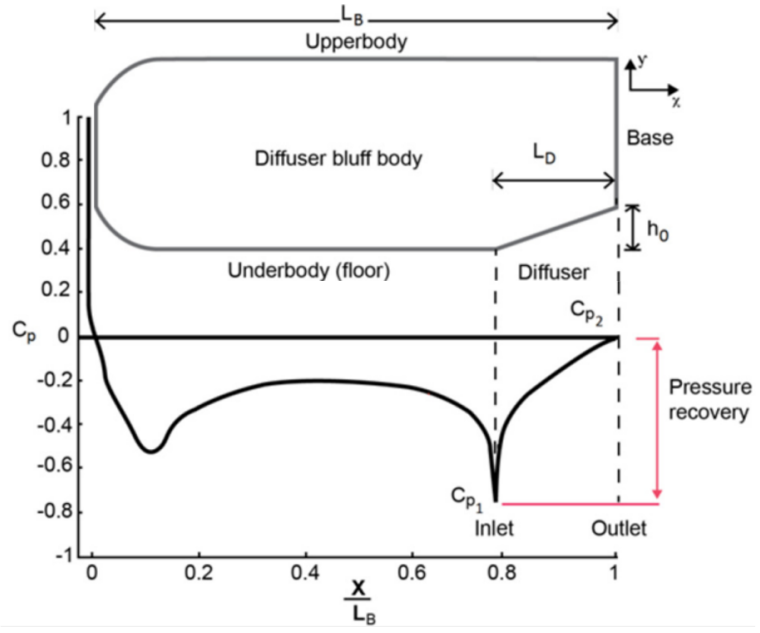

Figure 2.4: Typical pressure distribution on diffuser equipped bluff body [12]

Cooper et al. tested single plane diffusers at angles ranging from 0° (No diffuser, flat floor) to 9.64° on an Ahmed body in a windtunnel, and found similar results in terms of C_P distribution on the model centerline compared to figure 2.4[4]. The effect of increasing the diffuser angle is shown in figure 2.5. The diffuser introduces a clear second suction peak at its inlet, with increasing strength at higher diffuser angles, compared to a fully flat model $\theta = 0°$. There is little change in the pressure distribution on the forward part of the body, for example on the stagnation point of the body leading edge. This suggests that the diffuser doesn't affect flow upstream as much, and the amount of air being forced under the floor from the front of the body isn't changing much with adding a diffuser. The earlier mentioned diffuser pumping effect would be more related to air being drawn under the flat floor section laterally, instead of an increase in streamtube ingestion from the front of the body.

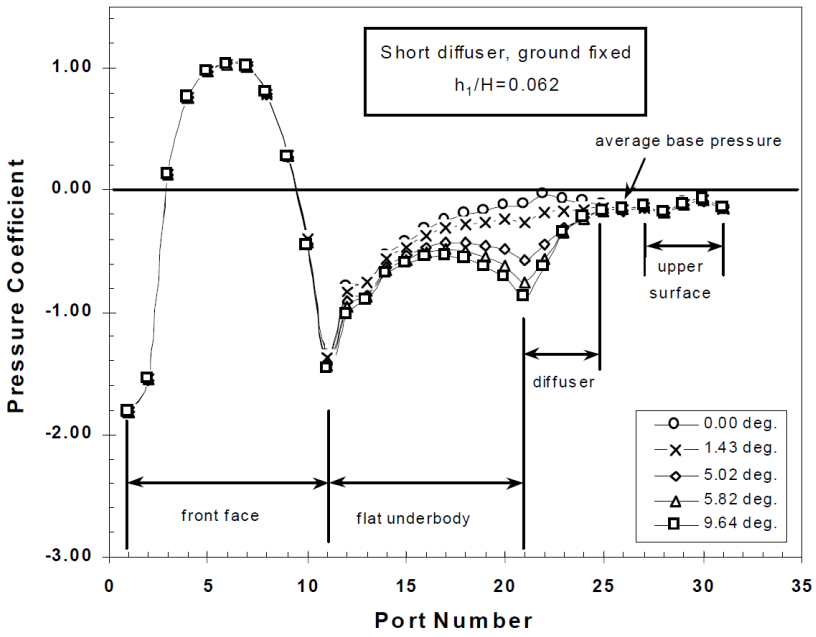

Figure 2.5: The effect of increasing diffuser angle on C_P around a bluff body [4]

2.4 Maximum downforce diffuser angle

As shown above from figure 2.5, there is an increase in diffuser performance with increasing diffuser angle. Several studies have been performed to try and find the optimal diffuser angle in order to maximize downforce. Maximum downforce diffuser angles as high as 20° have been found by Ruhrmann and Zhang [13], Jowsey and Passmore [14, 15] report angles closer to 13° to be optimal. Some mechanisms that affect diffuser performance at higher angles identified by Ruhrmann and Zhang [13] are the formation of separation bubbles near the diffuser inlet, for angles as low as 10°, and the further growth of these bubbles at higher angles, affecting the breakdown of streamwise vortices formed at the diffuser sidewall. These will be discussed in a bit more detail in section 2.6. The differences between the reported maximum downforce diffuser angle have been attributed in some degree to the difference in boundary conditions between the studies [16]. As mentioned by Ehirim [16], the studies done by for example Ruhrmann and Cooper [4, 13] used a rolling road system, where Jowsey and Passmore [14, 15] conducted measurement over a stationary ground plane. The effect of this is described in section 2.5.

2.5 Effect of rolling road and ride height

As mentioned earlier, the ground proximity of the model is an important parameter in the diffuser performance. Secondly, in an automotive application, the effect of a stationary vs rolling floor in testing is another factor to consider, especially when performing windtunnel tests. In order to properly mimic the real world conditions of a vehicle driving on a road, it is important to reduce the effect of a floor boundary layer growing on a stationary windtunnel floor. This boundary layer artificially reduces the massflow underneath the model, compared to a real world driving scenario where this ground boundary layer wouldn't be present. This is usually solved by introducing a rolling floor/belt in the windtunnel on which the model is positioned. The effect of this is shown

in figure 2.6 [4], where it is clear that the C_P is slightly more negative under the model for a moving belt system, than it is over a stationary floor in the windtunnel.

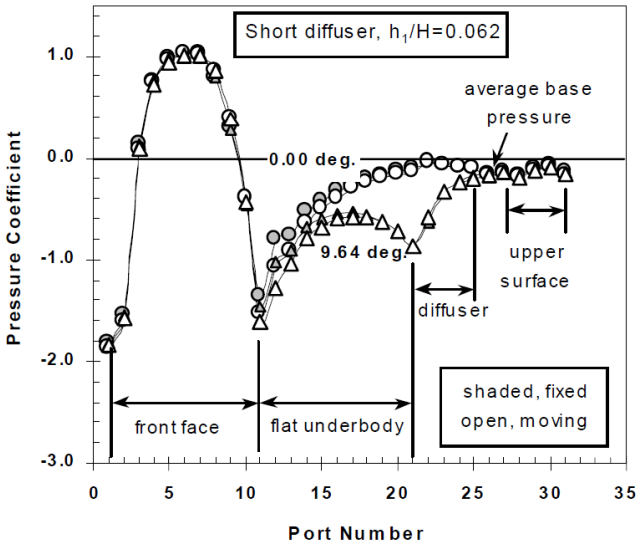

Figure 2.6: Effect of rolling vs stationary road on C_P distribution [4]

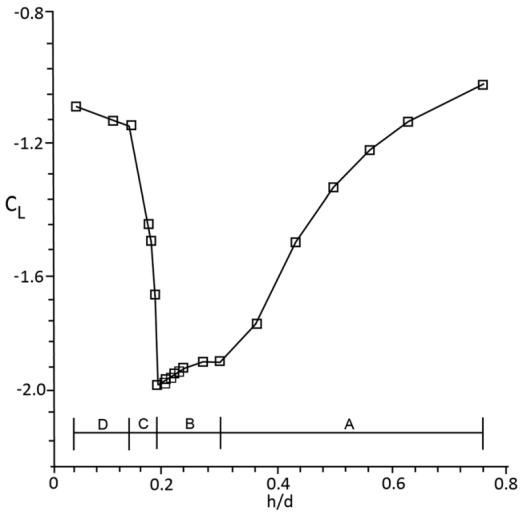

Figure 2.7: Effect of ground proximity on diffuser downforce [5]

Returning to the previously mentioned ground effect and its relation to ground clearance/ride height, Senior et al. [5] investigated the downforce produced by a bluff body with a 17° diffuser fitted at various ride heights. The results in terms of C_L are plotted in figure 2.7 against the non-dimensionalised rideheight h/d, where h is the models height of the ground/floor, and d is the diffuser half width. It shows 4 key regions identified by lowering the right height of the model. In region A, there is a clear increase in downforce generated with lowering ride height, region B is the so called maximum downforce region, region C where the diffuser stalls and rapidly loses performance with decreasing ride height, and finally region D, where the diffuser is performing very poorly and generating low downforce. Loss of downforce is usually attributed to the formation of separation bubbles, originating from the diffuser inlet, and the strength reduction and/or breakdown of streamwise vortices originating from the diffuser sidewalls [17–19]. Figure 2.7 shows the importance of ride height, and the diffusers sensitivity to this parameter.

2.6 Streamwise vortices

Up until now, only the quasi 1D flow through a diffuser has been discussed, but as we are interested in automotive diffusers, there will be some important 3 dimensional flow aspects to consider. One of the most important ones discussed in literature is the formation, strength and breakdown of streamwise vortices, coming from the sidewalls of a plane diffuser. These counter rotating vortices originate from the inflow induced by the pressure difference between the inside of the diffuser and the flow around the sides of the body in question. A low static pressure core of the vortex might improve the performance of the diffuser, as well as help keeping flow attached, due to the added upwash on the inboard side of these vortices. George [6] showed that the vortices formed by having endplates on the side of the diffuser delayed the formation of a separation bubble inside the diffuser, which improved its performance. Even at extreme diffuser angles as high as 30°, George showed that the vortex pair was strong enough to help reattach flow from a separation bubble formed upstream on the flat floor of the model.

A study by Jowsey in 2010 shows that splitting the diffuser into multiple channels by adding additional vertical fences inside the diffuser lead to an increase in the diffuser pumping effect [14] and [15]. The study also showed that adding more streamwise vortices by splitting the planar diffuser into more channels, diffuser performance was improved at higher diffuser angles, attributed to the suppression of flow separation inside the diffuser and by constraining the vortex structures formed from the additional fences.

Ruhrmann and Zhang [13] have used oil flow visualization in order to show the presence of these streamwise vortices, as well as their breakdown at higher diffuser angles together with the appearance of separation bubbles. These are shown in figure 2.8 on the next page.

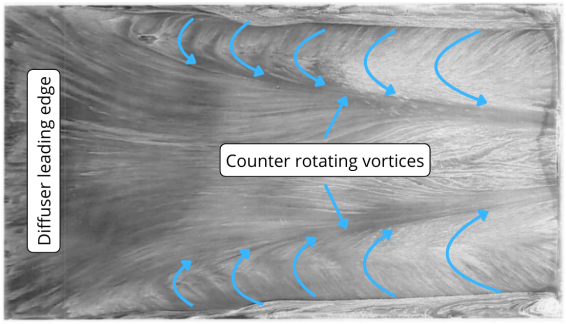

(a) $\theta = 5°$

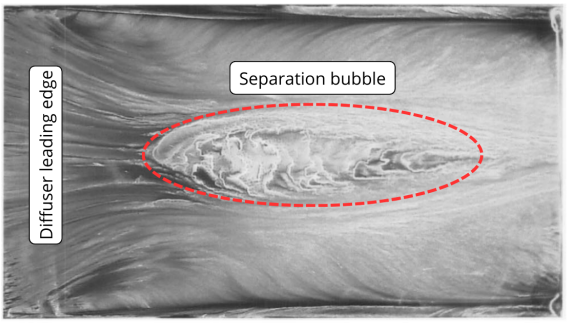

(b) $\theta = 10°$

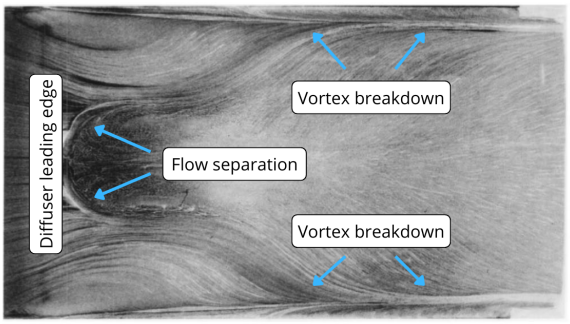

(c) $\theta = 15°$

Figure 2.8: Surface oil flow visualization on diffuser ramp [13]

The oil flow pattern on the 5° diffuser, figure 2.8a, clearly shows the presence of the counter rotating vortex pair, with a fully attached flow along the diffuser centerline. Figures 2.8b and 2.8c both show signs of a recirculation zone on the surface of the diffuser, attributed to a separation bubble. The counter rotating vortex pair from figure 2.8a is still clearly present along the entire diffuser length for the 10° diffuser geometry. However, at the 15° diffuser these vortices appear to break down not far downstream of the separation region in the diffuser center.

3. Flow Measurement Techniques for Diffuser Aerodynamics

This chapter will cover some of the current techniques used to study the performance of diffuser equipped bluff bodies such as force balance measurement, oil flow visualization, Computational Fluid Dynamics (CFD) and Particle Image Velocimetry (PIV). Finally a recent experiment on using an on-site particle tracking system for automotive underbody aerodynamics is discussed.

3.1 Experimental techniques

Many of the studies and experiments discussed in Chapter 2 rely on the use of windtunnel experiments to quantify diffuser performance and/or visualize flow structures. Force balance measurements provide a clear way off assessing diffuser performance in terms of downforce produced, as used by George [6], Cooper [4] and Ruhrmann and Zhang [13]. However, these balance measurements are only indicative of the force and moments on the total system, and cannot give any insights on how these force are generated. Surface pressure taps are useful tools used to gauge the pressure distribution around a model, however they require a relative large number of taps in order to give an accurate approximation of the surface pressure distribution. Figures 2.5 and 2.6 are both constructed using data generated by pressure taps, and give a good indication on what is happening at the underside surface of the diffuser model, but are not able to give much information on what is happening off surface. Oil flow visualizations like the ones used by Ruhrmann and Zhang in figure 2.8 are again limited to visualizing surface flow behavior, and as with the pressure taps, lack the 3 dimensional flow data.

As mentioned in section 2.5 earlier, the proper simulation of a car driving over a road requires boundary layer suction devices and/or rolling floors in a windtunnel setup. This has been a proven and effective technique [4], but comes at a cost of complicating the windtunnel experimental setup, both in a physical and in an economical way. An example of such a windtunnel rolling floor and model is given in figure 3.1.

Figure 3.1: Formula One windtunnel model on rolling floor [20]

Within a motorsport application, diffuser aerodynamics are usually used in an engineering development setting, i.e. trying to optimize a design, for example to produce maximum downforce. In this way, CFD, windtunnel as well as full scale vehicle testing are used to develop a car [2]. CFD provides engineers with a tool that is very well suited for visualizing all the flow structures and mechanisms around a car, as it is capable of modelling the full flowfield. This is very important in helping understand aerodynamic mechanisms and provide new design directions [2]. CFD does however have its limitations, as it is a trade-off between modeling accuracy and computational costs. There are countless variations on making these trade-offs, all being very case dependent. One can imagine that accurately modeling the complex 3D flows around a Formula One car becomes computationally expensive, very fast. Hence, currently Formula One teams still use windtunnel models, like the one in figure 3.1, as a main source to validate CFD results, and try to correlate data to full-scale vehicle testing done in race-events.

Marklund and Lofdahl [12, 21] investigated the difference in C_P across a diffuser-equipped bluff body, obtained by running a CFD simulation with a $K-\epsilon$ turbulence model, to the pressure tap readings from a windtunnel experiment. They were able to show a good correlation between the two datasets, however, disparities remained, and high mesh refinements were needed to accurately model for example the pressure peaks at the diffuser inlet and flat floor leading edge. As discussed by Ehirim [16], most of the challenges with CFD stem from the need for high mesh refinement, proper prediction of separation regions and turbulent energy dissipation. This means there will always be the need for experimental techniques to work with CFD to validate simulation results, especially in an engineering setting where computational and/or time resources might be scarce.

3.2 Particle Image Velocimetry

Particle Image Velocimetry (PIV) is a flow measurement technique that can provide off-surface flow field data in an experimental windtunnel testing setup. The output is a velocity vector field which can be mapped onto a regular Cartesian grid. This makes the technique an useful tool for validating CFD simulations, as well as give a direct way of quantifying the flow structures that happen in the flow around a test subject.

PIV is an experimental measurement technique, which utilizes tracer particles seeded in the flow around a test object, illuminated by a strong light source, being captured by cameras looking at a 2D plane [22]. The successive images captured are used to quantify the displacement of the tracer particles in the flow. The measurement domain is divided up into interrogation windows, on which a cross-correlation algorithm is used to solve for the average displacement of the particles inside this window, between successive images. The resulting shifts can be combined with the image acquisition frequency to compute a velocity vector for each individual interrogation window. Importantly, there are no individual particles being tracked in PIV, only a cross-correlation technique applied to the interrogation windows [23]. Hence, the interrogation window size is what drives the spatial resolution of the method.

Some PIV has been done on diffuser aerodynamics, most notably by Senior in 2002 [5]. By using transparent diffuser sidewalls, a laser sheet could be projected from the side of the model into the diffuser area, otherwise optically obscured by the diffuser sidewalls. This way, using planar PIV, Senior was able to capture the formation and behavior of the streamwise vortices originating from the diffuser sidewalls, as shown in figures 3.2 and 3.3 below.

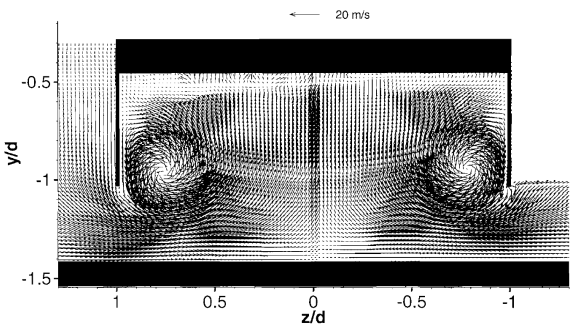

Figure 3.2: Cross flow velocity vectors in a planar diffuser from PIV [5]

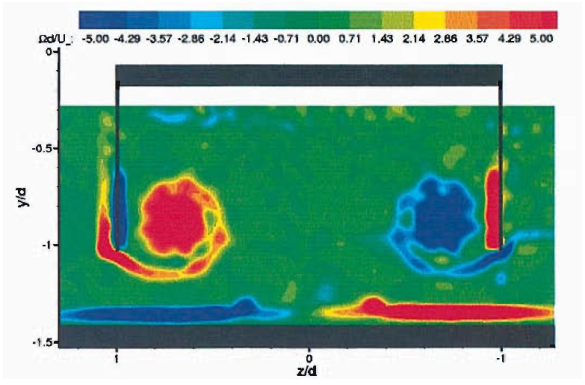

Figure 3.3: Mean vorticity in a planar diffuser from PIV [5]

The fact that the model required transparent sidewalls highlights the difficulty one might experience when looking to apply PIV on automotive floor and diffuser aerodynamics. Gaining optical access to these regions (a key criteria to perform PIV) becomes challenging with more complex geometries, especially if one wants to have a rolling floor in tunnel, as those are not yet available in a transparent form, and they are critical in replicating real world testing conditions of a car driving. With geometries as complex as the one shown in figure 3.1, using "tricks" like a transparent sidewall will not be enough to gain access to the flowfield under the model.

PIV has also been applied in a 3D setting, most notably using a so called Tomographic PIV (Tomo-PIV) setup, first proposed by Elsinga et al. in 2006 [24]. Tomo-PIV usually uses a setup of four to six cameras looking at a measurement volume [25], capturing the light scattered by tracer particles within the measurement domain. The cameras view the volume from different angles, allowing for a 3D reconstruction of the light intensity of the particles, discretized in voxel elements. These voxel elements are similar to the 2D interrogation windows mentioned above, and they define the 3D grid on which a velocity field is constructed. Using techniques similar to the cross-correlation techniques of planar 2D PIV, the 3D particle displacement in each voxel, and hence the local flow velocity, is obtained [25]. Figure 3.4 from Westerweel et al. [25] below gives an example tomographic PIV setup that can be used to measure a flat plate boundary.

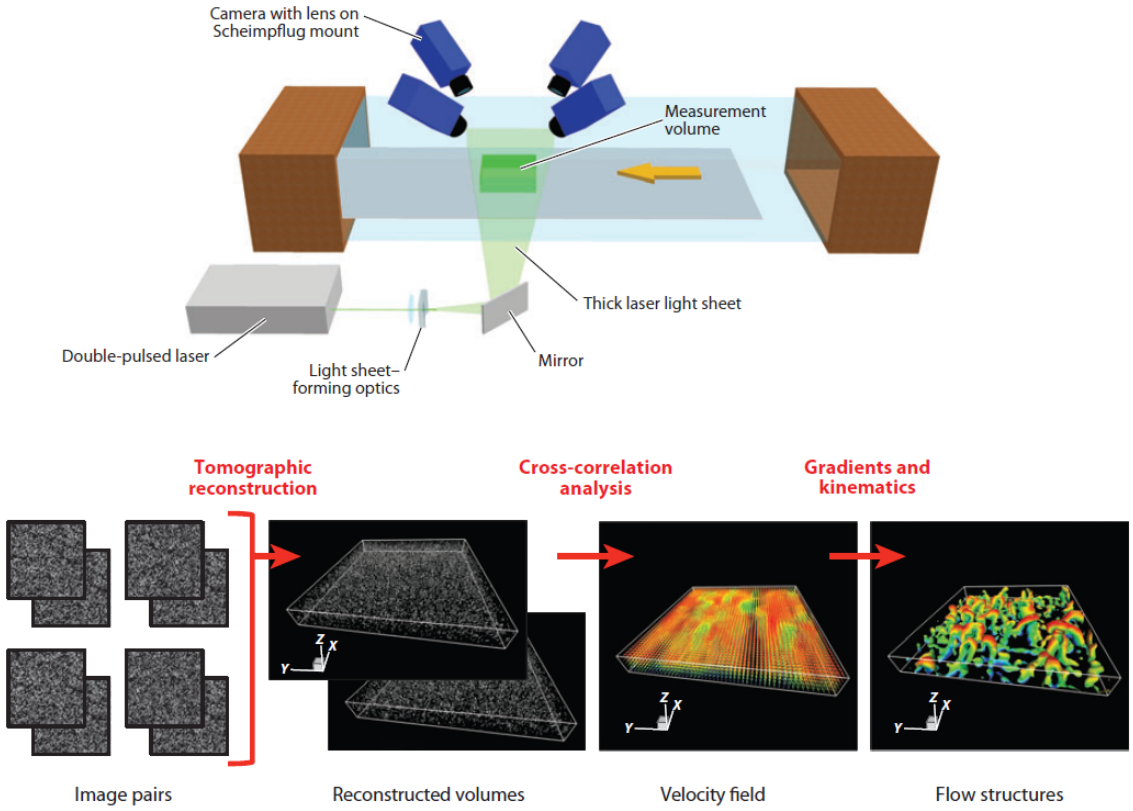

Figure 3.4: Example of a Tomo-PIV setup to measure a flat plate boundary layer, from Westerweel et al. [25]

Tomographic PIV can deal with particle densities in the order of 0.05 particles per pixel (ppp) through the measurement domain [25]. It does however not scale very well with increasing measurement volumes. The algorithms used for the reconstruction of the 3D position of the particle image intensities from the 2D camera images are computationally expensive [7]. Expanding the measurement domain increases the computational time, and requires keeping a larger and larger amount of data in memory [7]. Other limitations are described by Schanz et al. [7], such as but not limited to, positional errors stemming from the discretization of the particle locations on the voxel grid, a limit on the dynamic velocity range (i.e. the range of maximum and minimum velocities that can be resolved in a flow field) and a smoothing on velocity gradients due to the cross-correlation techniques applied.

3.3 Lagrangian Particle Tracking

Lagrangian Particle Tracking (LPT) is a form of Particle Tracking Velocimetry (PTV). As its name suggests, this technique reconstructs and tracks the position of individual particles, compared to the cross-correlation techniques applied in interrogation windows or voxels for 2D and 3D PIV respectively.

3D PTV techniques have been used already before the introduction of Tomo-PIV, but the used methods were only able to reconstruct particle tracks in flows with very low seeding densities, in the order of 0.005 - 0.02 particles per pixel (ppp) [22]. The introduction of the so-called Shake-The-Box (STB) algorithm by Schanz et al. in 2016 [7] allowed for the advancements in 3D LPT where particle tracks can be reconstructed using much higher particle image densities. PPP values in the order 0.05 - 0.2 could now be processed, which brings it more or less equal to the performance of Tomo-PIV in terms of particle image density [22].

3D LPT relies on the following basic steps to generate particle tracks within a certain measurement domain: Images from illuminated particles inside the flow are taken from different camera standpoints, looking at a certain measurement domain. For each individual camera, the light intensity peaks from the particle images are projected from the 2D camera images back to the 3D measurement domain. An intersection of the projected peaks (essentially a straight line) coming from multiple cameras allows for the triangulation of the original particle in 3D space. Doing this for all light intensity peaks from all cameras allows for the reconstruction of the 'original' particle cloud in the 3D measurement domain.

Doing this for multiple successive images/timesteps, particle tracks can be generated using specialized tracking algorithms. These algorithms attempt to follow individual particles across multiple timesteps, allowing for the construction of time-resolved 3D particle tracks in the measurement domain.

An overview of the basic steps of LPT is shown in figure 3.5, taken from the work of Schröder and Schanz 2023 [22].

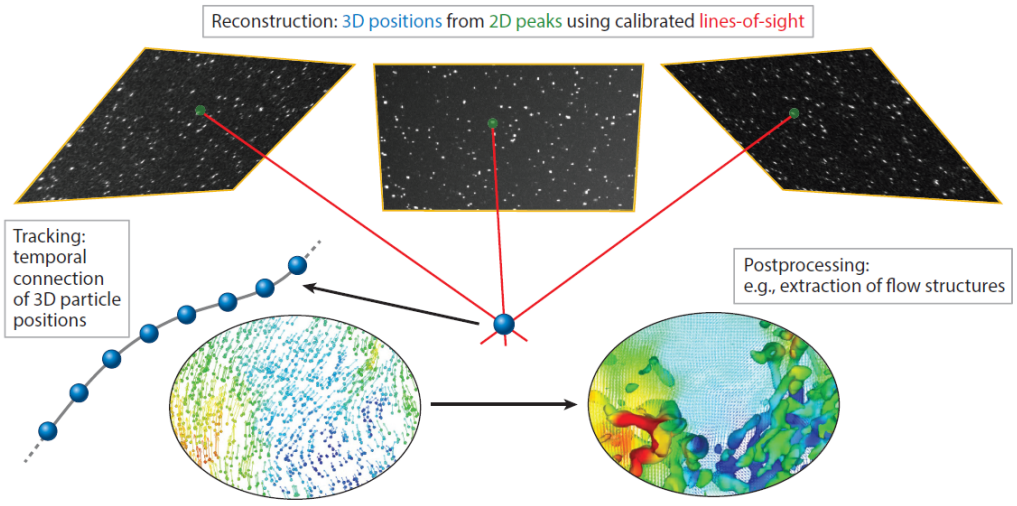

Figure 3.5: The basic steps of a Lagrangian particle tracking experiment, taken from Schröder and Schanz 2023 [22].

The resulting particle tracks can be used to analyze the individual movement of particles through the flow. Data from multiple particles can also be combined to build full 3D flowfield data on regular Cartesian grids, by interpolating the velocity and/or acceleration data from particle tracks to grid points. This results in datasets similar to the ones from Tomo-PIV, and can be compared to data from for example CFD simulations.

Schanz et al. shows that the performance of the STB algorithm used for 3D LPT compared to standard Tomo-PIV methods is superior in terms of local accuracy, solution completeness, surpression of ghost particles, spatial resolution and computational effort [7]. The expansion of the measurement domain (for both Tomo-PIV and 3D LPT) was in part limited by the amount of light scattered by the oil droplet tracer particles used, which had diameters in the order of 1 μm. Expanding the lasers used to create illumination sheets in planar PIV to larger volumes also reduces the illumination intensity that can be used for the particle imaging [26]. Together with the development of neutrally buoyant Helium-Filled Soap Bubbles (HFSB) by Scarrano et al. [26], which have diameters in the order of 300 μm, and the development of large high powered LED unit, 3D LPT can be applied to large measurement volumes, in the order of several 100's of liters [22].

3.4 On-site 3D Particle Tracking using the Ring of Fire

In 2019, Spoelstra et al. proposed a new technique to measure the aerodynamic drag of a cyclist, the so called Ring of Fire (RoF) [8]. The RoF setup allows for the characterization of flows around moving objects such as athletes or ground vehicles. Using a stereographic PIV setup, Spoelstra was able to conduct measurements on cyclist cycling through a 2x2 m^2 plane, illuminated by a laser. The laser sheet illuminated sub-millimeter HFSB, generated by a seeding rake set inside a large tunnel structure. By examining the wake produced by the cyclist, and applying a control volume analysis based on the work of Terra et al. [27], the aerodynamic drag of the cyclist in different positions was measured.

Figure 3.6 below gives an overview of the setup used by Spoelstra et al. [8] for the on-site measurement of the cyclist drag.

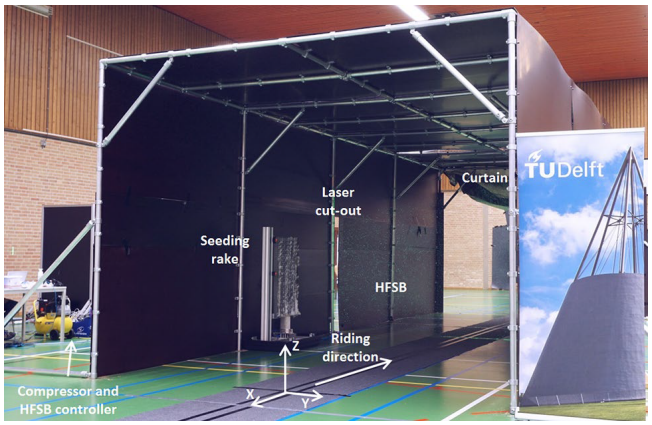

Figure 3.6: Ring of Fire setup used by Spoelstra et al. (2017) [8] to measure cyclist drag on-site

The fact that the RoF setup is capable to be applied on-site, i.e. at a local testing track, velodrome, indoor-sport facility etc. makes it very useful in testing a broad range of test subjects. It eliminates the need for (potentially scaled) windtunnel models, and can measure the test subject of interest directly.

In a similar setup, the aerodynamic drag of speed skaters has been investigated using the Ring of Fire by Spoelstra et al. (2023) [28]. This study employed a very similar setup compared to the study on cyclist in 2017, but used a much larger tunnel structure to contain HFSB around a measurement plane of $10m^2$. Ice-skaters wearing laser protection safety goggles skated through the measurement plane in different skate positions. The stereoscopic PIV system measured the flowfield at the measurement plane, which then served as inputs to the momentum based control volume analysis [27], allowing for the quantification of the drag of the cyclist, in each of the different positions.

An example of some of the measured velocity fields based on the acquired images with the RoF setup is shown in figure 3.7.

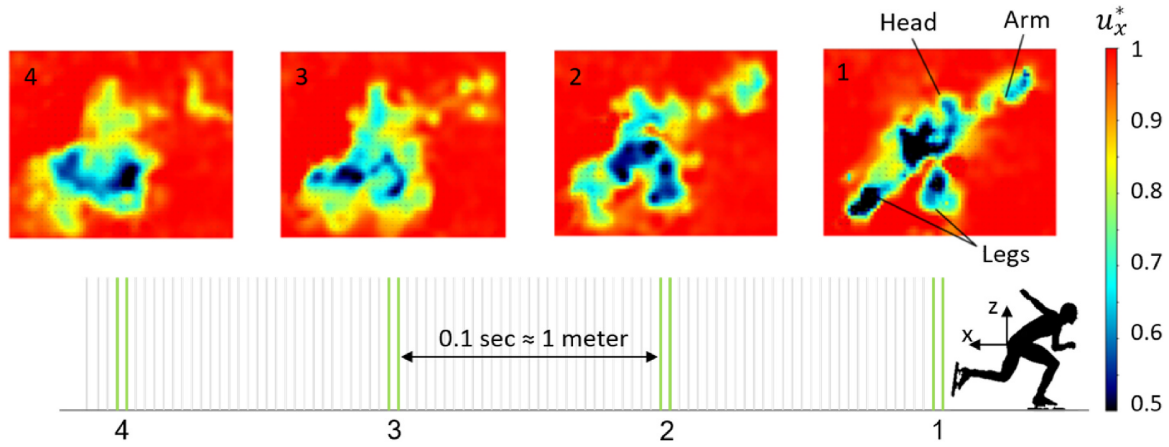

Figure 3.7: Example of velocity fields measured with the Ring of Fire for the passage of a speed skater, from Spoelstra et al. (2023) [28]

Getting back to automotive aerodynamics, the RoF setup has been used to measure the flowfield around a Volkswagen Up! vehicle. Hüttig et al. (2023) applied a 2 camera Shake-The-Box quantification of the flowfield measured in a roughly 46 m^2 domain [29]. The resulting particle tracks from different runs were combined, and binned into Gaussian weighted bins of 32x32x32 mm^3, resulting in a 3D velocity field of the wake of the vehicle. The resulting wake velocity field is shown in figure 3.8.

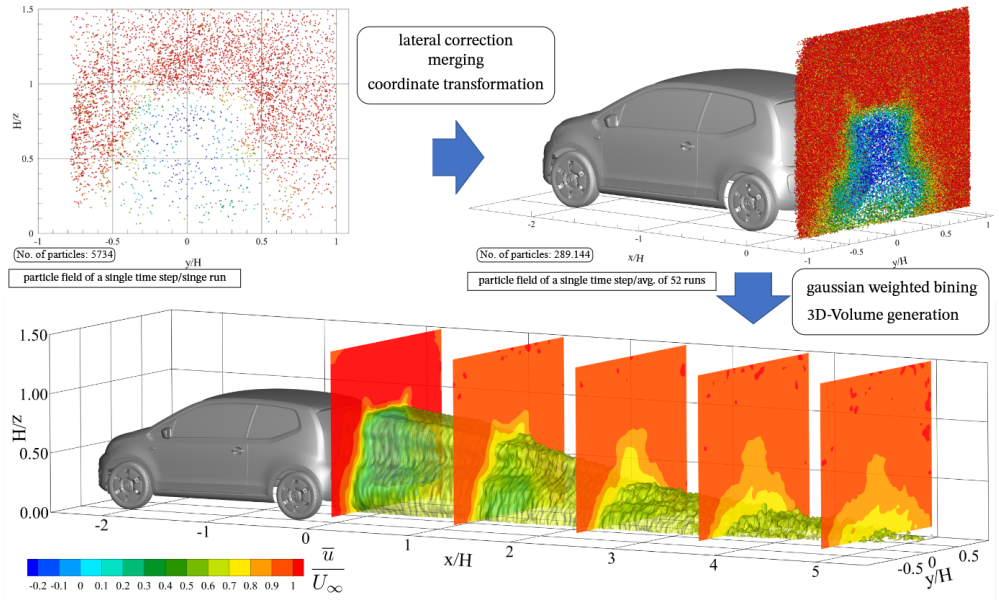

Figure 3.8: Illustration of processing of the particle fields: single particle field one time step (top left); merged particle field of in total 52 runs (top right); resulting bin averaged 3D velocity field the wake of the vehicle (bottom) from Hüttig et al. (2023) [29]

This result shows the potential of using the RoF setup to perform LPT measurements, and the large measurement domain that is achievable using the HFSB. The wake of a car was fully captured, while using a 'standard' road vehicle, without the need for a windtunnel, design a model, install a rolling floor, etc. The combination of the Ring of Fire and the Shake-The-Box lead to the experiment performed by Battegazzore et al. [9], where 3D LPT was performed on a Radio-controlled (RC) car model, retro-fitted with a flat floor and diffuser. The experiment was centered around a RoF setup using subterranean cameras and LED illumination units looking up through sheet of transparent Lexan. By driving a car across this sheet, optical access to the underside of the body was achieved, which allowed for the application of 3D LPT under the car model. Neutrally buoyant Helium-Filled Soap Bubbles [26] were used as seeder particles.

Using the above mentioned setup, Battegazzore was able to test a range of diffuser angles, going from 5° to 20°, and resolve the mean flowfield under the car and inside the diffuser. He was able to capture difference in underbody flowfield between the different diffuser angles, mainly in terms of peak velocity under the car. Some centerline velocity distribution are shown in figure 3.9. Signs of flow separation in the diffuser area were observed, mainly at diffuser angles 15° and 20°, which are somewhat in line with some of the observations of Ruhrmann and Zhang [13], who noted separation bubbles forming from diffuser angles above 10°.

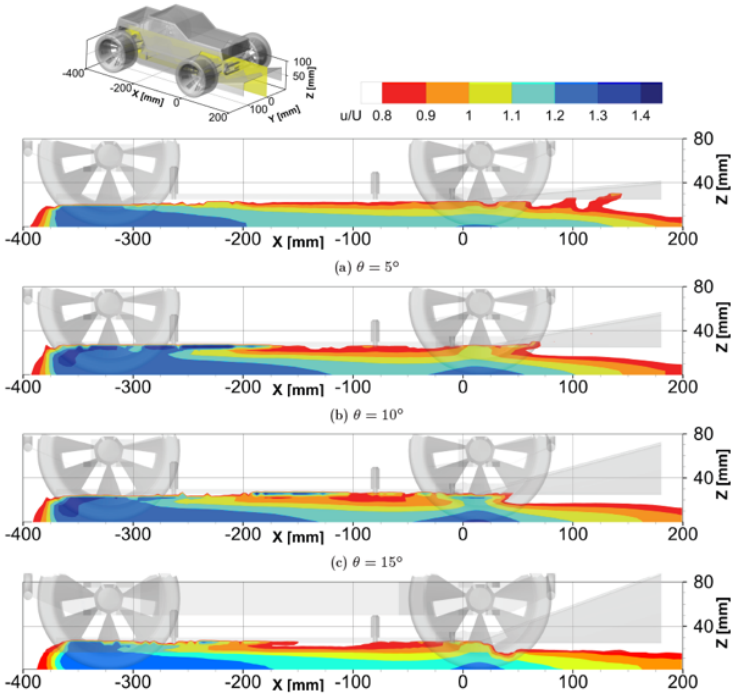

Figure 3.9: Velocity contours on car centerline at different diffuser angles [9]

The facility did have its limitations however. Particle tracking using the Shake-The-Box algorithm was challenging, as only 2 cameras were used to capture images. This lead to many ghost particle tracks being introduced, reducing the effectiveness of the STB algorithm [7]. Secondly, seeding distribution around the model was sub-optimal, in part due to the small seeding container used. This meant that the car traveled through the seeded volume of air for a short period, not allowing much time for the entrainment of the HFSB, especially in recirculation regions. This is particularly relevant in regions of separation, where reverse flow is present, and seeding particles would need a relatively long time to properly populate these regions. Reflections in the images originating from both the Lexan sheet and car proved difficult when trying to do particle tracking, requiring high image pre-processing before particle tracking could be performed, limiting the resulting usable measurement volume.

Next to that, the car model itself was not ideal for studying the diffuser flows commonly seen in the literature. Due to the very wide rear tires and relatively exposed upper body work, flow appeared to exit through the sides of the diffuser, laterally, towards the wake of the rear tires. This is the opposite flow direction than that of a "common" planar diffuser with straight sidewalls, where there is lateral inflow into the diffuser, creating the characteristic longitudinal vortex pair (visualized in figures 3.2 and 2.8). This outflow is shown in the following figure 3.10, where it is clearly visible that besides some outflow after the front tires, also in the diffuser region flow is going towards the outside of the car instead of into the diffuser.

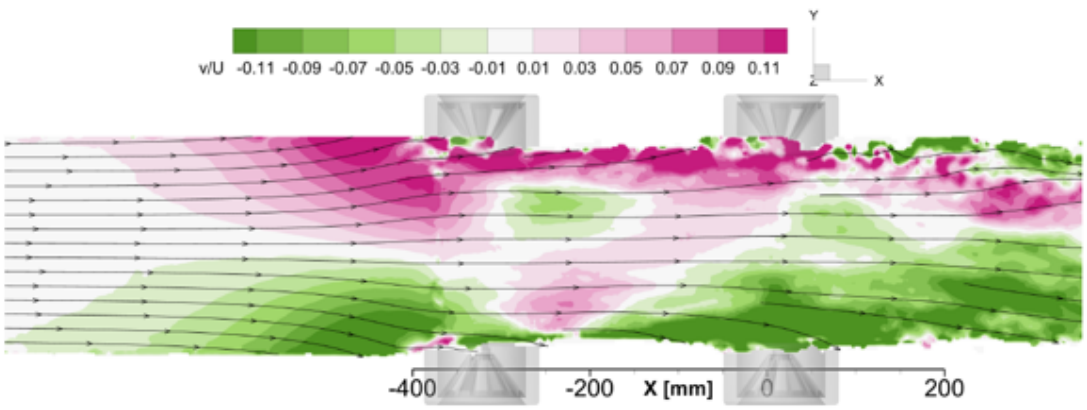

Figure 3.10: Spanwise velocity component under diffuser equipped RC car [9]

4. Research proposal and questions

4.1 Research Gap and Objectives

Aerodynamics optimization has shown to be an important method of enhancing the performance of race cars, be it through minimizing drag, or producing downforce. Underbody aerodynamics, which consists of the floor and diffuser area on a car, are a large part in the generation of this downforce. Underbody flows have been challenging to characterize in an experimental setup, especially using PIV or PTV, due to the lack of the optical access required for image acquisition and illumination.

From the literature described in chapters 2 and 3, a master thesis project is setup as a continuation of the on-site Ring of Fire particle tracking setup used by Battegazzore [9]. The aim is to build and improve upon the experimental setup used for that work, with the following 3 main objectives:

- Improve LPT capabilities by increasing the number of cameras used, reduce reflections, Lexan sheet vibrations, etc.
- Create better seeding distribution around the model, mainly focusing on seeding density and larger seeding containment for the car to travel through.
- Improve diffuser performance of the model by redesigning bodywork, floor and diffuser integration on the RC car.

4.2 Research Questions

From the research gap and objectives, the following research questions have been formulated. They are split into questions related to automotive aerodynamics, and ones focussed on the RoF LPT setup.

How do geometric modifications influence flow separation and downforce generation in automotive diffusers?

1. How does a rounded diffuser leading edge change the performance of a 15° diffuser compared to a sharp leading edge, in terms of peak velocity, pressure distribution and downforce generated?
2. How effectively can vortex generators delay or reduce separation inside a diffuser?
3. What is the effect of streamwise vortices within the diffuser in terms of peak velocity, pressure distribution an downforce generated?

How accurately can the Ring of Fire system measure critical aerodynamic characteristics of race car diffusers?

1. What spatial resolution/bin size can be achieved with the new setup?
2. How many runs are needed to reach a mean flow velocity convergence within 1% of to the car's velocity?
3. How accurate is the RoF setup in quantifying velocity and pressure distributions, as well as downforce figures for automotive applications?

5. Methodology

This chapter will cover the methodology and experimental setup related to this thesis project. An overview of the on-site Ring of Fire is given, discussing the changes made to the setup compared to the work of Battegazzore. The RC car used and different bodywork configurations are discussed.

5.1 Ring of Fire Setup

The following section discusses the changes made to the Ring of Fire setup (starting from the work done by Battegazzore [9]), based on the objectives laid out in 4.1. The setup as displayed in figure 5.1 was the starting point for the new experimental setup.

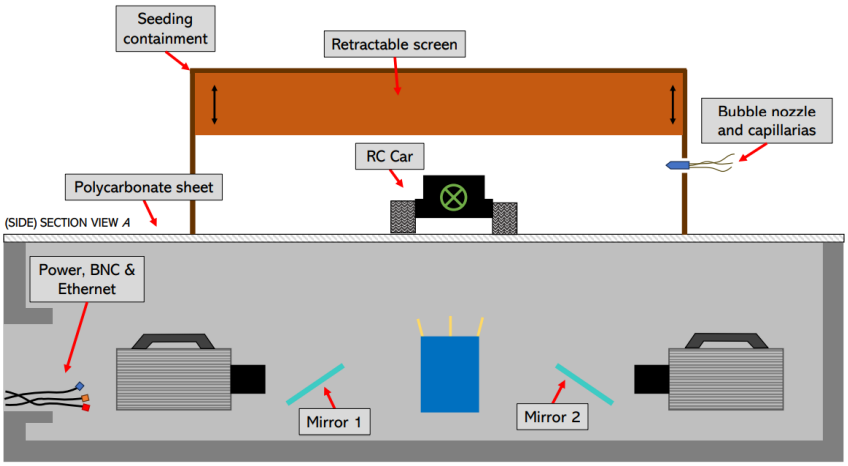

Figure 5.1: Ring of Fire setup used by Battegazzore [9]

5.1.1 Camera and illumination positioning

In order to improve the particle tracking capabilities of the setup, a new camera and illumination layout was designed. The same subterranean concrete shell was available, which has internal dimensions of 200x63x50 cm^3. Contrary to the work of Battegazzore, Photron FastCAM Mini AX 100 cameras were available, which are considerably smaller than the original Photron FastCAM SA1 used. This allowed for the positioning of 3 cameras inside the shell, compared to the original 2. As discussed before, more cameras allow for better particle tracking with the Shake the Box algorithm, as it reduces the number of ghost particles in the measurement domain. To make the 3 camera setup possible, as well as slightly decreasing setup complexity, the mirrors were removed from the ditch. In the new setup, the cameras were pointing almost straight up, and positioned in the middle of the shell. This was in part possible by the use of AF Nikon 20mm focal length lenses. The lenses and positioning of the cameras resulted in a measurement domain of around 300 mm by 150 mm by 200 mm. Within this domain, the field of view of the three cameras overlaps, allowing for the tracking of particles using the 3 points of view. A lens aperture $f_{\#} = 16$ used allowed for a depth of focus such that all particles are in focus throughout the 200mm measurement volume height, while still allowing for enough light scattered by the particles to be captured to create a usable image. The capturing and post-processing of the images will be discussed more in chapter 6.

As the cameras were now located in the middle of the shell, the setup of the LED used by Battegazzore wasn't possible anymore (see figure 5.1). As illumination of the tracer particles is critical in the use of LPT,

another solution was devised. Instead of a single illumination source centered in the shell, 2 LaVision 300 LEDs are positioned to the side of the cameras. They are pointed at a roughly 45 degree angle upwards, illuminating the measurement domain from both the left and right hand side (from the car model perspective). A benefit of this configuration is that the light sources give less reflection on the Lexan sheet covering the setup in the shell. These reflections were present quite prominently in the images captured by the setup of Battegazzore, and required high image processing to reduce the impact on the particle tracking capabilities. With the light sources positioned outboard to the side of the cameras, direct reflections on the Lexan in the cameras field of view were reduced considerably. Finally, the increase in light intensity by doubling the amount of light sources helped in reaching the final measurement domain in which particle tracks could be generated. With these changes, a schematic overview of the setup inside the concrete shell is given in figure 5.2 below. An overview of the experimental parameters and instrumentation is presented at the end of this chapter.

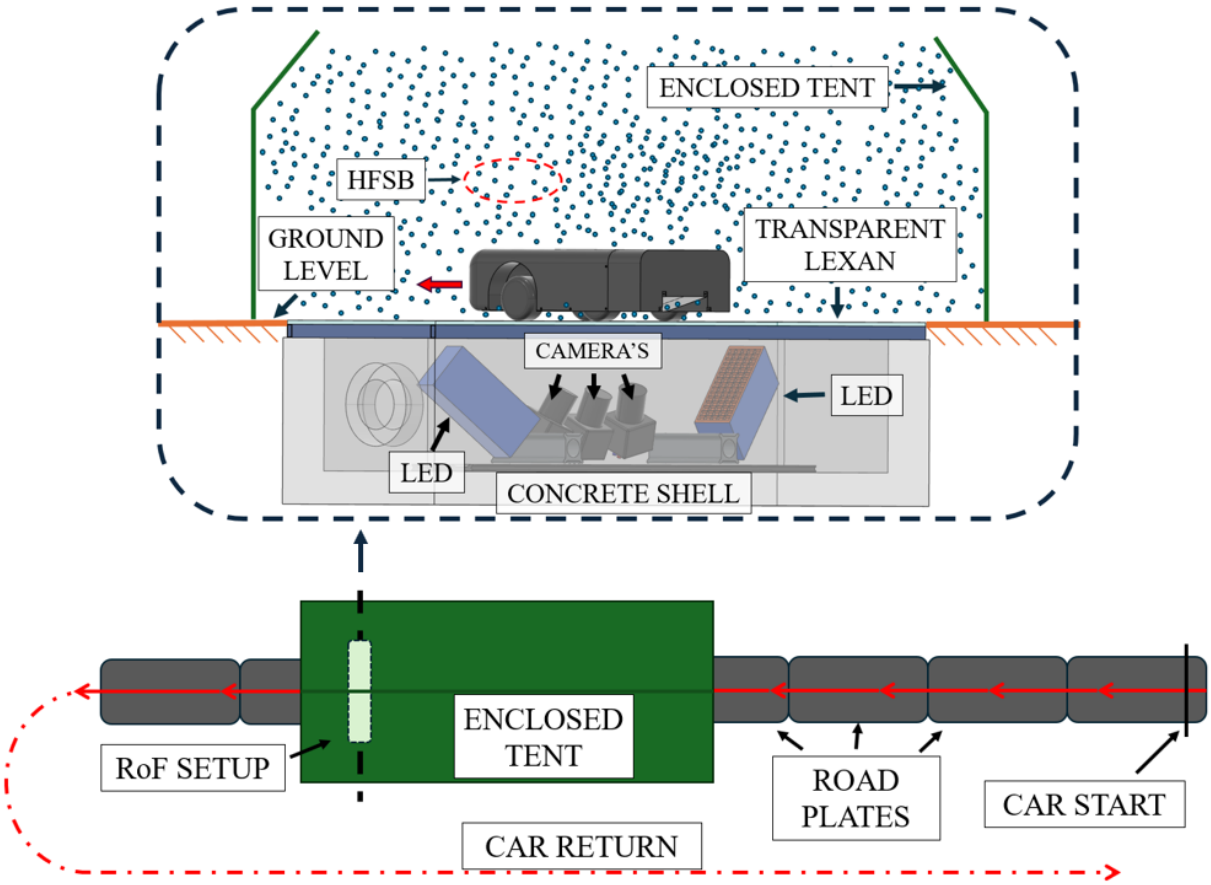

Figure 5.2: Experimental setup in top view, as well as a detail of the Ring of Fire setup inside the tent

5.1.2 Seeding containment and track layout

The second objective from 4.1 was set as a requirement to improve the seeding distribution around the car model. Due to the relatively short and small seeding container used by Battegazzore, seeding density in the diffuser area was quite low on average. Especially for recirculating flows such as separation regions in the diffuser, it is important that particle have enough time to be entrained by the car model. As the car is traveling, this means a longer seeding container was needed to make sure the HFSB had as much time as possible to be distributed around the model. With a larger seeding container comes the challenge of generating more bubbles in order to fill this larger volume with a sufficient particle density.

In order to tackle both these problems, the following was altered to the setup. Instead of using a separate box like container setup over the measurement domain, a fully closed off tent measuring about 4 meters tall, 3 meters wide and 9 meters long is positioned above the concrete shell and road ahead. This provided a much longer domain that could be filled with HFSB, compared to the 70 cm long C shaped section used by Battegazzore. It did however significantly increase the demand for bubble generation. In order to reach a proper seeding density in the full tent, the single bubble generating nozzle used previously was far from sufficient. As an alternative,

a 200 nozzle seeding rig developed in house at the Delft University of Technology was available. This seeding rig is capable of producing enough bubbles to completely saturate the tent with HFSB in about 60 seconds. Running only half of the available nozzles proved to be sufficient to ensure a constant, high enough seeding density. The images captured by the cameras in the ditch showed an average particle image density of around 0.045 particles per pixel (ppp). Once the proper seeding density was reached in the tent, the seeding rig was left on to run continuously, which creates a relatively consistent level of seeding between runs. The tent was closed off on all sides, leaving only a small front and rear opening for the car model to pass through. The front opening was closed off between runs to prevent too much wind draft carrying away particles out of the tent.

With the tent being completely filled with HFSB, it was critical to ensure that the concrete shell was properly sealed, as any bubbles entering the shell could damage the sensitive electronics of both the cameras and the LEDs. A transparent 12mm thick Lexan sheet was used to cover the top of the shell. This is the same way as was done by Battegazzore, however in that work it became evident that the forces of the car model driving across the sheet made it vibrate ever so slightly. These vibrations then caused issues in combination with the reflections of the LED light on the sheet, leading to the need to discard large parts of images in the pre-processing step of data processing. Discarding parts of the image then reduces the available measurement domain, reducing the capabilities of the Ring of Fire system. Apart from repositioning the LED units to the side of the cameras, the Lexan sheet was also stiffened with a steel box frame around the perimeter. The additional stiffness from the frame reduced reflection vibrations, allowing for a cleaner image captured by the cameras.

Finally, as was also done by Battegazzore, the road surface ahead and behind the shell was covered with flexible road cover sheets. These reduce bumps and gaps in the road, making it a bit more level for the car to drive on. It is critical that the car stays as level as possible during its travel across the camera setup, as this increases consistency in the aerodynamics between runs. The results of these changes lead to the setup depicted in figure 5.3 below.

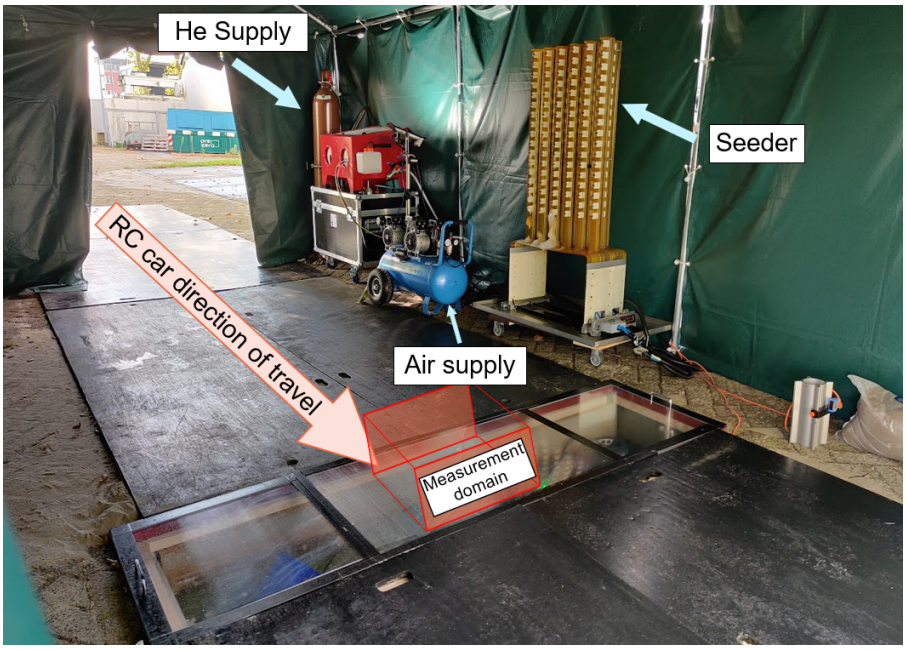

Figure 5.3: Experimental setup above ground

5.2 Test model design

With the setup design mostly focusing on the first and second research objectives, the car model bodywork was adapted with the aim of addressing some of the aerodynamic issues of his model, found by Battegazzore. This objective was added as the lateral outflow found in the diffuser from that model is the opposite of what is typically observed in automotive diffusers. The inflow normally seen creates the streamwise vortices which aid in diffuser performance, as discussed in section 2.6. Having this type of flow was an important part of this objective, as it would allow for better comparison between the experimental results and literature.

In order to achieve the wanted aerodynamic features, as well as generate some baseline dataset, three different bodywork designs were created for this test, namely:

1. Baseline bodywork with a full flat floor and no diffuser fitted to the rear of the model.

2. Baseline bodywork with a 15° degree diffuser and 80mm edge radius at the diffuser leading edge.
3. 15° degree diffuser with vortex generators (VG) added ahead of the diffuser leading edge, generating streamwise vortices.

All three bodywork designs are made to fit the radio-controlled car used by Battegazzore. This was an off the shelf Maverick Quantum Flux car, weighing about 2.1 kg and able to reach speeds of well over 15 m/s. The main challenges of this car were its exposed large wheels, which created a very big low pressure wake behind them. This low pressure wake was then drawing the air from inside the diffuser outward, reversing the desired inflow direction inside the diffuser. The new bodywork was designed to fit around the entire RC car subframe, and shield the rear wheels as much as possible. Finally, the design was also adapted to be more in line with the so called Ahmed body's tested frequently in other studies, see section 2.2. This resulted in the baseline bodywork as depicted in figure 5.4 below.

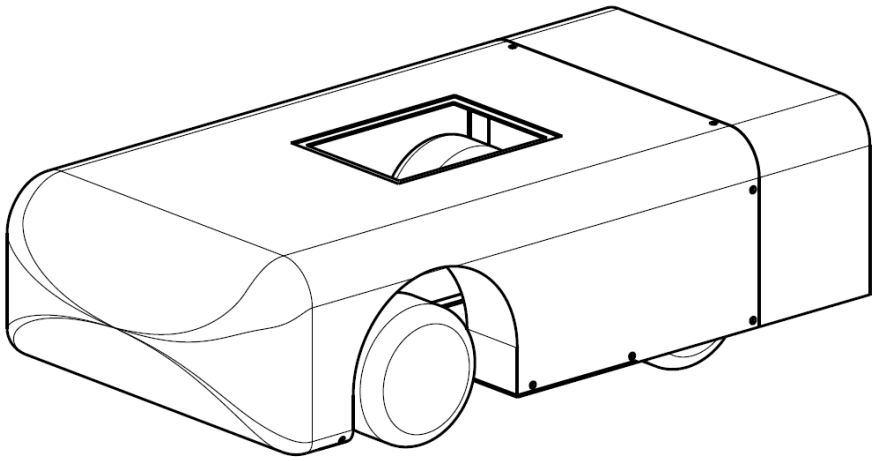

Figure 5.4: Isometric view of the RC car fitted with the new bodywork

For bodywork configurations 2 and 3, a 15° diffuser was incorporated at the rear of the car, which has the same dimensions as the one used by Battegazzore, i.e. 196 mm wide and about 170mm long. This diffuser angle showed to produce the highest flow acceleration under the car out of the angles tested. The only difference with the model of Battegazzore is the addition of an 80mm edge radius applied to the diffuser leading edge. As the work of Battegazzore showed signs of flow separation for a 15° diffuser with sharp leading edge, the edge radius was applied in order to see if this would reduces or negate the separation. A cutout and bottom view of the diffuser equipped bodywork are shown in figure 5.5.

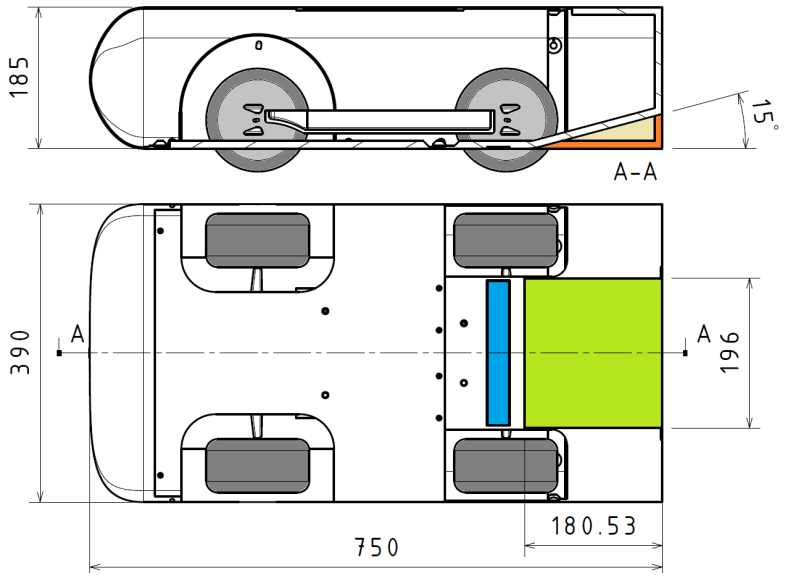

Figure 5.5: Bottom and section view of the diffuser equipped bodywork

The orange part highlighted in the section view of figure 5.5 is the baseline geometry without diffuser. This part is removed to reveal the diffuser on the model (green shaded area) for configurations 2 and 3. Finally, in case flow separation would still be present in configuration 2, a strip of vortex generating fins was placed ahead of the diffuser leading edge, in the blue shaded region of figure 5.5. Their aim was to generate streamwise vortex pairs, which could potentially aid flow attachment at the diffuser start. The strip features 4 pairs of fins, placed at a 30° angle of attack to the incoming flow. A pressure differential between the flow facing side of the fin and the rear facing side promotes the formation of a vortex, along the top slanted edge of the fin. As the fins are positioned in pairs, in alternating nose-in and nose-out orientation, the two vortices generated by a pair should rotated in opposite direction, creating an upwash component in the middle of the pair, and a downwash component between 2 pairs. The dimenions and layout of the vortex generator fins is shown in figure 5.6. Figure 5.7 shows a picture of the vortex generator strips fitted to the bodywork.

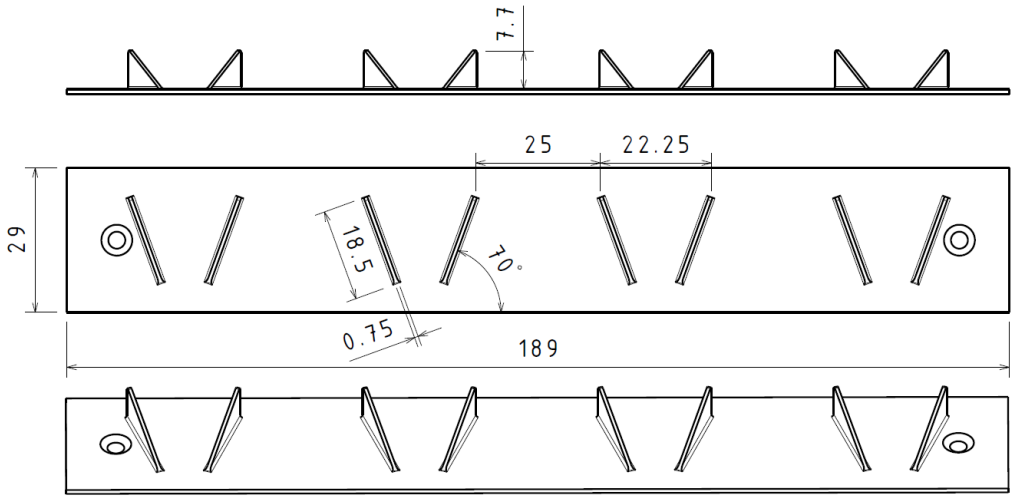

Figure 5.6: Vortex generator strip dimensions

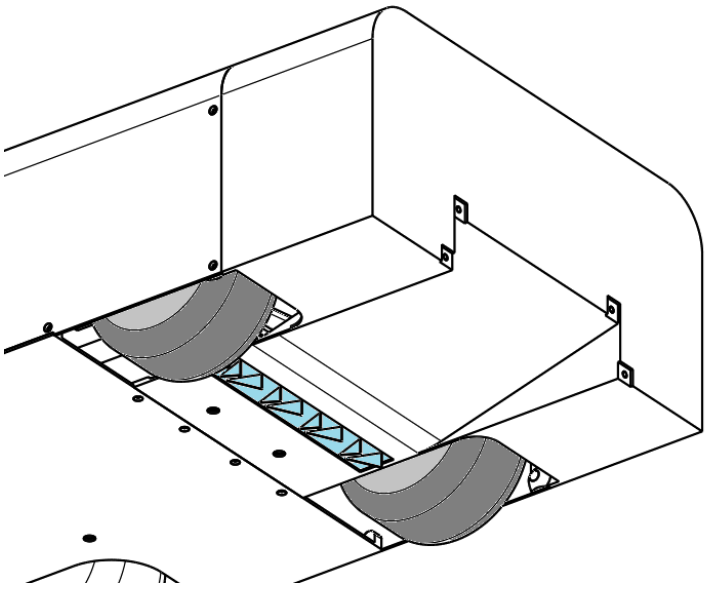

Figure 5.7: Picture of the vortex generator strip fitted to the car bodywork

5.3 Geometric and Volume Self-Calibration

Before the setup can be used to apply the Shake-the-Box algorithm on the images from runs of the car passing through the setup, an important step is making sure that the cameras are calibrated to track particles in the measurement domain. A so called geometric calibration is performed at the start of each day of the measurement

campaign. This calibration step involves taking a set of pictures of a calibration plate with the three cameras located in the shell. A known dot pattern is present on this calibration plate, which the DaVis software uses to construct a 3D space in which it knows the position of the plate and cameras, all relative to each other. With this geometric calibration, DaVis computes a first estimate of the field of view of all the cameras, and where these field of view overlap. The final measurement domain is determined by the overlap between the 3 FoV's, and this domain is initialized in the geometric calibration step. It also generates a mapping function which tells it where objects are in 3D space based on the 2D images captured by the three cameras.

A second important part of setting up the PTV step is a so called volumetric self calibration, introduced by Wieneke in 2008 [30]. After the geometric calibration with the calibration plate, the mapping function will contain triangulation errors that stem from small imperfections in the calibration plate, slight camera misalignment's, etc. In order to perform reliable 3D LPT, it is important that particles can be tracked with sub-pixel accuracy [30]. The volumetric self-calibration procedure is used to refine the mapping functions generated by the geometric calibration, minimizing the disparity between particle positions detected by the different cameras in the RoF setup. The volumetric self-calibration is performed by turning on the seeding rig in the tent, until there is a roughly steady amount of seeding inside the measurement domain. Then, by taking a set of images (no car is being driven through the tent yet), the DaVis software can perform the volume self calibration. The set of calibration images is used to create a disparity map of the measurement volume, by performing 3D particle tracking on the calibration images. This returns a residual triangulation error between the tracked particles and the geometric calibration, allowing for the correction of the mapping function generated from the geometric calibration. With this second calibration, DaVis is capable of correcting for small disparities in where it expects particles to be based on the geometric calibration, and where they actually appear in the three views of the cameras.

After the volumetric self-calibration step, a so-called Optical Transfer Function (OTF) (Schanz et al. 2013 [31]) is generated. This OTF is a way to telling the STB algorithm what a particle looks like, in different camera views, as well as in different parts of the measurement domain. The domain is divided into sub-volumes, for which the OTF function creates a 'standard' particle image of what a particle should roughly look like in that sub-volume, for each camera. Together with the volume self-calibration, the OTF allows for the setup of the STB software, which is now ready to start processing images from car passing runs.

5.4 Testing procedure

With the setup and test model ready, testing could be performed at the High Speed Laboratory of the Delft University of Technology. To test the 3 different bodywork geometries, 3 sets of data "runs" were to be collected. In a run, the car was set to travel at a speed of approximately 7.5 m/s when passing through the measurement domain. A set of runs is recorded by following the next steps:

- Step 1: Close off tent and turn on seeder to start filling the tent with HFSB
- Step 2: After about 60 seconds, check seeding density inside the tent. If sufficient, prepare car to drive through the tent by positioning it several meters in front of the tent.
- Step 3: Prime the cameras and LEDs to start recording/firing when the car passes through the measurement domain. Each run recorded 1000 images at an acquisition frequency of 2 kHz.
- Step 4: Drive the car through the tent, while the front of the tent is opened by an assistant when the car starts driving.
- Step 5: Once the car has passed through the measurement domain, close the front of the tent to keep seeding particles inside, and check if the images are captured.
- Step 6: If car was captured by the cameras, save the images, and reset the car to the front of the tent
- Step 7: Clean the top of the Lexan sheet to remove any bubbles and tire marks stuck on the surface of the Lexan, and prepare the field of view for a next run.
- Step 8: Repeat steps 2 to 7 as many times as runs are wanted for a certain car geometry.

The recording of images is handled by a photo-detector placed just aft of the measurement domain inside the tent. It is a laser beam that, when interrupted by the car driving through it, sends a signal to the control unit of the cameras and LED. The cameras are continuously recording images at 2000 frames per second once primed in step 3 above. The signal from the photo-detector tells the cameras to store a fixed amount of images,

in a time-frame around the signal trigger. The acquisition frequency of 2kHz was chosen based to match the average particle displacement between pictures to be about 10 pixel. This has been shown to work well with the STB algorithm of Schanz [7]. In this experiment, 1000 images per camera were stored from each run, starting approximately 0.1 second before the car passing, and ending 0.5 seconds after that (with the car being in view for roughly 0.2 seconds). This means that some of the flowfield ahead of the car, as well as a larger part of the wake behind the car is captured.

By following this procedure, runs could be performed in relative quick succession, taking about 2 minutes in total per run. The final campaign resulted in 20 runs of data collected for the car model without diffuser (configuration 1), and 30 runs each for configurations 2 and 3 (diffuser with and without vortex generators).

5.5 Experiment setup and imaging overview

Below, table 5.1 summarizes all the relevant equipment and parameters used in this thesis experiment, as well as the corresponding values for the experiment of Battegazzore:

Table 5.1: Overview of the equipment and parameters used for the Ring of Fire setup of this thesis, as well as by Battegazzore [9].

Equipment			
Purpose	Instrument/Parameter	Current Experiment	RoF by Battegazzore
Imaging	Cameras	Photron FastCAM Mini AX 100 (CMOS, 1024 × 1024 pixels, pixel pitch 20 µm, 12 bits)	Photron FastCAM SA1 cameras (CMOS, 1024 × 1024 pixels, pixel pitch 20 µm, 12 bits)
	Objectives	3× AF Nikon f=20mm	2× AF Nikon f=35mm
Illumination	LED	2× LaVision LED-Flashlight 300	1× LaVision LED-Flashlight 300
Seeding	Tracer particles	Helium-filled Soap Bubbles	Helium-filled Soap Bubbles
	Seeding container	Outdoor Tent (9×3×4m)	Wooden C-profile (0.7×1.2×0.5m)
	Seeding system	200 nozzle rig (100 nozzles used)	1 nozzle
Car model	Car speed (m/s)	7.5 ± 0.2	6.0 ± 0.2
	Car length-based Reynolds Number	3.5×10^5	2.8×10^5
Imaging and acquisition parameters			
Purpose	Instrument/Parameter	Current Experiment	RoF by Battegazzore
Field of view	X (car travel direction) [mm]	150	80
	Y (width) [mm]	300	200
	Z (height) [mm]	200	100
Imaging	$f_\#$	16	16
	Magnification	0.05	0.1
	Distance to half domain height (mm)	390	340
	Digital image resolution (mm/px)	0.292	0.255
	Max angle between cameras (deg)	24	70
	Acquisition frequency f_{acq} (kHz)	2	1
Camera and LED settings	Exposure time (µs)	50	110
	LED pulse duration (µs)	50	100
	Images taken per run per camera	1000	300
Seeding concentration	Particle image density (ppp)	0.045	0.04

6. Data Processing

This chapter will cover the processing pipe-line of the data acquired using the on-site Ring of Fire setup discussed in chapter 5. First, the raw images are processed to remove reflections, increase particle intensity and reduce image artifacts. After this, the Shake-the-Box algorithm in DaVis is used to generate particle tracks from the processed images. Thirdly, the particle tracks are transformed into the car reference frame with a Galilean transformation. Particle tracks from all multiple runs are then combined and binned onto a regular grid using a second order polynomial fit, resulting in 3 velocity field datasets, each corresponding to a different geometry configuration. Finally, with the velocity data from the binned data sets, a pressure evaluation method is presented to get an estimate for the pressure distribution around the car model.

6.1 Image processing

As mentioned in section 5.4, each run of the car produced a set of 3000 raw images (1000 per camera), acquired at 2000 Hz. An example of such a raw image is shown in figure 6.1a below, from a run of the car fitted with diffuser and vortex generators.

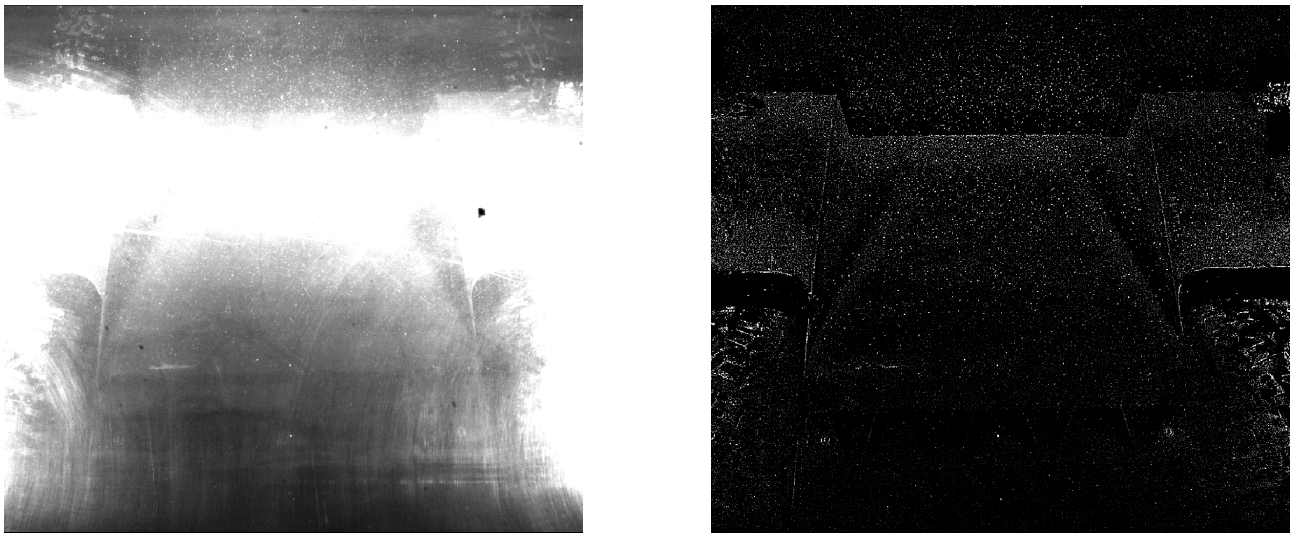

(a) Raw image

(b) Processed image

Figure 6.1: Raw and processed image captured by the center camera of the diffuser equipped model with vortex generators. Raw image intensity range is 10x larger than processed intensity range

The unprocessed image shows the view from the central camera located in the concrete shell. On the left and right of the image the edges of the rear tires are visible, with some tire tracks being left behind on the Lexan. As the tent was filled with HFSB the tires tended to pick up the soap from these particles. This made the tires extra reflective, as shown by the high intensity peaks in the image. Next to the reflections from the tires some reflections from the LED directly onto the Lexan are visible, together with some scratches. As these reflections have a much higher intensity than the light reflected by the HFSBs, it is very hard to see the bubbles in the raw image. As the Shake-the-Box algorithm will detect particles in an image based on their intensity in an image, it is important to process the raw images, trying to reduce reflections and background intensity, while preserving the particle intensities in the image.

To achieve this, a set of pre-processing steps is applied to the raw image. Images are processed through a novel combination of 3 separate filter steps. These filter steps are: A temporal high pass filter, aimed at removing steady reflections. It relies on a so called Butterworth filter, and is described by Sciacchitano and Scarano in 2014 [32]. Secondly, a spatial based filter aimed at removing light reflections from regions where these reflections 'overpower' the light scattered by the HFSB tracer particles. This filter was first developed for removing laser based light reflections in robotic PIV experiments (Galan et al. 2024) [33]. Finally, an anisotropic edge diffusion filter is applied to help reduce (moving) sharp edges such as the soapy tire pattern moving through the image. This filter step is descibed in a PIV setting by Adatrao and Sciacchitano in 2019 [34].

The resulting processed image is shown in figure 6.1b. As can be seen, most of the reflection artifacts are removed from the image, such as the tire tracks and the reflections from the scratched part of the Lexan. Only a small bit of the soapy tires remain, and otherwise mainly light reflected from the actual particles is visible. This makes it much more usable for applying the STB algorithm, which will be explained in a bit more detail in the next section 6.2.

Finally, along the bottom half of the image centerline a set of straight dots might be visible in figure 6.1b. These are not particles, but marker dots painted on the underside of the car model. They have a unique pattern in terms of relative distance, and allow for the tracking of velocity and location of the car model when it goes through the measurement domain, based on the images. This is critical for a later step of transforming the velocity tracks to a car reference frame, as well as give a measure of the car speed for each run. Section 6.3 will go into more detail on this.

6.2 Shake-the-Box Particle Tracking

With the setup calibrated as described in section 5.3, the acquired images from the runs can be processed by the Shake-the-Box algorithm in DaVis. Within DaVis, several settings have been applied in the Shake-the-Box setup to maximize reliable particle tracking based on the image sets. The settings are:

- **Measurement Volume** The measurement volume in which Davis tries to find and triangulate particles. This is generally driven by the outcome of the geometric and volume self calibration, as this is the limit in which DaVis is capable of finding particles. The resulting measurement volume is about 300mm wide, 200mm in the car traveling direction and 200mm tall (X, Y and Z coordinates in the lab reference frame).

- **Particle detection** In order for DaVis to try and triangulate a particle from the images, an image intensity and triangulation error threshold must be set. This tells DaVis how many counts (measure of image brightness) are minimally required to consider a bright spot in the image to be a particle, and the triangulation error tells it how much disparity in 3D space is allowed between the three camera views. The image preprocessing steps discussed earlier are critical here, as they remove bright spots from the image which aren't particles, and allowing the threshold for the particle detection to be lowered enough such that many particles can be detected in the domain. For this experiment a minimal count of 40 is set for 2D particle detection, with a maximum allowed triangulation error of 1 voxel.

- **Tracking velocity ranges** The third important setting for the STB algorithm is the allowed velocity range in which the algorithm might search for particle tracks. A median velocity in x, y and z direction is applied, with a ± range around this median. It has been set to include the expected particle velocity range, in all three dimensions. Any detected particles that fall outside of the supplied velocity range are discarded by the algorithm. This way it acts as a filter for the algorithm to discard "ghost" tracks which are clearly non physical. It is important however to select the right ranges, as it is easy to be too restrictive, and discard real particle tracks that are just outside the specified range. A velocity range of 4 m/s ± 8 m/s is set for the direction of travel for the car model (y direction in the lab frame), and 0 m/s ± 5 m/s in both the x and z direction.

- **Acceleration limits** In combination with the velocity range accepted for tracking, the acceleration limit inside the STB dialog is relaxed to allow for a maximum absolute particle shift between images of 2 voxel, as well as a maximum relative particle shift of 30%. These settings allow for higher particle accelerations between images to be accepted as valid particle tracks. This is especially important regions with high dynamic velocities such as separation or wake areas, or where the particles are being pushed under the car. Here they have a very low initial velocity, which doesn't allow a high absolute velocity change due to the relative acceleration limit. The settings of 2 voxel and 30% proved to be reliable in not clipping important particles, while keeping nonphysical "ghost" tracks to a minimum.

- **Multipass** Finally, to maximize the particle tracking capabilities of the STB algorithm, a 3 step multipass sequence has been applied on the images. A first pass goes through every 3rd image, making it easier to capture slow moving particles which might not be moving enough between single frames to be accurately tracked. Then a backwards pass goes through every image available. This is where the bulk of the particle tracks are being generated. Finally a last pass is performed which tries to connect the particle tracks generated in the previous two passes, making the full particle track dataset.

With the settings explained above, each run is processed in Davis. Before exporting the data, a final filter step in DaVis is applied, namely a spatial median filter. This aims to remove particle tracks that are moving in a way that is significantly different from its neighbors in terms of velocity, acceleration etc. Some care is required in applying it to highly turbulent regions, but it does help reduce some of the ghost particle tracks that might still exist. For this experiment it proved most useful for the slow moving particle cloud that resides in the measurement volume before the passing of the model. Further time steps are not much affected by this filter step, as there are fewer particles in those regions and the flow is more irregular throughout the domain.

Shake-the-Box returns a particle track dataset containing a lot of data per time step (image set). For each particle, it outputs variables such as the x, y and z coordinate of the particle, its velocity in the same three directions, a unique particle ID, and much more. The resulting datasets are stored and exported for further processing.

A visualization of the particle tracks generated is presented in figure 6.2, which is a snapshot of the particle tracks captured with the car nose halfway across the measurement domain.

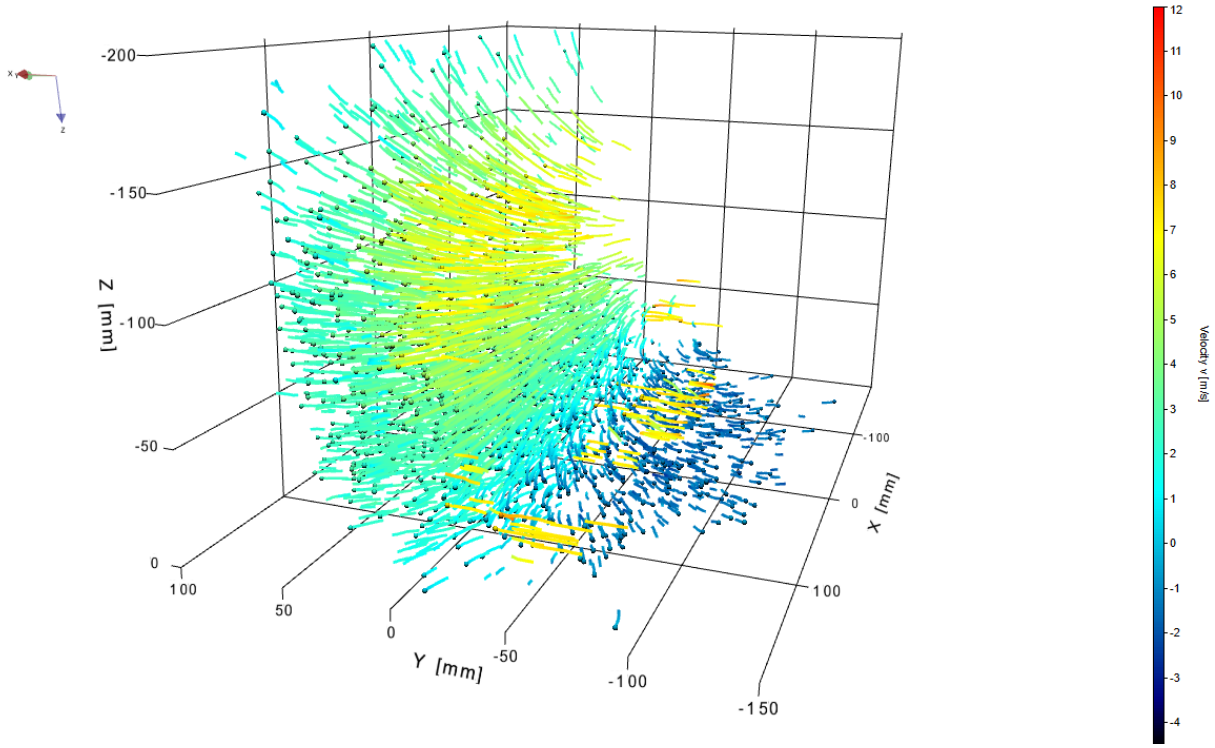

Figure 6.2: Example of particle tracks generated using STB, colored by streamwise velocity

6.3 Velocity Track Processing and Transformation

With the velocity track datasets from each of the runs generated, a processing step is applied which transforms the particle tracks from the stationary camera reference frame, to a moving car reference frame. In order to make the data more easy to understand and compare to results from literature, it is useful to translate it from the static "lab" frame of the cameras inside the shell to the moving car reference frame. This way, the data can be visualized as a flowfield around a static car, as if it was stationary tested inside a windtunnel. To achieve this, a so called Galilean transformation is applied. A Galilean transformation allows for the switch between reference frames which differ in a constant relative motion from each other. In the case of this experiment, it is the car speed which is the relative motion between the car static reference frame and the camera/lab reference frame.

The transformation hence requires an indication of the car velocity, and also depends on the fact that the car velocity is a constant. The last point will not be completely true for this experiment, but for each run, a distance of several tens of car lengths is used to accelerate the car to its set top speed, aiming to reach as good of a constant speed through the measurement domain as possible.

6.3.1 Marker pattern identification

In order to position new velocity tracks to the car reference frame, a car origin has to be established. This is done using the marker pattern, discussed earlier in section 6.1. These markers are placed in a predetermined unique pattern on the underside of the car, with all locations of the markers known on the car model. Using the same steps as discussed in section 6.2, particle tracking is done on the markers. Since the size of these markers is significantly larger than the HFSB used, they scatter much more light, resulting in a higher intensity count on the images. This allows for the minimum particle detection intensity setting to be increased to 150 counts. Together with a much smaller velocity range of 7.5 m/s $\pm$ 0.5 m/s in y direction, the STB algortihm is able to track the markers of the car without tracking HFSB. This generates a new dataset for each run with only the velocity and position of the markers, which is output in the same format as the HFSB particle tracks.

Applying the settings mentioned above, marker particle tracks were generated for each run, resulting in particle tracks such as the ones displayed in figure 6.3 below.

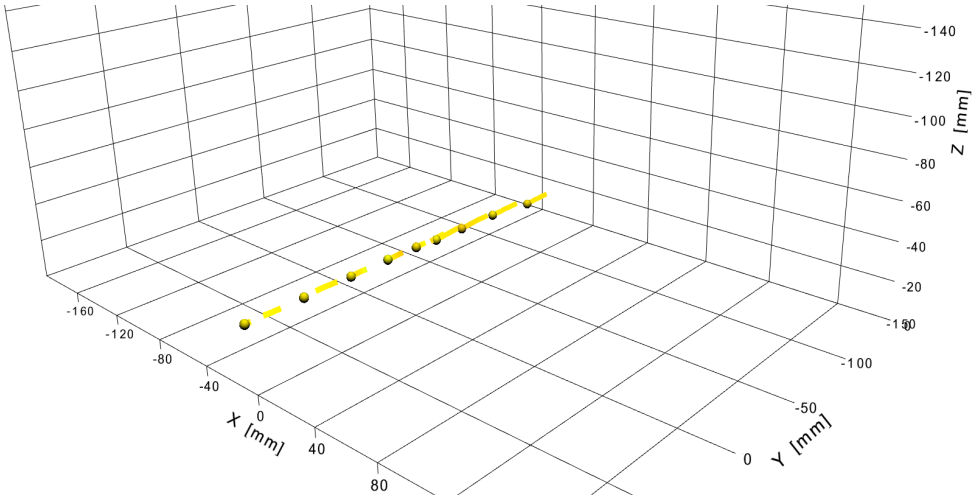

Figure 6.3: Marker particle tracks of the car traveling through the measurement domain.

Now runs can be processed to transform the particle track data from the static to the car reference frame. Firstly, the marker dataset is analyzed, and the car velocity is determined when it traveled across the measurement domain. This is done using a pattern detection script in Python, which is programmed to look for the unique marker spacing pattern put on the car model, identifying which markers are in view in a certain time-step. A pseudo-code is attached in appendix A that outlines the general workings of the pattern detection and marker tracking code.

Taking the average of the marker speed across the measurement domain returns a velocity vector in all 3 directions which is the mean car velocity through the measurement domain for that specific run. A marker placed on the car centerline near the diffuser leading edge is chosen to be the car origin, and this unique marker is used as origin in every run. Its position in the measurement domain at a given timestep (the frame in which the marker is closest to the middle of the measurement domain) is recorded, and will be used as the new origin for the Galilean transformation.

6.3.2 Galilean transformation

Transforming the velocity tracks from the static reference frame to the car reference frame is achieved using the following steps. For all subsequent equations the static reference frame coordinates of the particles are denoted with a prime ($'$) symbol. The transformation accounts for both the car's motion and the chosen car origin, which is the position of a unique marker placed near the diffuser's leading edge. The position of this marker at a specific timestep, t_{ref}, is used as the car origin for the transformation. This reference position, $\mathbf{x}'_{car-origin}$, is recorded in the timestep for which the marker is closest to the measurement domain origin. As the car moves

through the cameras field of view, a simplified snapshot at t_{ref} is shown below in figure 6.4. It shows the car velocity $\mathbf{v}_{car}$, the reference marker on the car underside, colored yellow, and a tracer particle inside the diffuser in blue.

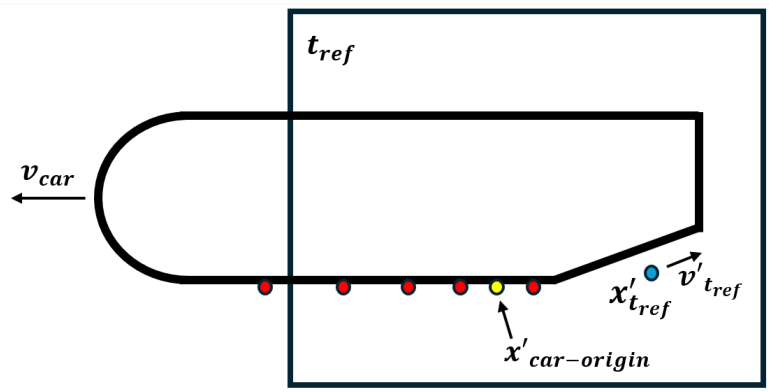

Figure 6.4: Car position and velocity at t_{ref}

For each timestep t, the position of the particles in the car reference frame, $\mathbf{x}(t)$, is computed by subtracting the car origin, $\mathbf{x}'_{car-origin}$, and the displacement of the car due to its motion during $t - t_{ref}$. This displacement is determined using the mean car velocity vector $\mathbf{v}_{car} = (U_x, U_y, U_z)$, calculated from the marker dataset. The particle position vector in the car reference frame $\mathbf{x}(t) = (x(t), y(t), z(t))$ is given by equation 6.1 below:

$$\mathbf{x}(t) = \mathbf{x}'(t) - \mathbf{x}'_{\text{car-origin}} - \mathbf{v}_{\text{car}} \cdot (t - t_{\text{ref}}) \tag{6.1}$$

$\mathbf{x}'(t) = (x'(t), y'(t), z'(t))$ represents the particle positions in the static camera reference frame. Similarly, the velocity transformation adjusts the particle velocities in the static reference frame, $\mathbf{v}'(t) = (u'(t), v'(t), w'(t))$, by subtracting the mean car velocity vector. The velocity transformation is expressed as shown in equation 6.2:

$$\mathbf{v}(t) = \mathbf{v}'(t) - \mathbf{v}_{\text{car}} \tag{6.2}$$

Here, $\mathbf{v}(t) = (u(t), v(t), w(t))$ represents the particle velocities in the car reference frame. These transformations are applied to each timestep of the dataset, ensuring that all particle tracks are consistently expressed relative to the car reference frame.

An example of 3 snapshots from the camera reference frame with a tracer particle and its velocity is shown in figure 6.5, as well as their resulting position and velocity

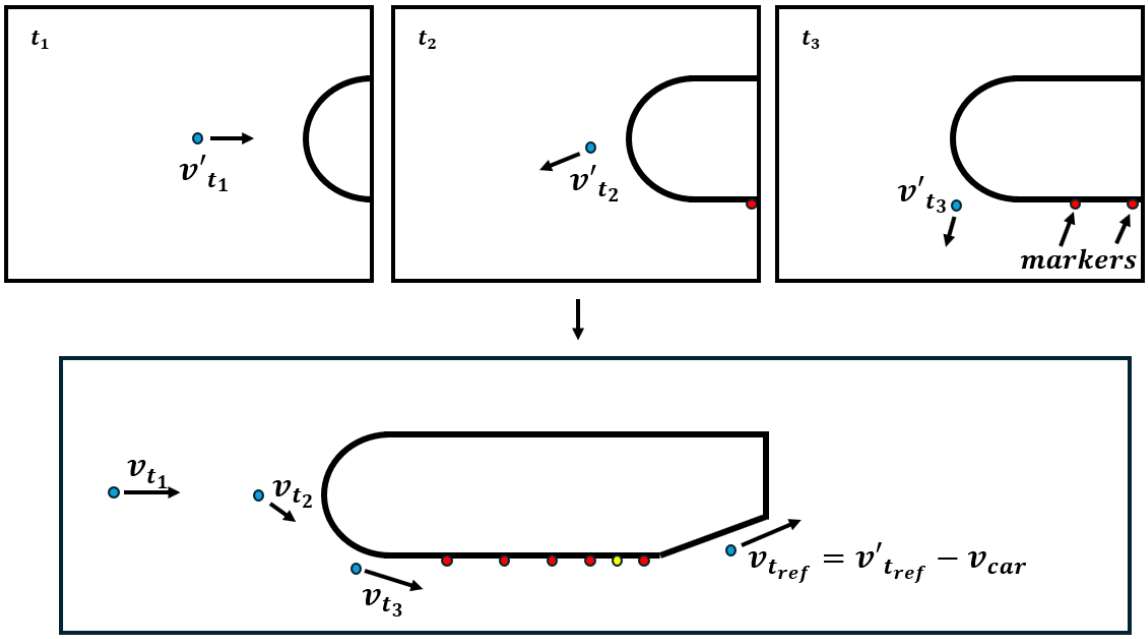

Figure 6.5: Example of tracer particle positions and velocity vectors before and after Galilean transformation

As a final step, velocities in the car's frame of reference are normalized with the car's forward velocity component U_∞, making them dimensionless and more importantly directly comparable between runs with slightly different car speeds. Even though car speed was attempted to be kept as constant as possible, small difference in the order of 0.2 m/s were present between runs, with an average of 7.5 m/s.

The dataset contains particle track data captured over a series of images. These images are acquired at a frequency of 2000 Hz. Consequently, the time interval between consecutive frames, or timesteps, is $\Delta t = 1/2000 = 0.5\ ms$. With 1000 images captured and an average car speed of about 7.5 m/s, this will ultimately result in a flowfield of about 3.75 meters in the car reference frame.

6.4 Mapping onto a Cartesian Grid

With all particle tracks converted and normalized into the car reference frame a so-called binning step (Aguera et al. 2016 [35]) is used to combine the data from multiple runs of the same car geometry (30 for both diffuser equipped model cases, and 20 for the no diffuser model). The results are averaged and put on a regular Cartesian grid. This process is called binning. A domain the size of about 5 car lengths in x direction, 1.5 times the car length in y direction and about 0.2 car length in z direction is setup. It is divided into so called *bins*, which are rectangular grid cells of a certain *binsize*. These bins are used to map the velocity data from the particle tracks onto, and is applied in the following way:

Each individual bin has a certain number of particle track datapoints in the car reference frame located inside it. Based on these velocity datapoints, a 2nd order polynomial is fitted to best represent the velocity distribution within this bin. The value of this polynomial at the center of this bin is taken as the "final" velocity value for that entire bin. This is done for all the bins in the domain, creating a regular velocity field output on a Cartesian grid.

The chosen bin size is dependent mainly on the minimum particle count available in each bin. This is because for the fit of a 2nd order polynomial in the 3D bins, a minimum of 10 particles per bin is required for a polynomial fit to exist, and more particles are ideally required to allow for a reliable polynomial fit. Here it should become clear why multiple runs were done for each geometry. As more and more runs are performed, each run adds particle data throughout the domain around the model. This slowly "fills in" the domain with particle data, increasing the ability to fit polynomials in a smaller and smaller bin size. A smaller bin size ultimately means more independent velocity vectors can be obtained in the domain. To allow for better ability to resolve velocity gradients, which are used to compute variables such as the pressure gradient and vorticity, a bin overlap can be applied. This means that the spacing between bins is smaller than their size. Particle tracks will be included in the polynomial fit of multiple bins, hence not increasing the number of independent data points in the final bin.

With the data acquired in this experiment, a final bin size of 7mm was achieved. At this size, practically all areas of interest, such at the floor and diffuser center region had sufficient particle density to reliably fit the 2nd order polynomial. To help with resolving the velocity gradients in the flow, a 75% overlap was used, meaning that individual bins are spaced 1.75 mm apart.

Below, figure 6.6 shows a slice along the car centerline with a contour plot of the number of particles inside each bin. Almost all of the domain underneath the car is filled with at least 100 particles per bin, only a small region near the diffuser leading edge and the vortex generators drops towards the minimum of 10 particles per bin.

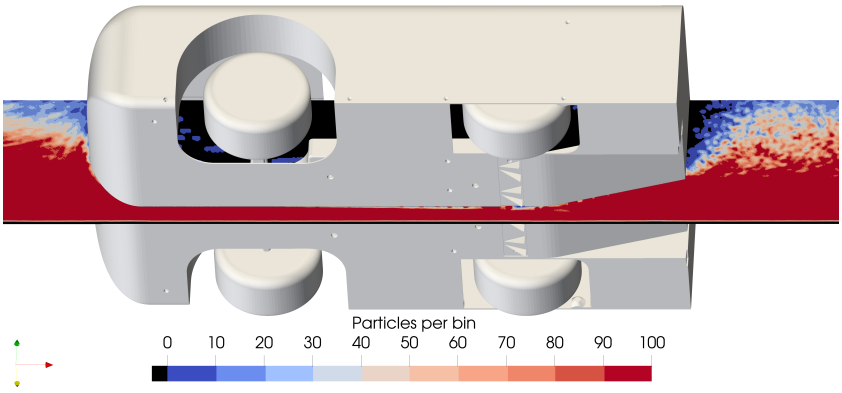

Figure 6.6: Particle distribution along the car centerline for diffuser equipped model with VG's

Figure 6.6 does however only show the distribution along the car centerline. A slice through the spanwise direction of the diffuser shows that in the diffuser corners, particles are not tracked as well, and/or there might be fewer particles present. This means that the number of particles per bin drops below 10 towards the corners of the diffuser, and there will be no data in the final binned dataset. Figure 6.7 clearly illustrates this lack of particles in the upper diffuser corners.

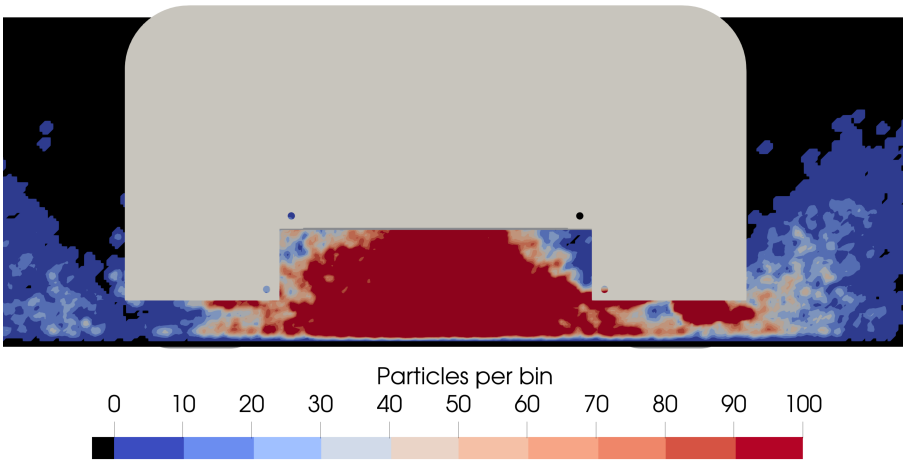

Figure 6.7: Particle distribution inside the diffuser of the car model equipped with VG's

6.5 Pressure Field Calculation

As 3D LPT generates velocity and acceleration data for particle tracks, the main output of this experiment is the velocity field around the car model. However, as discussed in chapter 2, the pressure distribution around a car is ultimately what drives the downforce generated by a car. Hence, being able to convert the velocity track data into pressure field information is a welcome addition to the output of this experimental setup.

A logical starting point of computing pressure from a velocity field is by applying Bernoulli's equation. This states that for a steady, incompressible and inviscid flow, the total pressure, consisting of the static pressure p and dynamic pressure q, remains constant along a streamline. When the flow is irrotational, the total pressure within a domain is constant everywhere, not only along a streamline. The pressure coefficient is defined by equation 6.3 below.

$$C_P = \frac{p - p_\infty}{\frac{1}{2}\rho_\infty U_\infty^2} \tag{6.3}$$

As mentioned in chapter 2, the pressure coefficient C_P when applying Bernoulli can be written as:

$$C_p = 1 - \left(\frac{u}{U_\infty}\right)^2 \tag{6.4}$$

Here, u is the local velocity, and U_∞ is the freestream or reference velocity. As all velocities are already normalized with the car speed after the Galilean transformation step, this definition of C_P can be directly applied in the entire flowfield. However, this would imply that Bernoulli's principle is applicable everywhere around the car. The flow inside the diffuser can still be considered inviscid and incompressible, however it is no longer irrotational. This means that equation 6.4 can not simply be applied in the whole domain. There are several other methods available to obtain a pressure field from a 3D velocity field, for example using a Poisson solver, as discussed by van Oudheusden (2013) [36]. The reconstruction of a pressure field from a 3D velocity field using a Poisson solver is possible but presents significant challenges, particularly for complex geometries such as the flow around a car. The Poisson equation for pressure, derived from the incompressible Navier–Stokes equations, is given by equation 6.5 below [36]:

$$\nabla^2 p = -\rho \nabla \cdot (\vec{u} \cdot \nabla \vec{u}) \tag{6.5}$$

While numerical methods exist to solve this equation, its practical implementation depends heavily on boundary conditions and velocity field accuracy. The Poisson equation requires well-defined boundary conditions on all sides of the domain. For external flows, like around a car, specifying physically meaningful pressure

or pressure gradient conditions at all boundaries is difficult. The Poisson solver also assumes a structured computational domain in which the flow field is well defined. Real-world geometries, such as the tested car floor and diffuser region, introduce discontinuities and flow separations. This makes numerical discretization more complicated and can introduce inaccuracies in the pressure field.

For this experiment, a pressure gradient integration method is used. A C_P value close to the ground is calculated using Bernoulli's principle and equation 6.4, after which this C_P is integrated in positive z-direction using a pressure gradient computed using velocity gradients obtained from the binned velocity field data.

Starting from the conservation of momentum in the Navier-Stokes equation, one can write for the the z direction:

$$\frac{\partial w}{\partial t} + (\vec{u} \cdot \nabla)w = -\frac{1}{\rho}\frac{\partial p}{\partial z} + \nu\nabla^2 w \tag{6.6}$$

Liu and Katz (2006) [37] have shown that the contribution of the viscous term $\nu\nabla^2 w$ is negligible when computing pressure gradients for a relatively high Reynolds number flow. As the flow inside the centerline of the diffuser will be largely inviscid, the viscous term is thus omitted from the calculation of the pressure gradient.

Using Reynolds decomposition, one can write the velocity components and pressure as the sum of a mean and a fluctuating component, i.e. $w = \bar{w} + w'$. By definition, the change of the mean velocity components over time is 0 for a steady flow. Hence the $\frac{\partial \bar{w}}{\partial t}$ term drops out of equation 6.6. The 3D particle track data gives some indication on the magnitude of the velocity fluctuations w', represented by the standard deviation. This standard deviation around the mean velocity in a bin can be seen as $||w'||^2$. As the magnitude of the standard deviation is much smaller than the mean velocity component, their contribution to equation 6.6 in the form of $\frac{\partial w'}{\partial t}$ is negligible, and thus neglected.

Substituting the Reynolds decomposed velocity components into the convective term $(\vec{u} \cdot \nabla)w$ of equation 6.6 results in a convective term of the mean velocity components, i.e. $(\vec{\bar{u}} \cdot \nabla)\bar{w}$, and a set of Reynolds stress terms. These terms are the product of the velocity fluctuations $\vec{u'}$ and the spatial derivatives of w'. These Reynolds stresses are usually very small if turbulence effects are low. Hence these are terms are also omitted from the pressure gradient computation, resulting in the following equation 6.7 below:

$$\frac{\partial p}{\partial z} = \rho\left(\bar{u}\frac{\partial \bar{w}}{\partial x} + \bar{v}\frac{\partial \bar{w}}{\partial y} + \bar{w}\frac{\partial \bar{w}}{\partial z}\right) \tag{6.7}$$

This relates the pressure gradient in z direction to the mean convective terms of the momentum equation. It allows for the computation of $\frac{\partial p}{\partial z}$ from the binned velocity datasets, where the binned velocity data is taken as the mean velocity vector, $\vec{\bar{u}}$. With this, an integration scheme is applied which takes a starting value of C_P calculated using Bernoulli's principle from equation 6.4, calculated at a small height above the ground plane, namely 3.5mm from the ground. Here, Bernoulli's principle should hold the best throughout the entire length of the domain, especially in the center region of the model, in terms of being steady, inviscid and irrotational flow.

From equation 6.3, one can write $\frac{\partial C_P}{\partial z}$ in terms of $\frac{\partial p}{\partial z}$ to equation 6.8:

$$\frac{\partial C_P}{\partial z} = \frac{2}{\rho U_\infty^2}\frac{\partial p}{\partial z} \tag{6.8}$$

Hence, starting at a height of 3.5 mm from the ground surface, a base $C_P(z = 3.5mm)$ value is computed, and iteratively integrated along the z-axis, following equation 6.9.

$$C_P(z_{i+1}) = C_P(z_i) + \left(\frac{\partial C_P}{\partial z}(z_i) \cdot \Delta z\right) \tag{6.9}$$

Equation 6.9 is a basic forward Euler numerical integration scheme. There are several other more advanced ways to integrate a pressure gradient from PIV-based methods. For example, Liu and Moreto (2020) [38] describe a method to minimize the error of the pressure gradient integration by using omnidirectional integration methods. Here multiple integration directions are used, originating from different starting points, to approach the point in which the pressure needs to be computed, instead of using a single straight vertical line, as is done in equation 6.9. This omnidirectional integration method does increase the integration scheme complexity. Hence, in order to keep the computation and implementation simple, the forward Euler scheme is chosen for this experiment. The uncertainty of the method used will be discussed in more depth in section 7.3.2.

7. Results

This chapter will present the results from the experimental campaign. First, section 7.1 will present the velocity field around the car model, focusing on the macroscopic behavior of the velocity profiles along the car centerline. An overview of the flow inside the diffuser is given, along with a comparison between the flowfield in the diffuser with and without vortex generators. Next, section 7.2 will present the results of the pressure evaluation technique discussed in chapter 6.5, and will highlight the differences in pressure coefficient C_P for each geometry option. Finally, section 7.3 will discuss the uncertainty of the velocity and C_P data, and convergence of the results based on the number of runs performed per geometry.

7.1 Velocity Field

As highlighted in chapter 2, flow acceleration and lowering the static pressure underneath a diffuser equipped car is important in its ability to generate downforce. With the floor interacting as a converging channel with the ground, and the diffuser section providing an expansion region, flow is accelerated under the car, at the start of the floor and near the diffuser leading edge. This reduces static pressure below the vehicle, generating downforce, adding performance to the (race)car. The resulting typical pressure coefficient distribution is shown in figure 2.4 from Marklund [12]. The effect of changing diffuser angles on the velocity fields is visualized by Battegazzore in figure 3.9 [9].

This section will cover the velocity distributions around the different car models obtained from this experiment. All velocities are normalized with respect to the car velocity U_∞, as mentioned in chapter 6. The streamwise and lateral coordinates are divided by the flat floor length of the no diffuser equipped model, L_B, which measures 688 mm. Vertical coordinates are normalised with respect to the cars nominal rideheight $h = 22mm$.

7.1.1 Full flowfield around model

With the data captured for this experiment, three 3D velocity datasets are available that represent the flowfield around the car model. Figure 7.1 shows streamlines colored by normalized streamwise velocity around the diffuser equipped car model.

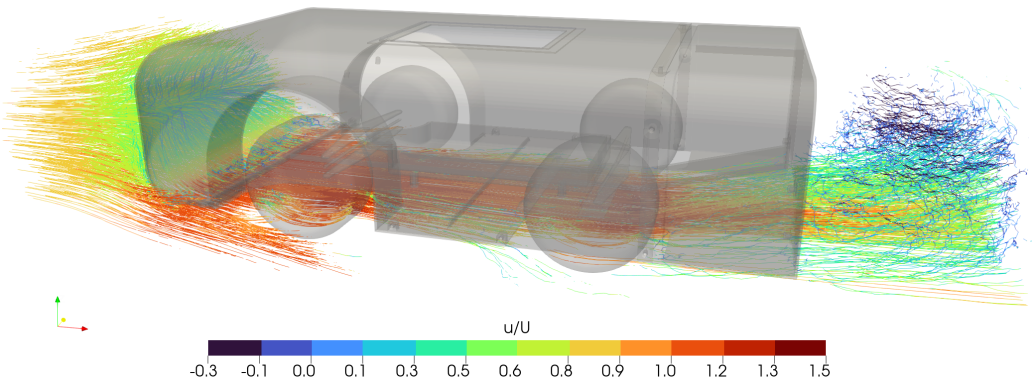

Figure 7.1: Streamlines colored by normalized streamwise velocity around car equipped with diffuser

Following the streamwise flow direction, there is a stagnation region at the cars nose, about halfway up the

body height. Flow at the car centerline is directed under the floor, where it accelerates to a velocity above freestream U_∞. Some is deflected around the front wheels, and some outflow between the front and rear axle is also present. At the diffuser inlet, the flow is accelerated again, before being expanded in the diffuser. Here it starts decelerating in streamwise direction, while increasing its vertical velocity. Behind the vehicle, flow exits the diffuser at an upward angle, entering a low velocity turbulent wake which follows the back of the model. Flow reversal in the upper part of the wake indicates a separation region behind the car.

Figure 7.2 shows the streamlines underneath the diffuser equipped model, as well as a contour plot of the streamwise velocity component, normalized with the car velocity U_∞.

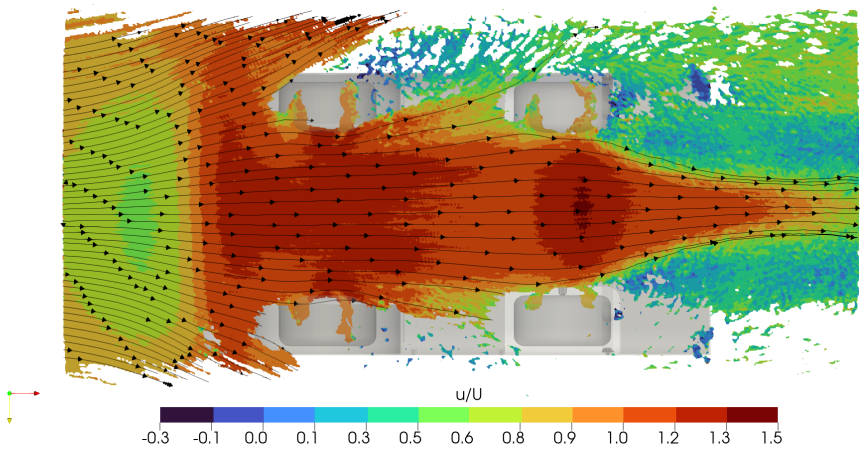

Figure 7.2: Normalized streamwise velocity contour plot with streamlines under diffuser equipped model, at $z/h = 0.12$

The flow approaching the car is split in a center section which moves under the model, and two sections moving laterally outboard the car, around the front tires. Flow travels fairly straight between the front wheels, after which the streamlines slightly expand laterally. Some outflow between the front and rear tires is visible. Approaching the diffuser section of the car, streamlines are converging towards the car and diffuser centerline, just after the rear axle. Within the diffuser, streamlines are contracted towards the diffuser center, indicating that there is inwash into the diffuser behind the rear tires. This pattern of contracting streamlines is quite different from the outwash observed in the diffuser used by Battegazzore, presented in figure 3.10, but is more in line with the flow patterns observed in figures 2.8 and 3.2.

7.1.2 Centerline normalized streamwise velocity

The normalized streamwise velocity field around the car models tested for this experiment are shown in figure 7.3. It shows a contour plot along the car centerline, including some of the upstream flowfield and wake behind the car.

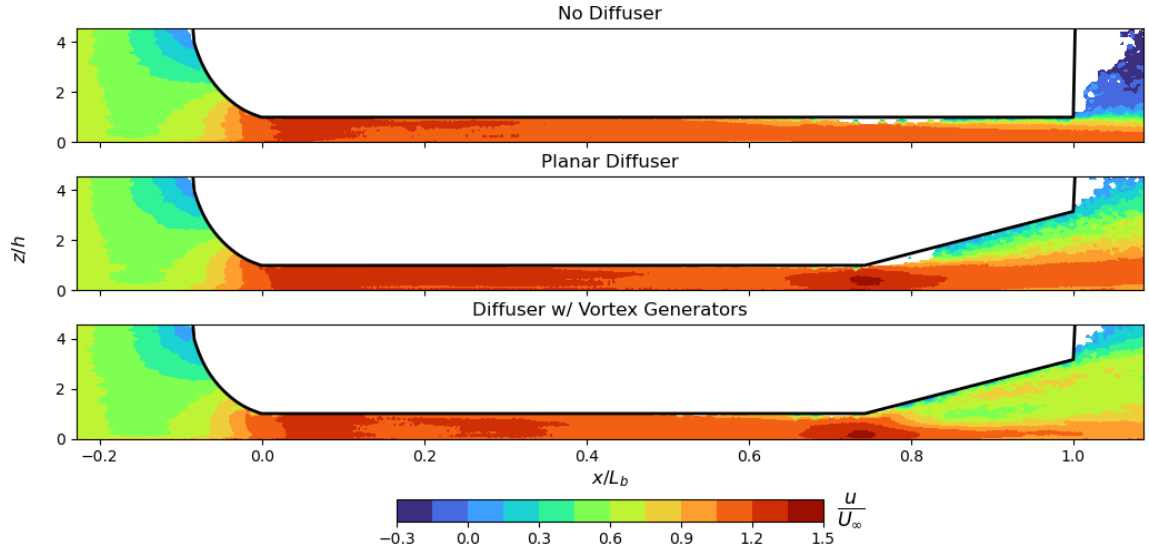

Figure 7.3: Normalised streamwise velocity contours around different car model geometries

All 3 geometries are showing a similar velocity trend at the forward part of the car. The flow is decelerated below freestream U_∞, approaching the car, with a stagnation point near the nose leading edge. As the flow is pushed under the nose to the start of the flat floor section of the car, an acceleration peak is present just after the transition from the curved nose to the flat underfloor, at x/L_B. Here velocities peak at around 1.25 times U_∞. The velocity distribution is relatively uniform in the z-direction, until the diffuser leading edge. The following subsections will discuss the differences in streamwise velocity between the 3 tested car geometries that appear from $x/L_B \approx 0.6$ onward.

7.1.3 Centerline velocity field around model with a flat floor

Keeping with the top contour plot of figure 7.3, following the flow under the car, the model without a diffuser shows a gradual velocity decrease going along the entire length of the floor, dropping to roughly 1.05 times U_∞ at the floor trailing edge. A wake with flow reversal is visible behind the car, $x/L_B > 1.0, z/h > 1.0$, located above the streamtube where $u/U_\infty > 1.0$ which continues from under the floor. The distribution of the velocity in z direction remains relatively uniform under the floor, until around $x/L_B = 0.6$, where a deceleration near the car surface is visible. This could be an indication of a thick boundary layer developing, but is more likely be due to the fact that the 3D printed car bodywork wasn't extremely rigid, and could have been pitching tail down due to the car's forward motion. If any part of the bodywork would have been tracked as particles, this would result in a particle with a streamwise velocity of 0 after the Galilean transformation, hence affecting the velocity binning to show a decrease in velocity. As the final bin size of 7 mm is in the same order as the thickness of a flat plate boundary layer developed over a 0.7 m length and freestream velocity of 7.5 m/s, the velocity gradient is likely to be caused by the car pitching down, instead of it being the actual boundary layer under the car.

Finally, behind the car there is some of the wake that is captured by the Ring of Fire setup. The setup does however struggle to capture particle tracks immediately behind the car, as highlighted by the white areas behind the car body. Here there will be some region that is obscured from the camera view as the car passes through the measurement domain. This is due to the fact that the cameras are pointed slightly towards the car starting position, i.e. the car drives towards the sensor. The car underbody produces an optical occlusion in the near wake of the car, thus precluding flow measurements in that region. This could be solved by using cameras above ground looking from the side of the measurement domain, but resolving the wake behind the vehicle is not the aim of this experiment.

7.1.4 Centerline velocity field around model with diffuser

Looking at both diffuser equipped models in figure 7.3, the velocity field starts to differ from the no diffuser model when approaching the diffuser leading edge (at $x/L_B = 0.75$). Instead of continuing to decelerate slowly towards the freestream velocity, a second velocity peak is observed at the diffuser leading edge. For the diffuser without vortex generators, a peak velocity of around 1.4 times U_∞ is reached close to the model surface. This is faster than the velocity peak at the start of the floor.

For the vortex generator strip model, a slightly lower streamwise velocity peak is reached, just under $u/U_\infty = 1.3$ close to the model surface. It does reach $u/U_\infty = 1.4$, but only very close to the ground, compared to the no vortex generator model. A more detailed comparison between the two diffuser models is discussed in section 7.1.6.

Once the diffuser starts, the centerline velocity fields of the two diffuser equipped geometries begin to differ slightly. The z location of the diffuser leading edge velocity peak is not the same between the two geometries, with the VG equipped diffuser having a peak closer to the ground plane compared to the no VG equipped diffuser geometry.

Still comparing the middle and bottom contour plots of figure 7.3, for the car model without vortex generator, a stream tube about the height h (where h is the distance between the flat floor section of the car and the ground plane) remains almost horizontal throughout and beyond the length of the diffuser, slowly decelerating towards U_∞. Throughout the diffuser, there is a clear velocity gradient in positive z-direction above this streamtube, where the streamwise velocity slowly decreases towards 0.0 u/U_∞ close to the diffuser surface. Comparing the streamwise velocity magnitude at $x/L_B = 0.9$ and $z/h = 1.0$, the planar diffuser without VG's has $u/U_\infty \approx 1.0$, while the diffuser with VGs drops to $u/U_\infty \approx 0.5$.

The wake immediately behind the model does not show the same amount of flow reversal at the height of the diffuser exit as the no diffuser, flat floor model. This indicates that the diffuser is providing some recovery of the flow velocity towards the freestream velocity.

In the case of the model equipped with vortex generators, there is not as much of a velocity gradient throughout the diffuser height, along the car centerline plane. In this case, the decelerating streamtube that carries on more or less horizontal in x is about half the height of that observed for the diffuser case without vortex generators. Looking at the velocity variation in the z direction, above the horizontal streamtube there is a small deceleration and then a small acceleration again when approaching the diffuser roof. The streamwise velocity component close to the diffuser surface has a higher velocity (around 0.75 times U_∞) for the car with vortex generators, compared to the car without vortex generators decelerating towards 0.0 - 0.1 times U_∞.

In order to further illustrate the difference in streamwise velocity between the three tested geometries, figure 7.4 below shows streamwise velocity profiles at different x/L_B locations under the car. The solid grey line represents $u/U_\infty = 0.0$, where the dashed grey line is $u/U_\infty = 1.0$. Clearly, the diffuser with VG's shows the higher streamwise velocity closer to the top of the diffuser, compared to the diffuser without VG's.

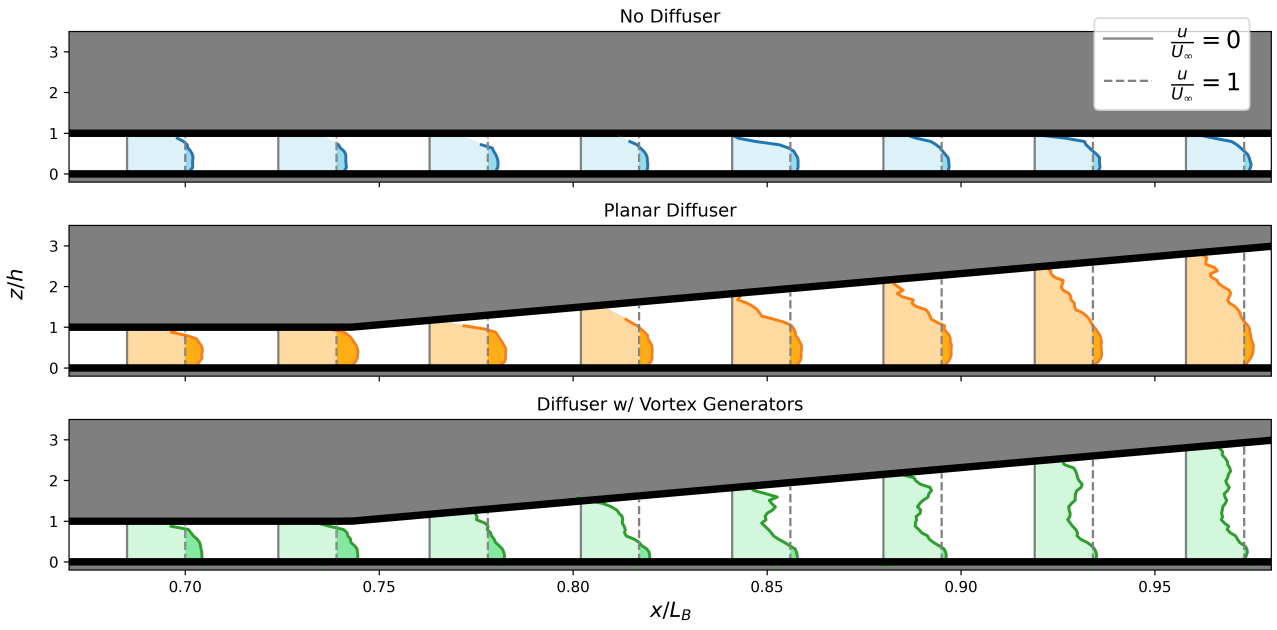

Figure 7.4: Streamwise velocity profiles at different x/L_B locations

7.1.5 Total velocity magnitude underneath car centerline

When plotting the velocity magnitude (the sum of all three velocity components) along a line positioned at $z/h = 0.5$ the difference between all three different model geometries is clear. Figure 7.5 below shows the normalized velocity magnitude in x along the car centerline for all 3 model configurations.

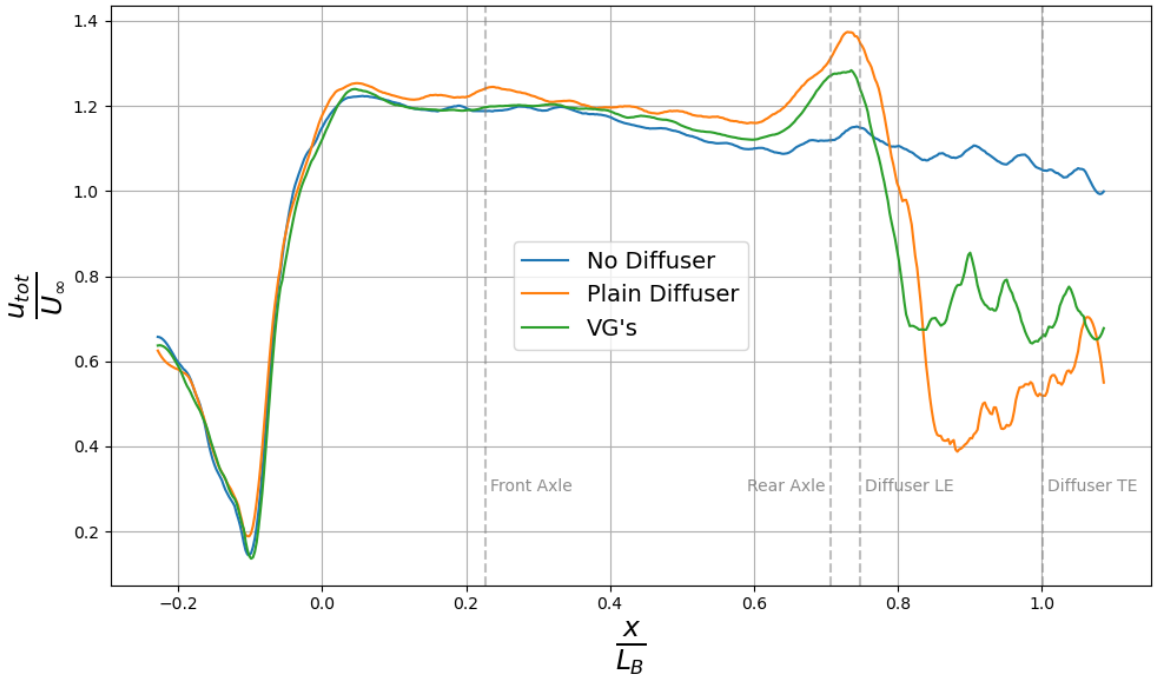

Figure 7.5: Normalized velocity magnitude along car centerline at $z/h = 0.5$ below the car surface

As discussed above, the velocity profile between the geometries does not vary much for the part under the car upstream of the diffuser leading edge. This is in line with the observations from literature, as for example Cooper et al. [4] showed that adding a planar diffuser to a bluff body only altered the flowfield from just ahead of the diffuser leading edge onward.

Both diffuser equipped models show a second velocity peak at the diffuser leading edge, with a difference in velocity magnitude throughout the diffuser height between the car with and without vortex generators. In the wake, i.e. behind the diffuser trailing edge $x/L_B > 1$, the velocity is plotted at the height of the trailing edge of the vehicle, which is $z/h = 1.0$ for the no diffuser equipped model, and $z/h = 3.15$ for both diffuser equipped models. Here the flow in both the diffuser-equipped models recover to roughly the same streamwise velocity magnitude, while the flow behind the no diffuser car has a much clearer separation between a relatively high velocity streamtube low to the ground ($z/h < 1.0$) and the wake behind the car above it.

Below, table 7.1 shows the distribution of the maximum velocity magnitudes at different x locations around the car, for the three different geometries.

Table 7.1: Normalized velocity magnitude u_{tot}/U_∞ at different points around the tested car geometries

	Floor LE	**Diffuser LE**	**Car TE**
No Diffuser	1.22	1.15	1.05
Plain Diffuser	1.24	1.38	0.52
VG's	1.25	1.30	0.66

The total velocity magnitude at the diffuser leading edge is slightly lower for the VG diffuser case, compared to the plain diffuser. This suggests that the VG's are introducing vortices that lower the total velocity magnitude, indicating that there is some loss of energy in the flow. As long as the VG's are not resolving flow separations inside the diffuser, it is likely that the added streamwise vortices do not contribute positively to the performance of the diffuser, and only act to convert some streamwise momentum into vertical and lateral momentum, with additional energy losses due to viscous effects.

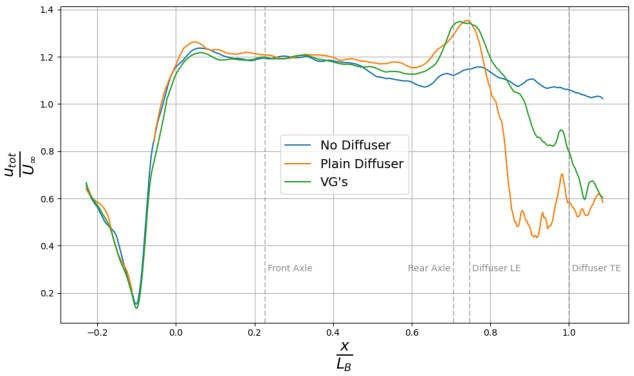

(a) $y = 14$ mm

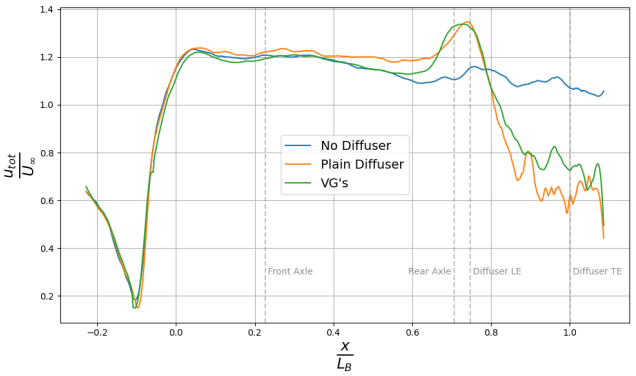

(b) $y = 24.5$ mm

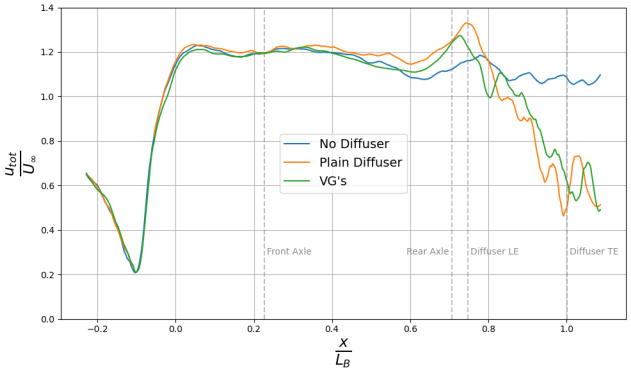

(c) $y = 49$ mm

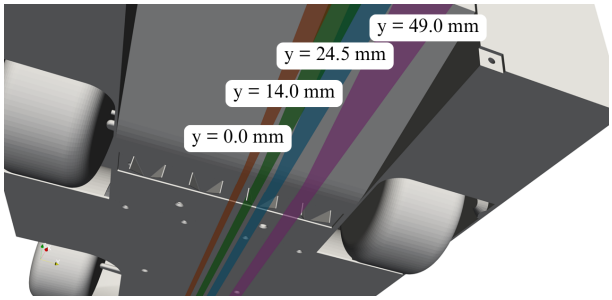

(d) Lateral positions of velocity plots with respect to car model

Figure 7.6: Normalized velocity magnitude at $z/h = 0.5$ below the car surface for different lateral positions

Looking at the total velocity magnitude at different spanwise locations under the car, displayed in figure 7.6 above, the observations remains mostly the same to the once made on the centerline velocity profiles. Both diffuser geometries produce a velocity magnitude peak at the diffuser inlet, and a gradual deceleration of the flow inside the diffuser. At the spanwise location $y = 14.0$ mm, figure 7.6a, the distinction between a higher total velocity through the diffuser for the model equipped with VG's still exists, as it did at the car centerline velocity profile. At the more outboard sections of the car, figures 7.6b and 7.6c, this distinction is not present any more at this particular distance from the car surface ($z/h = 0.5$). A further discussion of the differences between the flowfield inside the diffuser will be given in section 7.1.6 below.

7.1.6 Flowfield inside diffuser with and without VG

Streamlines of the flow inside the diffuser are shown in figure 7.7. The figure highlights the streamlines following the upwashing shape of the diffuser, with the earlier discussed decrease in streamwise velocity due to the expansion of the flow.

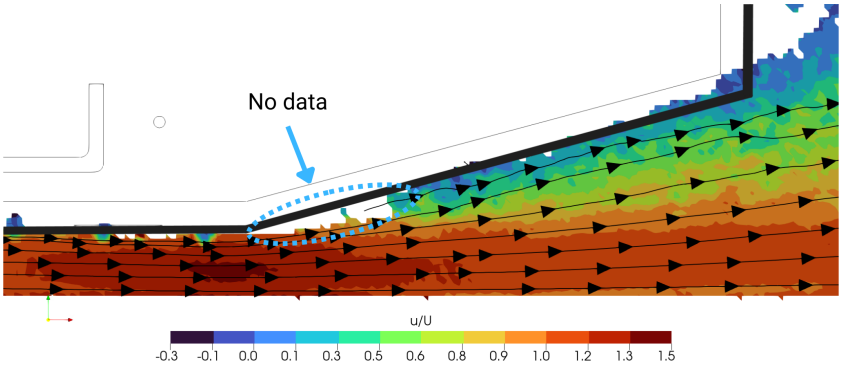

Figure 7.7: Streamlines in the diffuser section of the car model without vortex generators at $y = 0$

There is a region where there are not enough particles tracked in a bin sample to generate velocity data. This region sits just after the diffuser leading edge, near the surface of the diffuser. In the work of Battegazzore (2024) [9], a region of separation was observed for diffuser angles of 15° and 20°, with a similar section of no particle track data. Streamlines curved quite sharply around this region of no data, as shown in figure 7.8a. This was even more pronounced on the 20° diffuser angle, and the high upward curvature of the streamlines suggested a low pressure area, caused by flow separation.

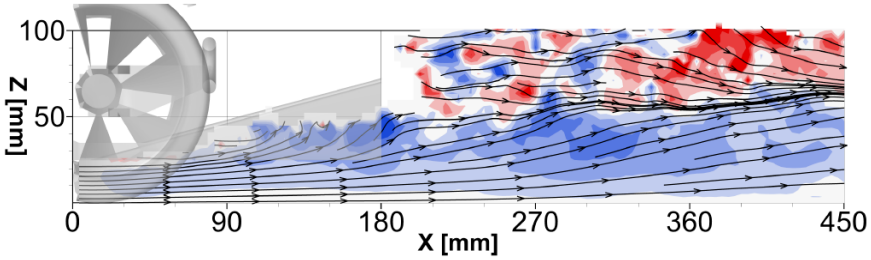

(a) Streamlines of 15° diffuser tested by Battegazzore [9]

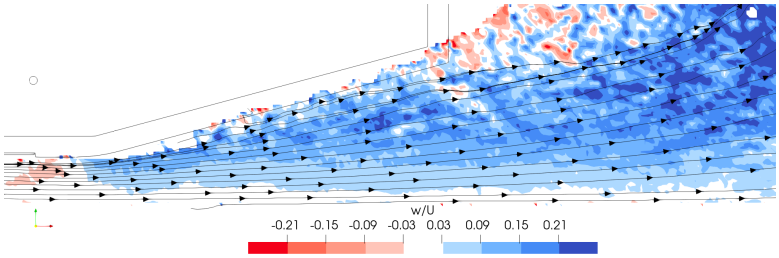

(b) Streamlines of 15° diffuser from current experiment

Figure 7.8: Normalized vertical velocity component inside diffuser comparison between Battegazzore and current experiment

Comparing the data from the 15° diffuser used in this experiment, figure 7.8b, there is also a region of no data near the diffuser surface for this experiment. There is no curvature of the streamlines around this region visible. In fact, all streamlines appear to follow the constant 15° angle of the diffuser. This suggests that the large separation observed by Battegazzore is not present in the diffuser tested for this campaign. However, there might still be a small laminar separation bubble present near the diffuser leading edge. This would explain the region of no data, as there is a very small change of particle tracers ever entering the separation bubble.

Looking at the relative ride height h of the model in comparison to half of the diffuser width d, $h/d = 0.24$. Figure 2.7 from Senior et al. [5] showed that the model is operating near the maximum downforce ride height

for this diffuser half width, and the formation of separation bubbles have been observed near this minimum C_L. The figure comparing the effect of ride height on diffuser downforce is repeated below:

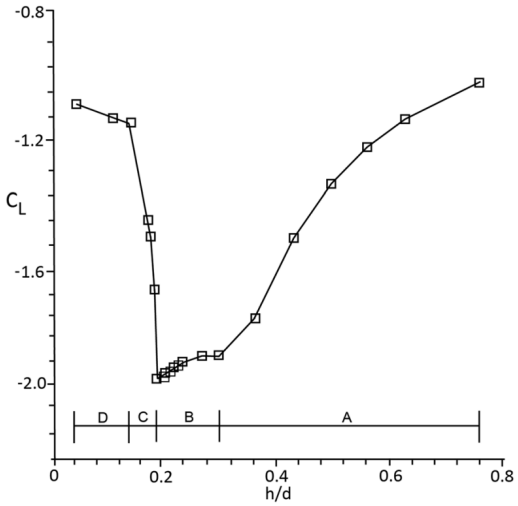

Figure 7.9: Effect of ground proximity on diffuser downforce [5]

Both experiments used the same size diffuser, with similar ride height and car velocity. The big difference in flow attachment observed between this experiment and the result of Battegazzore can be due to multiple reasons. The diffuser used in the current experiment did have an 80 mm edge radius applied to it, compared to the sharp edge at the diffuser start used by Battegazzore. It is possible that this radius resolved the separation in the diffuser, by reducing the initial high adverse pressure gradient induced by the sharp edge at the start of the diffuser. Secondly, the outflow towards the wake of the rear tires on the model of Battegazzore, deflecting the streamlines laterally, thus causing an additional adverse pressure gradient. Since the model used in this experiment has much more shielded rear tires, there is no longer any outflow laterally inside the diffuser, as demonstrated in figure 7.2 earlier.

As can be seen in the streamwise velocity contour plots of figure 7.3, there is no region of missing data in the VG diffuser case. Hence, it is possible that the vortex generators added to the model are reducing the size of, or even eliminating the separation bubble near the diffuser leading edge. From the velocity magnitude close to the diffuser surface, it is clear that adding VG's to the model moves higher velocity air close to the diffuser surface. This is apparent from figure 7.10 below, as a clear shift of high velocity flow close to the to of the diffuser volume.

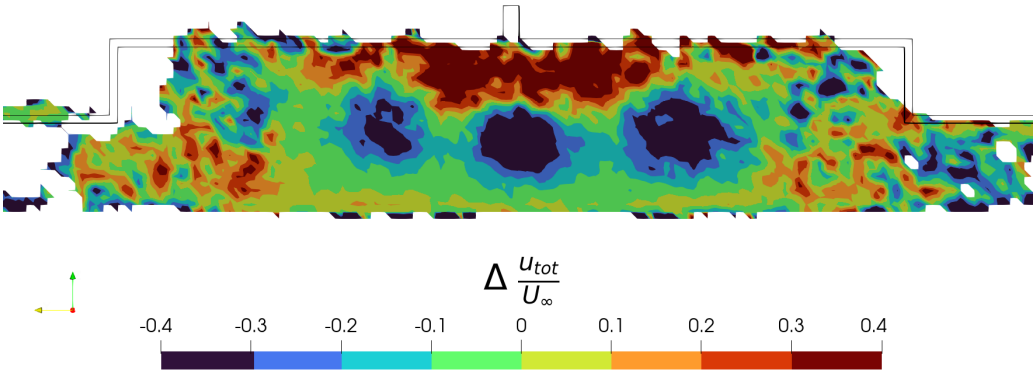

Figure 7.10: Difference in velocity magnitude u_{tot}/U_∞ by subtracting u_{NoVG}/U_∞ from u_{VG}/U_∞ at $x/L_b = 0.83$

In order to assess the flow inside the diffuser, and the difference caused by introducing the VG strip, a series

of velocity contour plots is presented that cut through the diffuser section of the car at different x locations. Figure 7.11 shows streamwise normalized velocity contours with velocity vectors at three different x locations inside the diffuser body. On the left side the slices from the model without vortex generators are presented, and the right side are the results from the car geometry fitted with vortex generators.

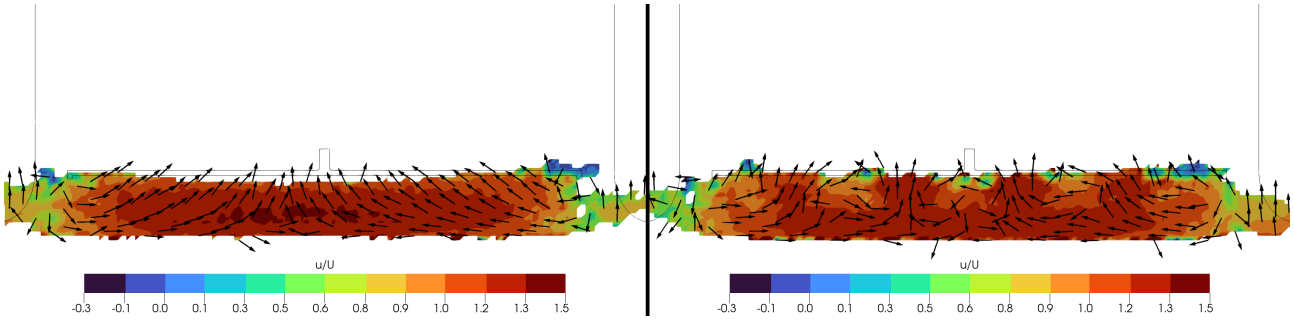

(a) Diffuser leading edge, $x/L_B = 0.75$,

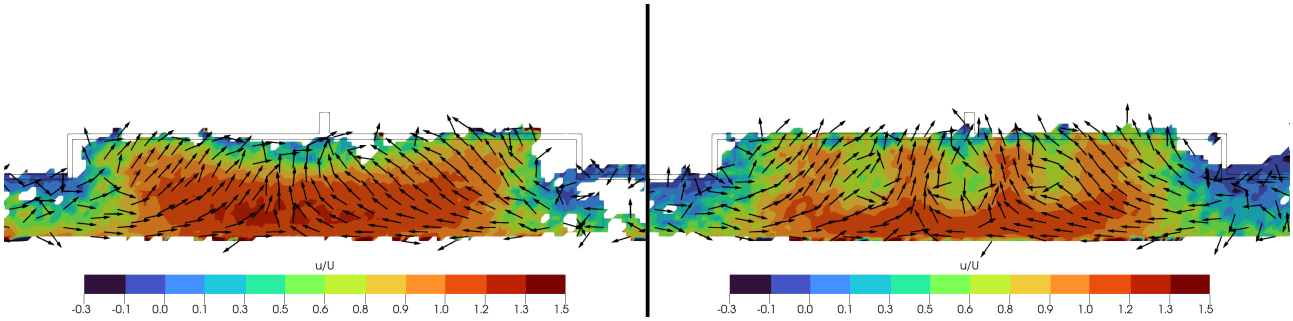

(b) $1/3^{rd}$ of diffuser length, $x/L_B = 0.833$

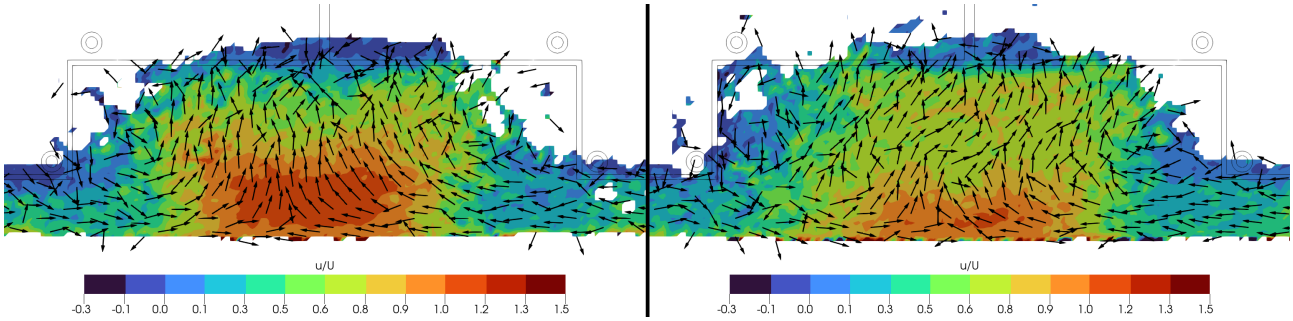

(c) Diffuser trailing edge, $x/L_B = 1.0$

Figure 7.11: Streamwise velocity contours and velocity vectors at different x locations, for diffuser with (right side) and diffuser without (left side) vortex generators

Starting at the diffuser leading edge, here the streamwise velocity is highest for both diffusers. There is upwash, and more importantly, inwash (i.e. flow moving laterally towards the center of the diffuser) in both the VG and non-VG model. Moving downstream through the diffuser, the upwash component remains, with the highest streamwise velocities persisting near the center of the diffuser. The high velocity air that exits the diffuser at around freestream velocity spans roughly half of the diffuser width in both VG and the non-VG model. Both geometries show air entering from the outboard sides of the diffuser, suggesting that there is a pressure gradient flowing laterally towards the diffuser centerline. This lateral inflow is often identified as the main driver of the streamwise vortex pair originating from the diffuser sidewalls. The presence of these vortices is not captured well in this experiment, as there is not enough data in the upper corners of the diffuser.

There are however some noticeable difference between the 2 cases. Already at the start of the diffuser, in figure 7.11a, 4 distinct regions of around 1.4 times U_∞ separated by sections of lower streamwise velocity can be seen near the diffuser surface. The velocity vectors are also much more uniform in their direction in the diffuser without vortex generators. A rotation pattern in the velocity vectors can be seen around the pockets of low velocity in the VG results, even more noticeable further downstream in the diffuser, in figure 7.11b. Here the regions of higher velocity separated by lower velocity are clearly visible. These suggest that streamwise vortices, generated by the vortex generators just ahead of the diffuser leading edge, are present and propagate

some streamwise distance into the diffuser. Figure 7.12 shows a closeup of the diffuser plane at $x/L_B = 0.75$, colored by the streamwise vorticity ω_x component. Blue means a counter-clockwise rotation, where a yellow color indicates a clockwise rotation when looking in the streamwise direction. A distinct pattern of alternating rotation direction is visible in the vorticity contours, matching with the location and orientation of the vortex generators placed ahead of the diffuser leading edge.

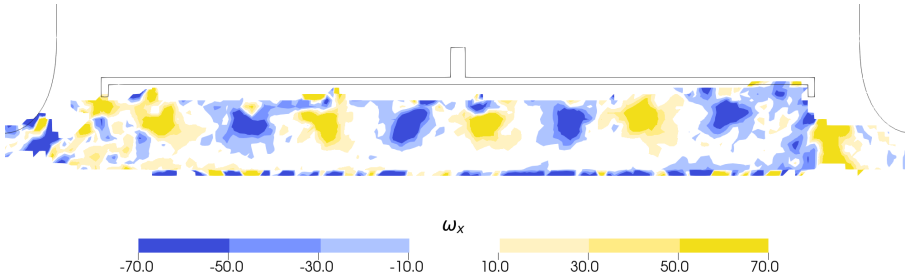

Figure 7.12: Contour plot of streamwise vorticity ω_x $[s^{-1}]$ at $x/L_B = 0.75$ for the diffuser equipped with vortex generators

At the diffuser exit, the distinct low and high velocity regions are no longer visible for the car with vortex generators. It does show however the region of higher streamwise velocity sitting close to the diffuser surface, compared to the diffuser without VG's. This is the same effect already described in the car centerline contour plots of section 7.1.4. The velocity gradients through the height of the diffuser are much smaller for the diffuser with vortex generators, compared to the diffuser without.

To further illustrate the effect of the vortex generators, figure 7.13 shows the difference in normalized streamwise velocity at the car centerline. It is colored by $\Delta u/U_\infty$, which is calculated by subtracting the $u/U_{\infty NoVG}$ from $u/U_{\infty VG}$.

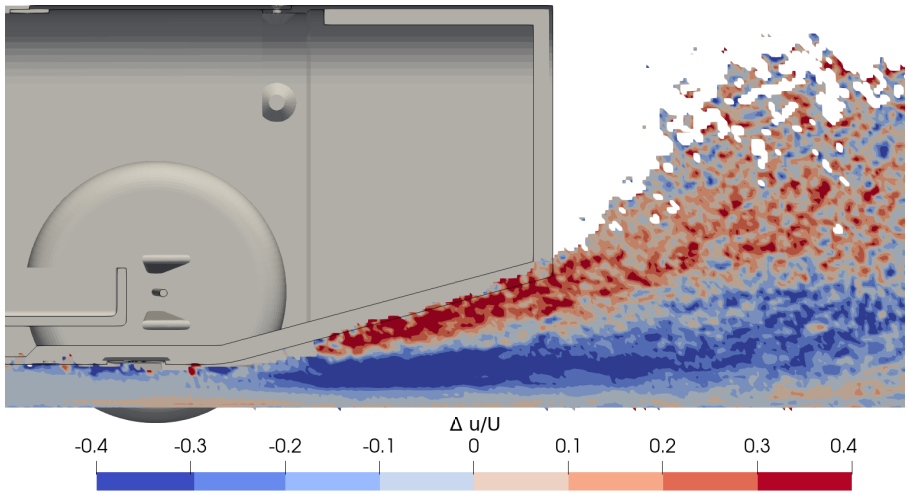

Figure 7.13: Difference in streamwise velocity distribution due to vortex generators, computed as $((u_{VG} - u_{NoVG})/U_\infty$

Figure 7.13 clearly shows that the vortex generators are producing streamwise vortex pairs, which move some of the high velocity flow low to the ground, closer to the diffuser surface. In turn, the flow close to the ground loses some of its streamwise velocity magnitude, leading to the change in velocity field distribution between the left and right of figure 7.11c.

As a final indication of the presence of streamwise vortices, the so called Q criterion is calculated using the binned VG velocity dataset. The Q criterion is sometimes also referred to as the second invariant of $\nabla \mathbf{u}$, and defined as in equation 7.1 below (Jeong et. al 1995) [39].

$$Q = \frac{1}{2}\left(||\mathbf{\Omega}||^2 - ||\mathbf{S}||^2\right) \tag{7.1}$$

Q can be used to identify vortices, based on the local balance of the shear strain rate and vorticity magnitude [39]. A positive value of Q indicates a flow where vorticity dominates over the strain rate or viscous stresses. These regions of flow are typically associated with vortex structures, hence visualizing positive Q criterion iso-surfaces are useful in identifying vortices [39]. Using the Paraview program, the Q criterion can be directly computed for a 3 dimensional velocity field, and plotted as iso-surfaces for different values of Q. Figure 7.14 below plots $Q = 0.006\ s^{-2}$ iso-surfaces in the diffuser region, for the car model equipped with a VG strip, with its fins highlighted in red.

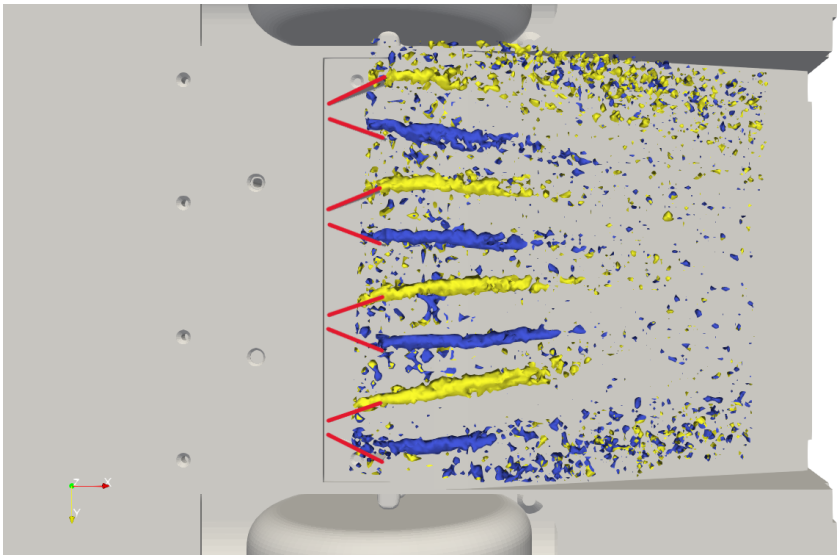

Figure 7.14: Iso-surface of $Q = 0.006\ s^{-2}$ for car equipped with vortex generator strip, colored by streamwise rotation (blue = counter clockwise, yellow = clockwise)

All eight fins of the vortex generator strip create a vortex, which propagate into the diffuser. These vortices create the up and downwash pattern discussed above, and change the distribution of high streamwise velocity throughout the diffuser height, compared to the diffuser with no vortex generator strip. As the diffuser without vortex generators did not show clear signs of separation, it is not possible to judge the effectiveness of adding the VG strip to prevent or reduce separation. It appears that the streamwise vortices introduced are mostly transporting some high momentum flow from the lower part of the domain closer to the diffuser surface, as well as convert some of the streamwise velocity into a rotational velocity component. There is no significant difference in the magnitude of the velocity peak generated at the diffuser leading edge, and in flowfield further upstream.

7.2 Pressure distribution

In order to assess the performance of a diffuser, it is important to evaluate the pressure distribution around the model. Section 6.5 discusses the method used to calculate the pressure coefficient C_P, defined by equation 2.1, using the local velocity gradients from the binned data sets.

It is important to note that the pressure evaluation will only be applied in the center region of the car. This is due to the fact that the assumptions made to use the method from section 6.5, such as applying Bernoulli's principle for the initial C_P value at ground level, and assuming a steady and inviscid flow. These assumptions cannot be applied in the outboard regions of the car i.e. where flow is exiting the floor laterally between the wheels and flow is flowing in from the sides at the diffuser outer edges. Here it is no longer possible to follow a streamline from the front of the car into the diffuser, as illustrated in figure 7.2. Marklund and Marklund [12], Cooper [4] and others typically evaluate the pressure coefficient of bluff bodies on the car centerline as well, where flow is most steady and 3D effects aren't as apparent in the pressure distribution. These result in the figures 2.4 and 2.5 presented in chapter 2 earlier.

The results of this pressure evaluation method are presented in figure 7.15 below for all three tested geometries.

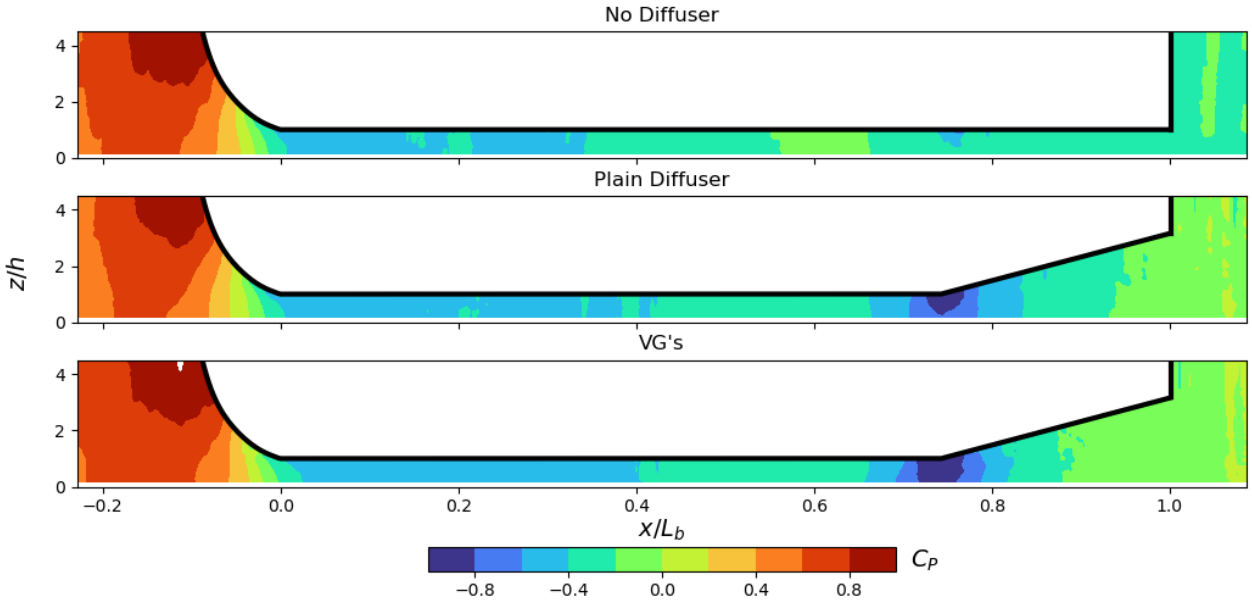

Figure 7.15: Contour plot of C_P around tested car geometries at $y/L_B = 0$

As with the velocity fields along the car centerline, there is no significant difference between the car with and without diffuser fitted, for the forward half of the car. At the stagnation point, $C_P = 1.0$, and as the flow is accelerated under the front of the car, C_P drops to about -0.5 for all three configurations. A very slight pressure increase is visible along the floor length in streamwise direction, until the rear axle and start of the diffuser. This slight pressure increase, linked to a similar small velocity decrease, can be contributed to some lateral outflow happening along the car center portion. Between the front and rear wheels, flow expands laterally, as is shown in the streamlines of figure 7.2 earlier. A (lateral) expansion will lead to a decrease in flow velocity (as per Bernoulli's principle), and a subsequent pressure rise.

The no diffuser equipped model keeps increasing in C_P, until a slight pressure drop around $x/L_B = 0.7$, where there is a small decrease in C_P. The drop in pressure is much smaller in magnitude however compared to the pressure drops at the diffuser leading edges of both the plain diffuser and one with VG's fitted. Both diffuser geometries shows a clear C_P minimum at the diffuser leading edge, in the order of $C_P = -0.9$. The car model with diffuser and vortex generators 'peaks' at the lowest C_P, but shows a slightly faster recovery to towards the base pressure through the diffuser length compared to the no VG diffuser geometry.

Inside the diffuser, C_P gradually recovers towards a diffuser exit C_P of about -0.1, the base pressure behind the car model, which is quite close to the freestream pressure, i.e. $C_P = 0$. The car without diffuser fitted retains a C_P of around -0.3, even behind the car model. It shows a base pressure which is lower than the base pressures of the diffuser equipped models.

Contrary to the velocity contour plots of the car centerline, there is not much difference in the pressure

distribution inside the diffuser between the model equipped with and without VG's. The clear difference in streamwise velocity distribution throughout the diffuser height, illustrated in figure 7.13, is not visible in the C_P distribution inside the diffuser section of the cars.

Figure 7.16 below is created, plotting the C_P value at a fixed distance $z/h = 0.46$ beneath the car surface. This is the same height below the model as used for the plotting of the normalized streamwise velocity, presented in figure 7.5.

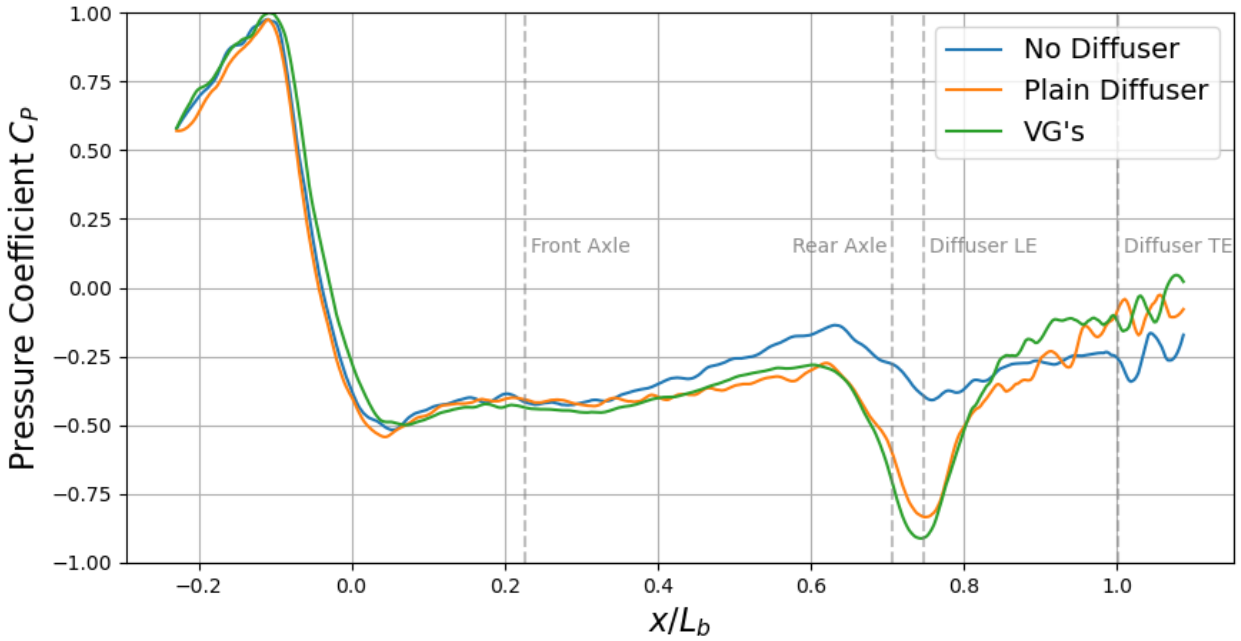

Figure 7.16: C_P distribution along car centerline at z/h = 0.46 below the car surface

Figure 7.16 shows the same trends observed from the contour plots of figure 7.15, in terms of differences between the 3 tested geometries. The pressure recovery and slight drop near $x/L_B = 0.7$ seen for the flat floor, no diffuser model, can be caused by the presence of the rear wheels. These still impose a slight lateral blockage factor for the flow along the car centerline, which could explain the pressure increase and subsequent drop around the rear tires of the model.

The local pressure coefficient around the model for the three tested geometries at different points of interest are summarized in table 7.2 below.

Table 7.2: C_P values at different points around the tested car geometries

	Floor LE	**Diffuser LE**	**Car TE**
No Diffuser	-0.5	-0.4	-0.3
Plain Diffuser	-0.5	-0.85	-0.1
VG's	-0.5	-0.9	-0.1

Apart from this, the C_P profiles of both the diffuser equipped and no diffuser (or 0° angle) models show good agreement with the trends reported in literature, for example by Cooper [4] and Marklund and Marklund [12]. These are repeated in figures 7.17 and 7.18 below. Adding a diffuser to the bluff body or car model does not change the pressure field at the forward half of the body, and only near the diffuser leading edge the benefit of adding a diffuser is visible in terms of lowering the local C_P. The pressure decrease due to the diffuser is caused by the 3 dimensional flow effects, where flow is entering the sides of the diffuser laterally. This lateral inflow, combined with the diffuser pumping effect described by Sovran [3], make the flow accelerate at the diffuser inlet, and lowering local static pressure of the flow.

The C_P plots from this experiment do not show as much of a pressure recovery after the initial floor leading edge peak, compared to figures 7.17 and 7.18. A possible cause could be that the flow along the car centerline is more 'shielded' from lateral outflow effects due to the wake of the front tires, together with the diffuser width being only half of the total body width in this experiment, compared to a full width diffuser tested by Cooper and Marklund.

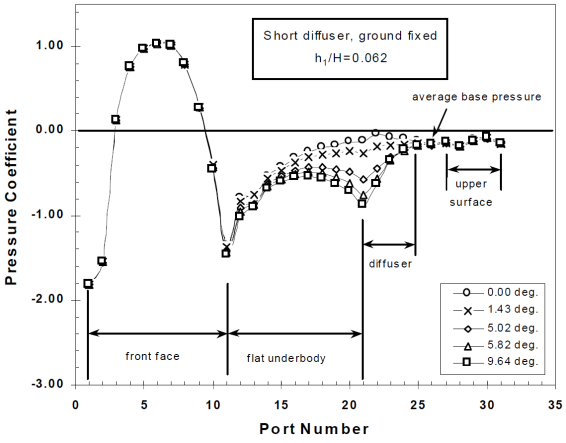

Figure 7.17: The effect of increasing diffuser angle on C_P around a bluff body [4]

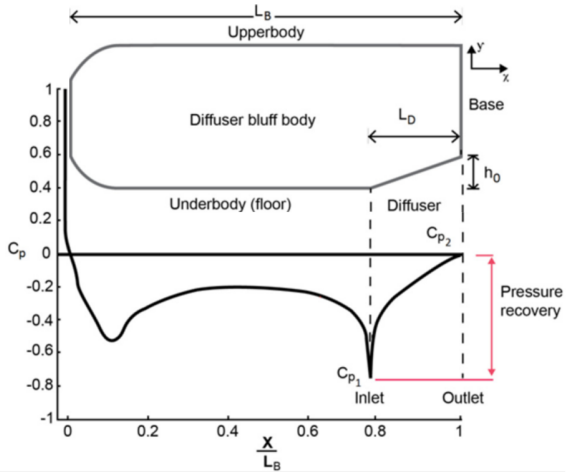

Figure 7.18: Typical pressure distribution on diffuser equipped bluff body [12]

As done with the velocity profiles in section 7.1.5 earlier, figure 7.19 shows a streamwise profile of the C_P distribution under the car, at different spanwise locations. All three locations show a very similar profile compared to the centerline profile shown in figure 7.16, until some 10% of the diffuser length. The low pressure peak at the diffuser inlet shows a consistently lower pressure for the VG cases. This can be due to the fact that the VG's are resolving a small separation region in the plain diffuser, near the diffuser inlet, and hence allowing for a slightly lower pressure at the diffuser inlet. Another explanation could be that the blockage effect (a smaller area for flow to pass through) of the VG fins introduces an increase in local suction. This seems unlikely however, as it would also imply (through Bernoulli's principle) an increase of velocity near the VG fins, which is not clearly observed in the velocity profiles.

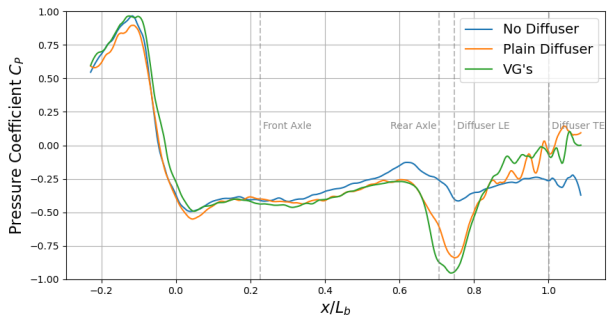

(a) $y = 14$ mm

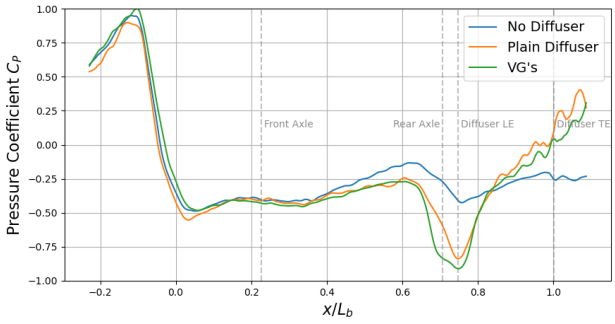

(b) $y = 24.5$ mm

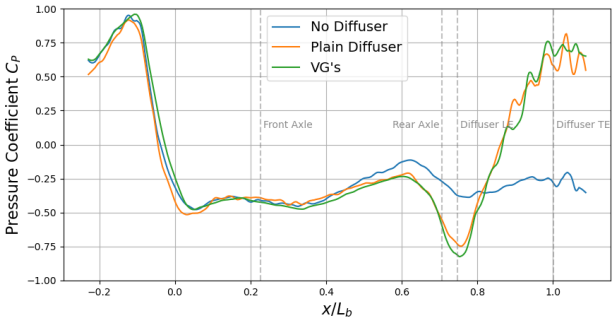

(c) $y = 49$ mm

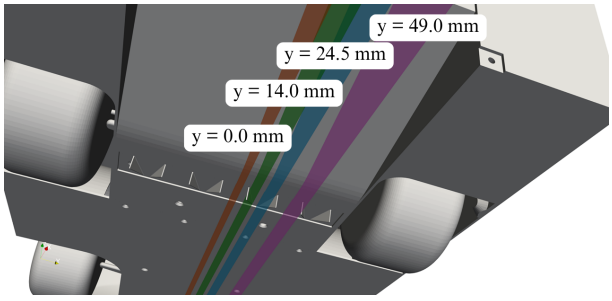

(d) Lateral positions of velocity plots with respect to car model

Figure 7.19: C_P distribution along car centerline at $z/h = 0.5$ below the car surface for different lateral positions

When looking at the pressure distribution inside the diffuser, the further outboard profiles show a much more prominent recovery of pressure coefficient than observed at the car centerline. For example, looking at figure 7.19c, C_P from the diffuser inlet minimum of roughly $C_P = -0.8$ to a value of around $C_P = 0.75$ at the diffuser trailing edge ($x/L_B = 1.0$). This means that the flow has decelerated to below freestream velocity,

something that is also confirmed by figure 7.20. There is a clear region of high velocity flow inside the diffuser, with streamlines contracting toward the car centerline (previously shown in figure 7.2).

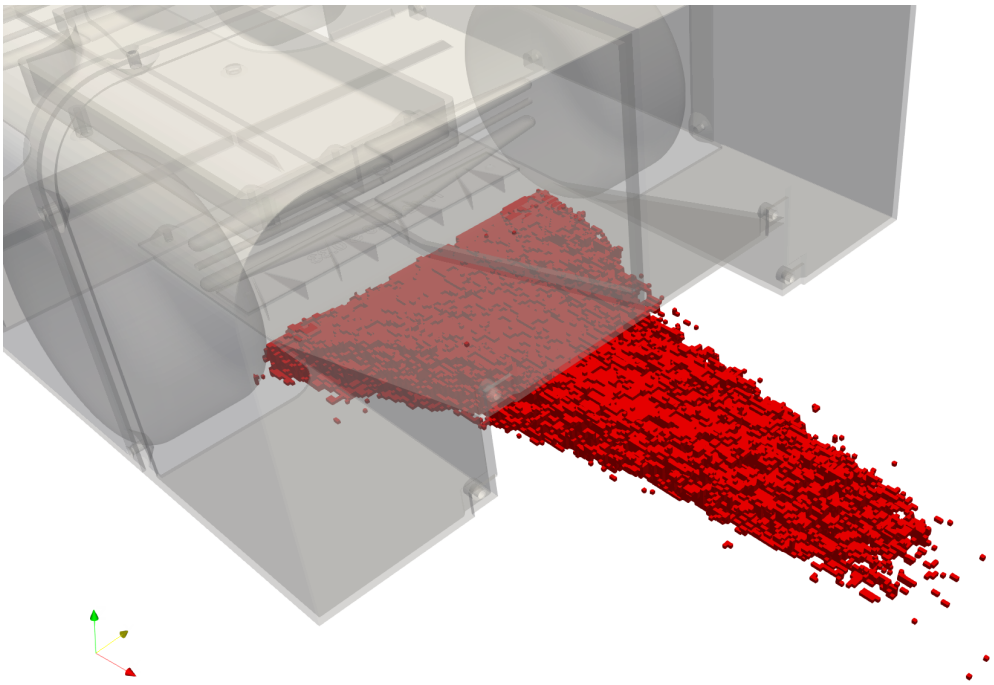

Figure 7.20: Bin cells inside the diffuser where the $u_{tot}/U > 0.95$

Outboard of this center region of high velocity, and corresponding low C_P, i.e. at $y = 49$ mm figure 7.19c, the pressure coefficient is much higher for both diffuser models, compared to the no diffuser case. This potentially negates the extra downforce generated by having a lower static pressure along the car centerline region. With the data available, and the method used to compute the pressure coefficient, it is not possible to compute an accurate downforce figure based on just this pressure data. That would require an integration of the surface pressure along the entire car body, something that is not possible with the velocity data captured in this experiment.

7.3 Data uncertainty and convergence

After analyzing the results and drawing conclusions from the data of this experiment, it is important to assess the uncertainty of the collected data using this setup. As the velocity field is the primary output of this experiment—and most other parameters, such as pressure and vorticity are derived from it, an analysis of the velocity uncertainty is performed first. Then some insight on the uncertainty related to the pressure evaluation method presented in section 6.5 is covered, after which a convergence study is presented to show the effect of the number of runs used per geometry.

7.3.1 Velocity uncertainty quantification

The binned velocity field dataset is generated by fitting a polynomial to the collected data points within each bin and sampling this polynomial at the bin center. This process provides an approximation of the mean value of the data points in that bin. Together with the mean value, a standard deviation within a bin is calculated. With this standard deviation, the standard random uncertainty of the mean $\epsilon_{\bar{u}}$ can be estimated as:

$$\epsilon_{\bar{u}} = \frac{\sigma_u}{\sqrt{N}} \tag{7.2}$$

Here σ_u is the standard deviation of the velocity in each bin, based on all the particle tracks that are sampled to generate the value for the binned dataset in that location. N is the number of independent samples used to arrive at the binned velocity value. Even-though each bin value is constructed using all n particle track data points in the given bin, $n \neq N$ for the uncertainty quantification used in this experiment. This is due to the fact that particle tracks from a single run are not fully independent from one another. Each run the car might have had a slightly different attitude/orientation when traveling through the measurement domain, as well as external effects which can alter the velocity field at a certain point around the model. To combat this potential dependence between particle tracks, N is taken as the number of runs per geometry. In most of the domain, $n >> N$, and the true value of N independent measurements will be somewhere between the number of runs and the total number of particle tracks per bin. However taking N to be equal to the number of runs is a conservative approximation, and used for the rest of this uncertainty analysis.

The standard deviation is directly computed and output with the binning data, hence equation 7.2 is applied throughout the whole domain. Figure 7.21 shows the confidence interval $\epsilon_{\bar{u}}$ applied around the mean normalized velocity magnitude value along the car centerline, at the same height from the surface as presented in figure 7.5.

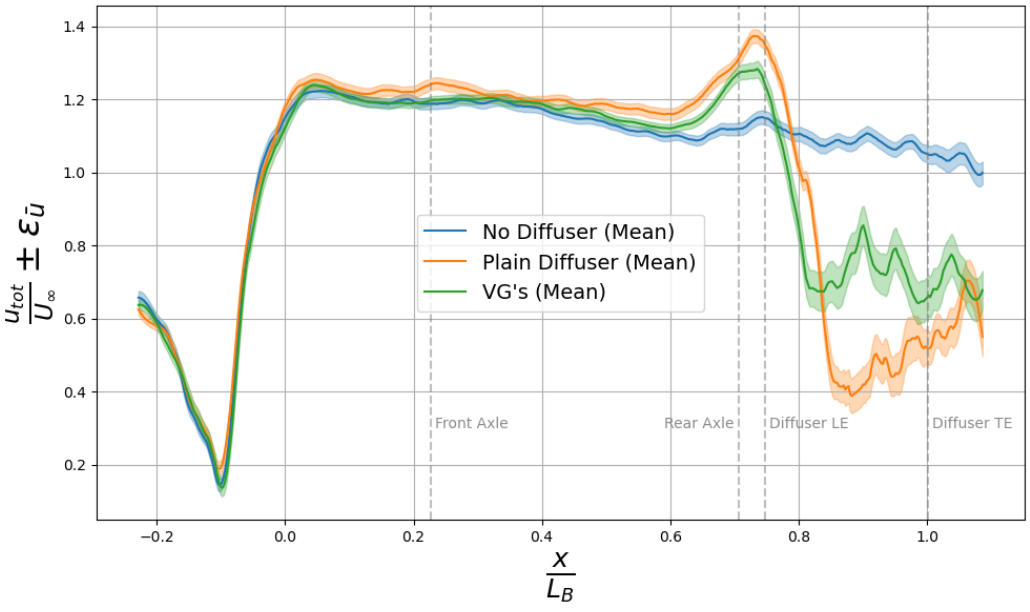

Figure 7.21: Normalized velocity magnitude profile including $\epsilon_{\bar{u}}$ confidence interval along car centerline

All three models show a similar level of uncertainty until the start of the diffuser. The relative uncertainty is of the order of 1.5% U_∞. Clearly, the uncertainty is highest in the diffuser area of the model. Both the plain

diffuser and the diffuser with VG's show an increase in $\epsilon_{\bar{u}}$, compared to the no diffuser, flat floor model. Both are similar in magnitude, peaking at around 6.0% U_∞ relative uncertainty.

This rise in relative uncertainty is driven by an increase in the local velocity standard deviation σ_u. While the flow underneath the flat floor of the car is very uniform, and almost purely in streamwise direction, there is very little fluctuation in the velocities measured. Inside the diffuser however, the flow becomes much more 3D dimensional, with lateral inflow, (potential) small regions of flow separation, streamwise vortices, etc. These factors make it such that the fluctuations in the velocity of particles tracked between runs will be larger in this area, increasing the standard deviation of the velocity in the bins located inside the diffuser.

The relative uncertainty is lower than the difference in peak velocity between the diffuser equipped models and no diffuser equipped geometry, as this difference is in the order of a 25% increase in local velocity magnitude. This shows that the current setup is capable of capturing the large scale flow effect of adding a diffuser to a flat floor car model. However, looking at the difference between the vortex generator equipped diffuser model and the plain diffuser without VG's, there is less of a clear distinction between velocity peaks at the diffuser leading edge, and the differences are close to the order of the uncertainty of the velocity. This means that when one is drawing conclusions from the differences between the velocity fields of the VG and Non-VG diffuser models, one should take the uncertainty into account. The observed difference might not be statistically significant, if they fall within the uncertainty of the results.

The distinction between the higher momentum flow being transferred to the diffuser surface by the introduction of the vortex generators does still hold, even with the relative uncertainty reaching about 6% of the mean velocity.

7.3.2 C_P uncertainty quantification

The accuracy of the pressure integration method described in section 6.5 is dependent on several factors. The assumptions made in deriving the pressure gradient $\frac{\partial p}{\partial z}$, the initial starting value of C_P, the local velocity gradients and the numerical integration scheme used all contribute to the accuracy of the method. In order to give an indication of the uncertainty of the C_P calculated, the following method is introduced.

The flow upstream of the car can be considered to be very close to perfectly steady, incompressible, inviscid and irrotational. Hence, Bernoulli's principle and the corresponding value of C_P based on equation 6.4 is a very reliable way to compute a reference $C_{P_{ref}}$ value. By computing this $C_{P_{ref}}$ value at the top of the domain, i.e. $z/h = 4.5$ ahead of the car in figure 7.15, one can compare this $C_{P_{ref}}$ value to the C_P value computed with the integration method described in section 6.5. This will give an indication of the total error introduced by the integration method, when applied over the full $z/h = 4.5$ domain height, which can be used as a first estimate of the relative uncertainty on the C_P values computed.

Computing the $C_{P_{ref}}$ value at a $z/h = 4.5$ height for $-0.2 < x/L_B < -0.15$, and comparing the value to the computed C_P using the integration method, an average absolute uncertainty to the local C_P of 0.04 is found, for the probed x/L_B range.

Figure 7.22 shows an example of the C_P value computed at different heights in the domain, when using Bernoulli, or the pressure gradient integration method, at $x/L_B = -0.17$. Figure 7.23 shows the relative difference between the two methods, calculated as $||C_{P_{integration}} - C_{P_{Bernoulli}}||$

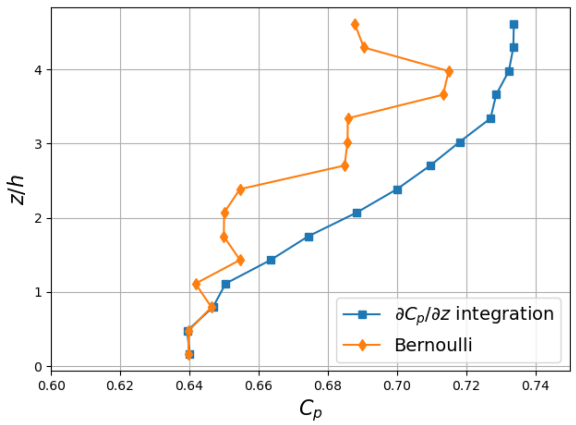

Figure 7.22: Computed C_P vs z/h by using Bernoulli or a pressure gradient integration method, at $x/L_B = -0.17$

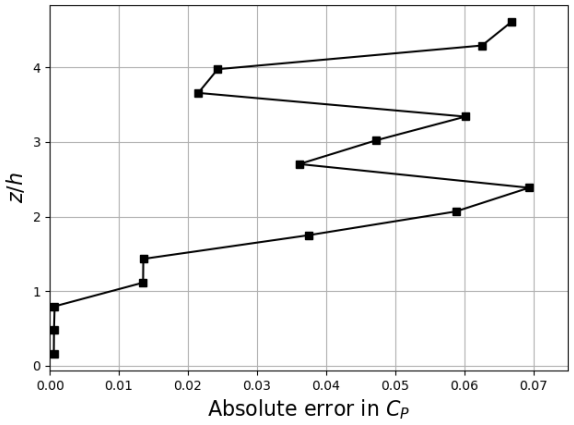

Figure 7.23: Absolute error vs z/h between C_P computed using the pressure gradient integration method and a Bernoulli based C_P, at $x/L_B = -0.17$

A constant error of 0.04 C_P is taken as a first order estimate on the uncertainty of the integration method. It does however not include the uncertainty introduced to the starting value of C_P at $z/h = 0$, which is computed based on Bernoulli's principle and the local velocity magnitude. Using the law of uncertainty propagation, the uncertainty of the starting C_P value can be computed based on the standard uncertainty of the mean velocity $\epsilon_{\bar{u}}$, as shown in equation 7.3.

$$\sigma^2_{C_{P_{Bernoulli}}} = \left(\frac{\partial C_P}{\partial \frac{u}{U_\infty}}\right)^2 \epsilon^2_{\bar{u}} \tag{7.3}$$

Using the definition of C_P from equation 6.4, one gets equation 7.4 below:

$$\sigma_{C_{P_{Bernoulli}}} = 2||\frac{u}{U_\infty}||\epsilon_{\bar{u}} \tag{7.4}$$

Combining $\sigma_{C_{P_{Bernoulli}}}$ with the constant absolute C_P error of 0.04 computed from the C_P integration method, a σ_{C_P} is computed, defined below:

$$\sigma^2_{C_P} = 0.04^2 + \left(\sigma_{C_{P_{Bernoulli}}}\right)^2 \tag{7.5}$$

Figure 7.24 shows the same C_P distribution as presented earlier in figure 7.16, but with σ_{C_P} applied as confidence interval around the computed value.

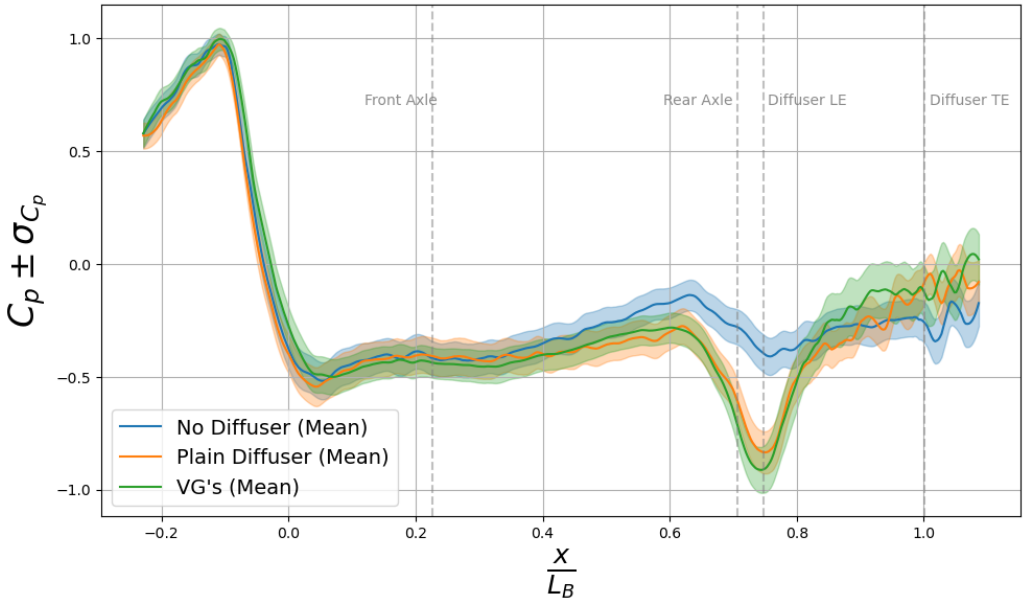

Figure 7.24: C_P distribution along car centerline at $z/h = 0.46$ below the car surface with confidence interval σ_{C_P}

The difference in C_P underneath the car with and without VG applied falls within the confidence interval for almost the entire length of the of the car. Hence the potential difference between the two geometries is too small to be considered statistically significant.

However, the C_P plot of the car without a diffuser has a larger difference to the diffuser geometries than the confidence interval, near the rear axle and diffuser leading edge, $0.55 < x/L_B < 0.8$. Here its value is considerably higher than the C_P of the two diffuser equipped cars, meaning that there is a significant pressure drop achieved compared to the no diffuser case. σ_{C_P} is highest in the diffuser area and the wake behind the car, driven by the increased velocity uncertainty in that region. This makes it difficult to claim any significant differences in C_P between the three tested geometries in this region of the car.

7.3.3 Data convergence

To assess how the measured velocity field converges toward the mean flow around the car model as more runs are added, the following procedure is applied. The particle track velocity data is binned, combining particle tracks from multiple runs into a single dataset for each geometry, as described in section 6.4. By evaluating the mean velocity at a specific bin, using only a subset of all available particle tracks in that bin, the effect of increasing the number of runs on convergence can be quantified.

Three different points around the car model are chosen, one located close to the nose/floor leading edge, one point underneath the cars flat floor section, and one inside the diffuser. The location of these points are plotted in figure 7.25 below:

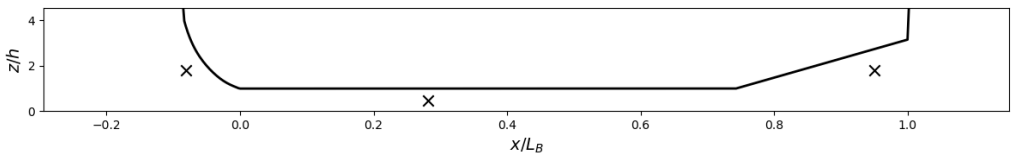

Figure 7.25: Sample points for convergence study

For each Point of Interest (POI), referred to as *Nose*, *Floor*, and *Diffuser*, the total number of tracked particles contributing to the corresponding bin (radius = 7 mm) is counted for each binned dataset. Since the *Diffuser* POI is located above $z/h = 1$, no particle data is available for this point in the flat-floor, no-diffuser configuration.

The average number of particles per run tracked in a specific bin, Np_{avg}, is determined by dividing the total number of particles in each bin by the number of runs performed for that geometry:

$$Np_{\text{avg}} = \frac{Np_{\text{total}}}{r_{\text{max}}} \tag{7.6}$$

where Np_{total} is the total number of particles recorded at the POI, and r_{max} is the total number of runs performed (30 for both of the diffuser cases, 20 for the flat floor model).

To analyze convergence, the mean velocity is computed using 10,000 unique samples of size $Np_{\text{avg}} \times r$ at each POI, where r represents the number of runs for which to evaluate convergence. The standard deviation of these 10,000 mean velocities, σ_{mean}, is then normalized by the free-stream velocity U_∞:

$$C_r = \frac{\sigma_{mean}}{U_\infty} \tag{7.7}$$

where C_r represents the relative convergence of the mean velocity. This calculation is repeated for all $1 < r < r_{\text{max}} - 1$. Plotting C_r as a function of r for each POI and all three geometries produces figure 7.26.

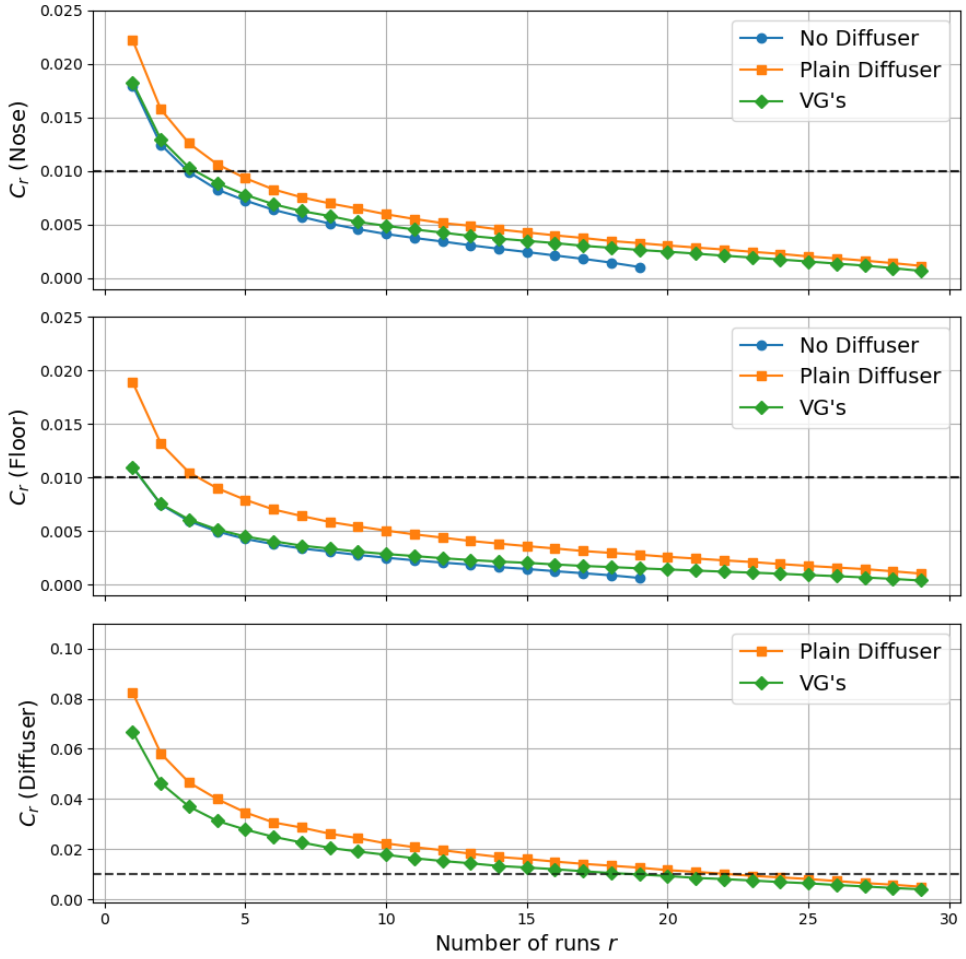

Figure 7.26: Relative convergence of the mean velocity at different numbers or runs, at different points around the car

A dashed black line is included at $C_r = 0.01$, corresponding to a standard deviation of the mean velocity within 1% of U_∞. The *Nose* and *Floor* POIs exhibit rapid convergence, reaching $C_r < 0.01$ within 4–5 runs. For the diffuser POI however, at least 23 runs are needed for a relative convergence below 1%. This is most likely due to 2 factors, one being that the velocity fluctuations are larger inside the diffuser compared to the flow at the car nose and underneath the flat floor section. Secondly, there are less particles tracked in the diffuser bin volumes per run. This decrease in number of tracked particles per volume can be caused by the potential presence of flow separation in the diffuser, as well as behind the model. Combined with the finite length of track that is seeded with HFSB (as only the tent is filled), this could be a potential explanation for the reduced number of particle tracks inside the diffuser and behind the car. With the smaller number of particles available to be tracked, combined with the greater velocity fluctuations in the diffuser, the number of runs needed to reach convergence to the mean flow hence needs to be in the order of 25 or more.

8. Conclusions and Recommendations

This chapter presents the key findings of the thesis, evaluates the improvements made to the experimental setup, and discusses the aerodynamic performance of the tested diffuser configurations. The chapter is structured as follows:

After this, a set of recommendations is given for future work, primarily focusing on the application and improvement of the Ring of Fire system for use in large-scale automotive diffuser aerodynamics

8.1 Conclusions

Aerodynamics play a critical role in the performance optimization of race cars, particularly in motorsports where downforce generation is key to maximizing cornering speeds while maintaining an efficient balance between downforce and drag. As discussed in chapter 2, underbody aerodynamics, and in particular the use of diffusers, contribute substantially to downforce generation with a relatively low drag penalty compared to external aerodynamic devices such as wings [2]. The ability to effectively manipulate the flow underneath a race car allows for improved traction, enhanced vehicle stability, and ultimately, better lap times [1]. This makes the study of diffuser aerodynamics essential in the broader field of automotive aerodynamics.

Below, the research objective and questions are stated again, as they are presented in chapter 4. The following sections will try to answer the questions based on the results from the experiment.

8.1.1 Research Objective and Questions

The objective of the experiment for this thesis project had the following 3 main components.

- Improve LPT capabilities by increasing the number of cameras used, reduce reflections, Lexan sheet vibrations, etc.
- Create better seeding distribution around the model, mainly focusing on seeding density and larger seeding containment for the car to travel through.
- Improve diffuser performance of the model by redesigning bodywork, floor and diffuser integration on the RC car.

Based on the research gap and objectives, the following research questions were formulated:
How do geometric modifications influence flow separation and downforce generation in automotive diffusers?

1. How does a rounded diffuser leading edge change the performance of a 15° diffuser compared to a sharp leading edge, in terms of peak velocity, pressure distribution and downforce generated?
2. How effectively can vortex generators delay or reduce separation inside a diffuser?
3. What is the effect of streamwise vortices within the diffuser in terms of peak velocity, pressure distribution and downforce generated?

How accurately can the Ring of Fire system measure critical aerodynamic characteristics of race car diffusers?

1. What spatial resolution/bin size can be achieved with the new setup?
2. How many runs are needed to reach a mean flow velocity convergence within 1% of to the car's velocity?
3. How accurate is the RoF setup in quantifying velocity and pressure distributions, as well as downforce figures for automotive applications?

8.1.2 Improvements of the experimental setup

Starting off with the main objectives of this research, being the improved LPT capabilities, seeding and model aerodynamics, the results show the following, compared to the setup used by Battegazzore:

By increasing the number of cameras used from two to three, as well as fitting 2 high power LED units inside the concrete shell, a measurement domain of roughly 400 x 200 x 200 mm was achieved. The car model traveled through a 9 x 3 x 4 m (LxWxH) enclosed tent completely filled with neutrally buoyant Helium Filled Soap Bubbles (HFSB), generated by a 200 nozzle seeding rig developed at the Delft University of Technology. This ensured a better distribution of particles around the car model, especially in the diffuser and wake of the car.

A custom 3D printed bodywork ensured the flow inside of the diffuser to be protected from the low pressure wake originating from the rear tires of the RC car, which caused lateral outflow in the diffusers tested in the experiment of Battegazzore [9]. This is against the typical inflow direction observed inside diffuser equipped bluff bodies in literature, for example by Senior et al. [18]. Instead, from the results of this experiment it is clear that there is lateral inflow observed into the diffuser.

With the objectives achieved, the first research question about the developed RoF setup can be answered, with the question being: ***What spatial resolution/bin size can be achieved with the new setup?***

The data generated from the 30 runs per diffuser geometry, and 20 for the flat floor no diffuser car model was sufficient to create a binned velocity dataset with spatial resolution of 7 mm. A minimum of 10 particles are present per bin, with a large majority of the domain having over 100 particles per bin, ensuring the ability to fit a 2nd order polynomial to the velocity data of the particles in each bin. Compared to the experiment of Battegazzore, this is over 2 times increase in spatial resolution, from 15mm to 7mm. The three camera setup also allowed for a wider measurement domain, making it easy to capture the full width of the diffuser in a single run.

8.1.3 Aerodynamic performance of the tested geometries

The velocity field analysis provided insights into the acceleration and recovery of the flow beneath the car. Compared to the observations from Battegazzore, the streamlines under the car equipped with a diffuser show inwash in the diffuser area, opposed to the outwash due to the exposed rear tires. Looking at the streamwise velocity around the center of the car with a flat floor, velocity peaks at about $u/U_\infty = 1.25$, after which is gradually declines to about 1.05 times U_∞ at the car trailing edge.

The results showed two primary acceleration peaks for the diffuser equipped cars: one at the transition from the curved nose to the flat floor, where the velocity reached approximately 1.25 times U_∞, and another at the diffuser leading edge, where the peak velocity was around 1.4 times U_∞. Close to the car surface, the velocity magnitude is higher for the diffuser without vortex generators at the diffuser leading edge.

A small separation bubble might be present just after the diffuser start, where there is no data captured for the plain diffuser geometry. This can be an indication of a small separation bubble formed at the diffuser inlet. There is however no indication of the large scale separation observed by Battegazzore for diffusers at angles 15° and 20°. The addition of the rounded diffuser leading edge, combined with the lateral inwash can be factors in the improved flow attachment.

When a strip of vortex generators is added to the car, streamwise vortices are introduced in the diffuser. The vortices move higher momentum air closer to the diffuser surface, leading to a higher velocity magnitude recorded close to the diffuser surface, when compared with the plain diffuser without VG's. The small region of no particle data just after the diffuser leading edge is also not present anymore, suggesting that the vortices might reduce the potential separation bubble observed for the plain diffuser. No clear effect on the upstream velocity distribution was noticed, suggesting that while vortex generators influence and introduce secondary flow structures, their overall effect on primary velocity fluctuations under the car is limited.

The pressure distribution analysis provided further insight into diffuser performance by computing the pressure coefficient C_P along the car centerline. The method relied on integrating velocity gradients from the binned velocity field, with an initial reference pressure calculated using Bernoulli's principle. The results showed that, in the forward half of the model, the pressure distribution remained largely unchanged across all configurations. However, significant differences emerged at the diffuser leading edge, where the presence of a diffuser resulted in a pronounced pressure drop, with minimum C_P values reaching approximately $C_P = -0.9$.

Inside the diffuser, a gradual recovery of C_P was observed, aligning with the C_P profiles from literature. The model equipped with vortex generators exhibited slightly faster pressure recovery compared to the plain diffuser, indicating an altered flow structure but no dramatic improvement in base pressure. Also, the distinction in a higher velocity close to the surface of the diffuser with VG's has no clear effect on the pressure distribution on a vertical profile through the diffuser height.

Notably, the car without a diffuser retained a lower C_P value at the rear, suggesting that the diffuser-equipped configurations achieved better pressure recovery towards freestream conditions. The full centerline C_P profiles align well with the pressure profiles presented by Cooper et al. and other sources in literature [4], in terms of the effect of adding a diffuser to a model. The pressure recovery between the floor leading edge and the diffuser leading edge, observed by Cooper, is not as pronounced in the centerline C_P from this experiment. This is likely caused by a reduced lateral outflow between the front and rear axle, hence the centerline flow is less affected by 3D flow effects.

Below, table 8.1 shows the distribution of the maximum velocity magnitudes at different x locations around the car, for the three different geometries, while table 8.2 shows the value of the pressure coefficient C_P at those locations.

Table 8.1: Normalized velocity magnitude u_{tot}/U_∞ at different points around the tested car geometries

	Floor LE	**Diffuser LE**	**Car TE**
No Diffuser	1.22	1.15	1.05
Plain Diffuser	1.24	1.38	0.52
VG's	1.25	1.30	0.66

Table 8.2: C_P values at different points around the tested car geometries

	Floor LE	**Diffuser LE**	**Car TE**
No Diffuser	-0.5	-0.4	-0.3
Plain Diffuser	-0.5	-0.85	-0.1
VG's	-0.5	-0.9	-0.1

Looking back at the automotive aerodynamics research questions:

- ***How does a rounded diffuser leading edge change the performance of a*** $15°$ ***diffuser compared to a sharp leading edge, in terms of peak velocity, pressure distribution and downforce generated?*** The differences in velocity magnitude and C_P at the diffuser leading edge between the experiment of Battegazzore (sharp leading edge) and this experiment (rounded) shows there is a small increase in local streamwise velocity, as well as a decrease in C_P for the diffuser with the rounded leading edge. This is summarized in table 8.3.

Table 8.3: Velocity magnitude and C_P observed at the leading edge of a $15°$ diffuser

	rounded LE	**sharp LE**
u/U_∞	1.38	1.32
C_P	-0.85	-0.45

- ***How effectively can vortex generators delay or reduce separation inside a diffuser?*** As the diffuser without vortex generators did not show as large of a separation region as found by Battegazzore, one cannot answer directly if vortex generators are an effective method to reduce the large scale separation of a diffuser. Still, there is the indication of a laminar separation bubble being present at the plain diffuser, indicated by the lack of data around the diffuser leading edge. Since this data gap is not present for the diffuser with VG's, as well as the fact that the streamwise vortices move higher velocity air closer to the surface of the diffuser, it is reasonable to assume there is some effect on reducing separation inside a diffuser by adding a vortex generator strip near the diffuser leading edge.
- ***What is the effect of streamwise vortices within the diffuser in terms of peak velocity, pressure distribution and downforce generated?*** As shown already in tables 8.1 and 8.2, the streamwise vortices generated by the VG strip, there is no big effect on the magnitude of both the peak velocity as well as the local C_P observed at the diffuser leading edge. However, still important differences are observed, most notably the movement of high momentum air from middle part of the diffuser height towards the surface. The fact that the VG's transform some of the streamwise velocity into a rotational component might help with the reduction of separation regions, but they do not show a direct improvement in lowering the pressure underneath the model even further. This would suggest that there is not a direct benefit to adding the VG's to the $15°$ diffuser as tested in this experiment, in terms of downforce, which is driven by a lower pressure under the car.

8.1.4 Measuring vehicle downforce

As briefly touched upon, finding difference in downforce produced between different diffuser geometries is ultimately the goal of engineers trying to improve a race-car diffuser geometry. By integrating the pressure distribution underneath the car over the surface of the floor and diffuser, a first order estimation on the downforce produced by the car can be obtained. However, in order to relate the pressure underneath the car to an actual force value, the pressure difference between the upper and lower part of the vehicle is needed. As the flow over the top of the car is not measured in the experiment, it is impossible to calculate an accurate downforce figure.

Secondly, even though most of the domain underneath the car had good particle densities in the final binned datasets, the upper outboard corners of the diffuser lack particle information. Hence it is impossible to compute a pressure value in these areas using the integration method used in this thesis. Extrapolation of the available data will further increase the uncertainty of the pressure field.

Hence, this experiment is unable to directly answer the research questions about differences in downforce generated by the three test geometries. However, the C_P plots along the car centerline can give an indication about the working of the diffuser on the car, in terms of downforce. As the C_P around the diffuser leading edge is significantly lowered by the presence of the diffuser compared to the no diffuser model, one can see that there must be some form of downforce increase due to the diffuser. The difference between the model with and without VGs however is much smaller, and one cannot make a direct claim about more downforce being produced by one or the other.

Equipping the test model with surface pressure taps, as well as try to create a full circumferential measurement domain by adding cameras above the ground, can help with recreating the full flowfield around the car. This can then be processed to generate surface pressure data, allowing for a way of quantifying downforce figures, as well as other force components such as drag.

8.1.5 Uncertainty and convergence of the data

As this experiments main objective was to improve the setup used by Battegazzore, and demonstrate the capabilities of the Ring of Fire system in an automotive diffuser and underbody aerodynamics setting, it is important to focus on the research question from chapter 4, aiming at evaluating the accuracy of the Ring of Fire system in measuring critical aerodynamic characteristics of automotive diffusers. These questions were:

1. ***How many runs are needed to reach a mean flow velocity convergence within 1% of to the car's velocity?***

2. ***How accurate is the RoF setup in quantifying velocity and pressure distributions, as well as downforce figures for automotive applications?***

In terms of accuracy, the variance in the velocity profiles measured for the three car geometries showed a relative uncertainty in the order of 1.5% U_∞ for the flow upstream of the diffusers. At the diffuser leading edge and beyond, the relative uncertainty went up to about 6% of the freestream velocity. The measured uncertainties were small enough to measure the difference in peak velocity caused by putting a diffuser on the car model. The observed difference in velocity magnitude through the height of the diffuser, caused by the introduction of vortex generator fins at the diffuser leading edge is also outside the relative uncertainty measured in the diffuser.

For evaluating the pressure distribution around the car model, based on the velocity field data, a pressure gradient integration method was used. The uncertainty of this method stems from a relative error introduced by the integration scheme, as well as the uncertainty in estimating a base pressure coefficient C_P by applying Bernoulli's principle on the velocity field data. Combining these two uncertainties, the maximum relative C_P uncertainty was about 0.014. The measured pressure drop at the diffuser leading edge when introducing a diffuser, was in the order of 0.5 ΔC_P. This indicates the capability of the measurement system to capture the important large scale flow behaviors of automotive diffusers.

The data convergence analysis in section 7.3 assessed how the measured velocity field stabilizes as additional runs are included. By binning the particle track velocity data and evaluating the standard deviation of the mean velocity in a given bin, computed with a subset of the available tracks, the analysis quantified the impact of increasing the number of runs on convergence. Three points of interest (POIs) were examined: near the nose/floor leading edge, underneath the flat floor, and within the diffuser region.

The results showed that the Nose and Floor POIs reached a relative convergence threshold of 1% within approximately 4–5 runs, indicating that the mean velocity stabilized relatively quickly in these regions. However, the Diffuser POI required at least 23 runs to reach the same level of convergence. This was attributed to two primary factors: (1) increased velocity fluctuations within the diffuser, and (2) a lower number of tracked

particles per run in this region. The latter is due to flow expansion within the diffuser, which reduces particle density in the measurement volume. These findings highlight the need for a higher number of runs when studying complex flow regions such as diffusers.

The main uncertainty and convergence study outcomes are summarized in table 8.4 below. Please note that the mean velocity uncertainty is expressed as a percentage of the freestream velocity U_∞, and the uncertainty of C_P is expressed as an absolute value around C_P.

Table 8.4: Overview of the measurement uncertainties and convergence of the data

	Nose	**Floor**	**Diffuser**
Relative mean velocity uncertainty $\epsilon_{\bar{u}}$	1.5%	1.5%	6%
C_P **uncertainty** σ_{C_P}	0.09	0.07	0.12
Runs needed to reach 1% convergence	5	5	25

8.2 Recommendations and improvements

This study successfully demonstrated the application of on-site 3D Lagrangian Particle Tracking (LPT) for analyzing underbody aerodynamics using the Ring of Fire (RoF) setup. While the methodology provided valuable insights into diffuser flow behavior, several limitations remain, particularly regarding scalability, accuracy, and the feasibility of direct downforce measurements. This section outlines key improvements that could enhance the experimental setup for larger-scale applications, improve measurement precision, and explore potential methods for extracting direct aerodynamic force data.

8.2.1 Scalability for larger vehicles

The current on-site RoF setup using the facility at the Delft University of Technology (TU Delft) is reaching the limits in terms of scalability of the test vehicles. In order to facilitate larger vehicles, at higher speeds to increase the Reynolds number at which the testing is conducted, several modifications can be implemented:

- **Increase subterranean camera and illumination container**: In order to allow for a larger measurement volume, increasing the size of the concrete shell or other container below ground-level can be beneficial. Making the cameras sit deeper in the ground allows for a larger focal distance, and a wider field of view, if the walls of the container are not blocking it. Next to increasing the cameras field of view, when scaling the measurement volume one needs to ensure proper illumination of particles. This most likely requires an increase in light sources, which need to fit in the shell under the ground.

- **Improve seeding container size**: The tent used for the experiment of this thesis proved sufficient for the size of the car model used. However, if one wants to consider testing a full scale vehicle, the tent width of around 3m does not allow for safe high speed driving of such vehicles. Increasing the size of the tent further does need rechecking with the current seeding rig if a sufficient HFSB density can be obtained in the entire tent.

- **Road preparation and run-off**: The concrete shell at the TU Delft is located in a closed area behind the high-speed laboratory. It has a poor road surface consisting of small bricks, and is far from flat. A small run-off area of length 30m is present after the concrete shell, severely limiting car braking distance. In order to allow for high speed driving, a much larger facility needed. An actual automotive track or car park, fully paved with flat concrete or tarmac, would be ideal for high speed testing with full-scale vehicles.

8.2.2 Improving measurement accuracy

When looking at the accuracy of the measurements, several improvements can be made in order to further develop the capabilities of the setup:

- Adding more cameras to the measurement setup: When one plans to increase the measurement volume, and size of the vehicles tested, increasing the number of cameras used for image acquisition can be beneficial. Evaluating more challenging geometries than the plain diffusers tested in this setup can create blind spots for cameras in certain viewpoints. This effect is already visible in the current setup where the particle tracking in the outboard corners of the diffuser is limited. The vertical side walls of the

diffuser block part of the image for the outboard cameras, hence particle tracking capabilities is reduced. Together with a larger camera container, more cameras would allow for much more complex geometries to be reliable captured and tracked.

- **Model painting and preparation** Even with the image preprocessing steps taken described in chapter 6, light reflections from the soap covered tires and some other parts of the bodywork persisted in the images. When scaling to a larger vehicle, more car components might introduce reflections, such as metallic suspension members, non-painted bodywork panels, bolt heads, etc. Having a system that can clean the tires after each run might keep the transparent panel clean from tire marks, for cars where the tires pass through the measurement domain.
- **Improved Pressure Calculation Methods** The pressure field is calculated with the pressure gradient integration method described in chapter 6. Using a different pressure integration scheme, such as the omnidirectional scheme described by Liu and Moreto [38], has been proven to reduce errors introduced by the numerical integration. A Poisson solver will require a more complex setup in terms of boundary condition handling [36], but might still be valuable in order to validate the pressures obtained through the pressure integration methods.

Bibliography

[1] Douglas L. Milliken and William F. Milliken. *Race car vehicle dynamics: problems, answers, and experiments*. English. [Rev. ed.] Section: xiii, pages 280 : illustrations ; 26 cm + 1 CD-ROM (4 3/4 in.) Warrendale, PA: SAE International, 2003. ISBN: 978-0-7680-1127-2.

[2] W. Toet. "Aerodynamics and aerodynamic research in Formula 1". en. In: *The Aeronautical Journal* 117.1187 (Jan. 2013), pp. 1–26. ISSN: 0001-9240, 2059-6464. DOI: 10.1017/S0001924000007739. URL: https://www.cambridge.org/core/product/identifier/S0001924000007739/type/journal_article.

[3] G Sovran. "The kinematic and fluid-mechanic boundary conditions in underbody flow simulation". In: *Proceedings of the CNR-pininfarina workshop on wind tunnel simulation of ground effect*. National Research Council, Turin, 1994.

[4] Kevin R. Cooper et al. "The Aerodynamic Performance of Automotive Underbody Diffusers". In: *SAE Transactions* 107 (1998). Publisher: SAE International, pp. 150–179. ISSN: 0096-736X. URL: https://www.jstor.org/stable/44740947.

[5] Andrea Elizabeth Senior. "The aerodynamics of a diffuser equipped bluff body in ground effect". en. phd. University of Southampton, 2002. URL: https://eprints.soton.ac.uk/47113/ (visited on 05/15/2024).

[6] A. R. George. "Aerodynamic Effects of Shape, Camber, Pitch, and Ground Proximity on Idealized Ground-Vehicle Bodies". In: *Journal of Fluids Engineering* 103.4 (Dec. 1981), pp. 631–637. ISSN: 0098-2202. DOI: 10.1115/1.3241783. URL: https://doi.org/10.1115/1.3241783.

[7] Daniel Schanz, Sebastian Gesemann, and Andreas Schröder. "Shake-The-Box: Lagrangian particle tracking at high particle image densities". en. In: *Experiments in Fluids* 57.5 (Apr. 2016), p. 70. ISSN: 1432-1114. DOI: 10.1007/s00348-016-2157-1. URL: https://doi.org/10.1007/s00348-016-2157-1.

[8] Alexander Spoelstra et al. "On-site cycling drag analysis with the Ring of Fire". en. In: *Experiments in Fluids* 60.6 (June 2019), p. 90. ISSN: 0723-4864, 1432-1114. DOI: 10.1007/s00348-019-2737-y. URL: http://link.springer.com/10.1007/s00348-019-2737-y.

[9] Andrea Battegazzore, Adrian Grille Guerra, and Andrea Sciacchitano. "On-Site Characterization of Automotive Diffuser Aerodynamics by 3D LPT". In: *Proceedings of the International Symposium on the Application of Laser and Imaging Techniques to Fluid Mechanics* 21 (July 2024), pp. 1–13. DOI: 10.55037/lxlaser.21st.62.

[10] Joseph Katz. "Aerodynamics in motorsports". en. In: *Proceedings of the Institution of Mechanical Engineers, Part P: Journal of Sports Engineering and Technology* 235.4 (Dec. 2021), pp. 324–338. ISSN: 1754-3371, 1754-338X. DOI: 10.1177/1754337119893226. URL: http://journals.sagepub.com/doi/10.1177/1754337119893226.

[11] S. R. Ahmed, G. Ramm, and G. Faltin. "Some Salient Features of the Time -Averaged Ground Vehicle Wake". In: *SAE Transactions* 93 (1984). Publisher: SAE International, pp. 473–503. ISSN: 0096-736X. URL: https://www.jstor.org/stable/44434262.

[12] Jesper Marklund. *Under-body and diffuser flows of passenger vehicles*. eng. Doktorsavhandlingar vid Chalmers Tekniska Högskola N.S., 3547. Göteborg: Chalmers Univ. of Technology, 2013. ISBN: 978-91-7385-866-3.

[13] Andreas Ruhrmann and Xin Zhang. "Influence of Diffuser Angle on a Bluff Body in Ground Effect". In: *Journal of Fluids Engineering* 125.2 (Mar. 2003), pp. 332–338. ISSN: 0098-2202. DOI: 10.1115/1.1537252. URL: https://doi.org/10.1115/1.1537252.

[14] L Jowsey and M Passmore. "Experimental study of multiple-channel automotive underbody diffusers". en. In: *Proceedings of the Institution of Mechanical Engineers, Part D: Journal of Automobile Engineering* 224.7 (July 2010), pp. 865–879. ISSN: 0954-4070, 2041-2991. DOI: 10.1243/09544070JAUTO1339. URL: http://journals.sagepub.com/doi/10.1243/09544070JAUTO1339.

[15] Lydia Jowsey. "An Experimental Study of Automotive Underbody Diffusers". en. PhD thesis. Loughborough: Loughborough University, 2013. URL: https://core.ac.uk/download/pdf/288380215.pdf.

[16] O. H. Ehirim, K. Knowles, and A. J. Saddington. "A Review of Ground-Effect Diffuser Aerodynamics". en. In: *Journal of Fluids Engineering* 141.2 (Feb. 2019), p. 020801. ISSN: 0098-2202, 1528-901X. DOI: 10.1115/1.4040501. URL: https://asmedigitalcollection.asme.org/fluidsengineering/article/doi/10.1115/1.4040501/368866/A-Review-of-GroundEffect-Diffuser-Aerodynamics.

[17] Andrea Senior and Xin Zhang. "An experimental study of a diffuser in ground effect". en. In: *38th Aerospace Sciences Meeting and Exhibit*. Reno,NV,U.S.A.: American Institute of Aeronautics and Astronautics, Jan. 2000. DOI: 10.2514/6.2000-118. URL: https://arc.aiaa.org/doi/10.2514/6.2000-118.

[18] Andrea E. Senior and Xin Zhang. "The Force and Pressure of a Diffuser-Equipped Bluff Body in Ground Effect". In: *Journal of Fluids Engineering* 123.1 (Oct. 2000), pp. 105–111. ISSN: 0098-2202. DOI: 10.1115/1.1340637. URL: https://doi.org/10.1115/1.1340637.

[19] Xin Zhang, Willem Toet, and Jonathan Zerihan. "Ground Effect Aerodynamics of Race Cars". en. In: *Applied Mechanics Reviews* 59.1 (Jan. 2006), pp. 33–49. ISSN: 0003-6900, 2379-0407. DOI: 10.1115/1.2110263. URL: https://asmedigitalcollection.asme.org/appliedmechanicsreviews/article/59/1/33/450607/Ground-Effect-Aerodynamics-of-Race-Cars.

[20] *Andretti still working towards 2025 F1 debut as tunnel model revealed*. en. Jan. 2024. URL: https://www.motorsport.com/f1/news/andretti-still-working-towards-2025-f1-debut-tunnel-model-revealed/10570624/ (visited on 12/03/2024).

[21] Jesper Marklund and Lennart Lofdahl. "Drag Reduction of a Simple Bluff Body by Changing the Rear End and Use the Ground Effect". In: *Volume 2: Fora*. Vail, Colorado, USA: ASMEDC, Jan. 2009, pp. 291–296. DOI: 10.1115/FEDSM2009-78502. URL: https://asmedigitalcollection.asme.org/FEDSM/proceedings/FEDSM2009/43734/291/333092.

[22] Andreas Schröder and Daniel Schanz. "3D Lagrangian Particle Tracking in Fluid Mechanics". en. In: *Annual Review of Fluid Mechanics* 55.1 (Jan. 2023), pp. 511–540. ISSN: 0066-4189, 1545-4479. DOI: 10.1146/annurev-fluid-031822-041721. URL: https://www.annualreviews.org/doi/10.1146/annurev-fluid-031822-041721.

[23] Ronald J. Adrian and Jerry Westerweel. *Particle Image Velocimetry*. en. Cambridge University Press, 2011. ISBN: 978-0-521-44008-0.

[24] G. E. Elsinga et al. "Tomographic particle image velocimetry". en. In: *Experiments in Fluids* 41.6 (Dec. 2006), pp. 933–947. ISSN: 1432-1114. DOI: 10.1007/s00348-006-0212-z. URL: https://doi.org/10.1007/s00348-006-0212-z.

[25] Jerry Westerweel, Gerrit E. Elsinga, and Ronald J. Adrian. "Particle Image Velocimetry for Complex and Turbulent Flows". en. In: *Annual Review of Fluid Mechanics* 45.1 (Jan. 2013), pp. 409–436. ISSN: 0066-4189, 1545-4479. DOI: 10.1146/annurev-fluid-120710-101204. URL: https://www.annualreviews.org/doi/10.1146/annurev-fluid-120710-101204.

[26] Fulvio Scarano et al. "On the use of helium-filled soap bubbles for large-scale tomographic PIV in wind tunnel experiments". en. In: *Experiments in Fluids* 56.2 (Feb. 2015), p. 42. ISSN: 1432-1114. DOI: 10.1007/s00348-015-1909-7. URL: https://doi.org/10.1007/s00348-015-1909-7.

[27] W. Terra, A. Sciacchitano, and F. Scarano. "Aerodynamic drag of a transiting sphere by large-scale tomographic-PIV". en. In: *Experiments in Fluids* 58.7 (June 2017), p. 83. ISSN: 1432-1114. DOI: 10.1007/s00348-017-2331-0. URL: https://doi.org/10.1007/s00348-017-2331-0.

[28] Alexander Spoelstra, Wouter Terra, and Andrea Sciacchitano. "On-site aerodynamics investigation of speed skating". In: *Journal of Wind Engineering and Industrial Aerodynamics* 239 (Aug. 2023), p. 105457. ISSN: 0167-6105. DOI: 10.1016/j.jweia.2023.105457. URL: https://www.sciencedirect.com/science/article/pii/S0167610523001605.

[29] Steffen Hüttig et al. "Automotive on-road flow quantification with a large scale Stereo-PIV set-up". en. In: Accepted: 2023-07-04T12:39:09Z. International Symposium on Particle Image Velocimetry, June 2023. URL: https://reposit.haw-hamburg.de/handle/20.500.12738/13938.

[30] B. Wieneke. "Volume self-calibration for 3D particle image velocimetry". en. In: *Experiments in Fluids* 45.4 (Oct. 2008), pp. 549–556. ISSN: 1432-1114. DOI: 10.1007/s00348-008-0521-5. URL: https://doi.org/10.1007/s00348-008-0521-5.

[31] D. Schanz et al. "Particle Reconstruction with Optical Transfer Functions Applied to Tomo-PIV-Experiments". en. In: *New Results in Numerical and Experimental Fluid Mechanics VIII: Contributions to the 17th STAB/DGLR Symposium Berlin, Germany 2010*. Ed. by Andreas Dillmann et al. Berlin, Heidelberg: Springer, 2013, pp. 623–631. ISBN: 978-3-642-35680-3. DOI: 10.1007/978-3-642-35680-3_74. URL: https://doi.org/10.1007/978-3-642-35680-3_74.

[32] Andrea Sciacchitano and Fulvio Scarano. "Elimination of PIV light reflections via a temporal high pass filter". en. In: *Measurement Science and Technology* 25.8 (Aug. 2014), p. 084009. ISSN: 0957-0233, 1361-6501. DOI: 10.1088/0957-0233/25/8/084009. URL: https://iopscience.iop.org/article/10.1088/0957-0233/25/8/084009.

[33] Laura Porcar Galan et al. "Light Reflections Detection And Correction For Robotic Volumetric PIV". en. In: *Proceedings of the International Symposium on the Application of Laser and Imaging Techniques to Fluid Mechanics* 21 (July 2024), pp. 1–19. DOI: 10.55037/lxlaser.21st.59. URL: https://www.lisbonsymposia.org/21stlxsymp2024/piv-data-assimilation/59.

[34] Sagar Adatrao and Andrea Sciacchitano. "Elimination of unsteady background reflections in PIV images by anisotropic diffusion". en. In: *Measurement Science and Technology* 30.3 (Mar. 2019), p. 035204. ISSN: 0957-0233, 1361-6501. DOI: 10.1088/1361-6501/aafca9. URL: https://iopscience.iop.org/article/10.1088/1361-6501/aafca9.

[35] Nereida Agüera et al. "Ensemble 3D PTV for high resolution turbulent statistics". en. In: *Measurement Science and Technology* 27.12 (Dec. 2016), p. 124011. ISSN: 0957-0233, 1361-6501. DOI: 10.1088/0957-0233/27/12/124011. URL: https://iopscience.iop.org/article/10.1088/0957-0233/27/12/124011.

[36] B W van Oudheusden. "PIV-based pressure measurement". en. In: *Measurement Science and Technology* 24.3 (Jan. 2013). Publisher: IOP Publishing, p. 032001. ISSN: 0957-0233. DOI: 10.1088/0957-0233/24/3/032001. URL: https://dx.doi.org/10.1088/0957-0233/24/3/032001.

[37] Xiaofeng Liu and Joseph Katz. "Instantaneous pressure and material acceleration measurements using a four-exposure PIV system". en. In: *Experiments in Fluids* 41.2 (Aug. 2006), pp. 227–240. ISSN: 1432-1114. DOI: 10.1007/s00348-006-0152-7. URL: https://doi.org/10.1007/s00348-006-0152-7.

[38] Xiaofeng Liu and Jose Roberto Moreto. "Error propagation from the PIV-based pressure gradient to the integrated pressure by the omnidirectional integration method". en. In: *Measurement Science and Technology* 31.5 (Feb. 2020). Publisher: IOP Publishing, p. 055301. ISSN: 0957-0233. DOI: 10.1088/1361-6501/ab6c28. URL: https://dx.doi.org/10.1088/1361-6501/ab6c28.

[39] Jinhee Jeong and Fazle Hussain. "On the identification of a vortex". en. In: *Journal of Fluid Mechanics* 285 (Feb. 1995), pp. 69–94. ISSN: 1469-7645, 0022-1120. DOI: 10.1017/S0022112095000462. URL: https://www.cambridge.org/core/journals/journal-of-fluid-mechanics/article/on-the-identification-of-a-vortex/D26006DDB95FB28DA80E28A581182DF1.

A. Particle transformation code

```
# -*- coding: utf-8 -*-
'''
Pseudo code to transform particle track data from lab frame to car static reference frame

For each run:
  Loads run marker and particle track files
    Match particle track data to predefined marker sequence painted on the car
      Extract car velocity and position at t_ref
    Transform full set of particle track data using known car velocity and position at t_ref
  Save transformed particle track file with tracks in car static reference frame
'''

import Marker_Finding_main as mf
import Transform_dat_file as td
import os

def process_marker_data(file_path_markers, minpart=3, tresholdx=10, marker_id=10, tolerance=1.3, min_consecutive=2):
    """
    Process marker data to find the longest consecutive sequence of a specific marker.
    Checks each timestep for marker tracks, and tries to match their relative distances to a predefined marker sequence in which the markers are painted on the car model.

    Inputs:
    file_path_markers         # Location of marker particle track file
    marker_id                 # Marker from the sequence to be tracked as the car origin
    minpart                   # Minimum number of particles per timestep needed to try and find a match to the marker sequence
    tresholdx                 # Maximum deviation of a particle allowed with respect to the theoretically straight line of the marker sequence [mm]
    tolerance                 # Maximum deviation in relative particle distances allowed with respect to the marker sequence [mm]
    min_consecutive           # Minimum number of consecutive frames for which the sequence needs to be matched for the 'matching' to be accepted

    Returns:
    longest_consec_match      # Longest consecutive timesteps for which marker_id is found
    track_id                  # Particle track ID assigned by Davis to the marker_id
    """

    cleanfull = mf.load_data(file_path_markers) # Load all marker data from specific run

    blocklength, snapshotlist, timesteps = mf.extract_timesteps(cleanfull, totalsteps=1000) # Break file into single blocks of data per timestep
    snapshotlist_filtered, timesteps_filtered = mf.filter_timesteps(timesteps, snapshotlist, blocklength, minpart, tresholdx, totalsteps=1000)  # Filter any timesteps that have marker tracks that are outside the set minpart and tresholdx
    track_marker_mapping = mf.find_matching_sequences(timesteps_filtered, snapshotlist_filtered, tolerance)        # Try to fit the predefined marker sequence to the filtered timesteps
    longest_consec_match, track_id = mf.find_consecutive_matches(track_marker_mapping, marker_id, min_consecutive) # Filter out the longest consecutive sequence of timesteps containing marker_id

    return longest_consec_match, track_id

def process_velocity_and_transform(file_path_markers, file_path_bubbles, track_id, longest_consec_match, transformed_output_file):
    """
```

```
    Compute the average velocity of the selected track and transform bubble data accordingly.

    Inputs:
    file_path_markers        # Location of marker particle track file
    file_path_bubbles        # Location of full run particle track file
    track_id                 # Particle track ID corresponding to the car origin marker
    longest_consec_match     # Longest consecutive timesteps for which marker_id is found
    transformed_output_file  # Location to save transformed particle track data

    Returns:
    Transformed particle track file saved to transformed_output_file location
    """

    # Read marker data, and extract the average velocity of the car origin marker based on its
     track_id
    particle_data = td.parse_particle_tracks(file_path_markers)
    avg_vx, avg_vy, avg_vz, last_coordinates = td.filter_track_data(particle_data, track_id,
    longest_consec_match)


    if last_coordinates:
        target_snapshot_index = longest_consec_match[-1]               # Set timestep to fix
    car origin
        bubbles_data = td.parse_particle_tracks(file_path_bubbles)     # Load particle tracks
        transformed_data = td.transform_particle_data(                 # Transform particle
    tracks to car static reference frame
            bubbles_data, {'Vx': avg_vx, 'Vy': avg_vy, 'Vz': avg_vz}, last_coordinates,
    target_snapshot_index
        )
        td.write_transformed_data_to_file(transformed_data, file_path_bubbles,
    transformed_output_file)  # Write transformed particle track file
    else:
        print(f"No valid last coordinates for TrackID {track_id}, transformation skipped.")

def main(mainpath, runfolder, savepath, runlist):
    """
    Main function to process multiple runs by extracting marker data and transforming particle
     tracks to car static reference frame.

    Inputs:
    mainpath                # Main directory holding the 3D LPT data
    runfolder               # Directory in which marker and particle files are stored per run
    savepath                # Path to save transformed particle tracks
    runlist                 # List of run's to process within the mainpath

    Returns:

    """
    savefolder = os.path.join(savepath, runfolder)
    os.makedirs(savefolder, exist_ok=True)

    # Setup folders and names for run processing
    for run in runlist:
        runpath = os.path.join(runfolder, f"{runfolder}_Run{run}")
        folder = os.path.join(mainpath, runpath)

        file_path_markers = os.path.join(folder, "_Markers/ShakeTheBox Markers.dat")
        file_path_bubbles = os.path.join(folder, "_Bubbles/ShakeTheBox-MedianFilter.dat")
        transformed_output_file = os.path.join(savefolder, f"Run{run}_bubbles_transformed_v2.
    dat")

        print(f"Processing {run}...")

        longest_consec_match, track_id = process_marker_data(file_path_markers)
        if longest_consec_match:
            process_velocity_and_transform(file_path_markers, file_path_bubbles, track_id,
    longest_consec_match, transformed_output_file)
        else:
            print(f"No valid marker sequence found for Run {run}.")

mainpath = "Example/Davis/STB data/"
runfolder = "Day01_HE_NoDiff"
savepath = "Example/Davis/STB transformed/"
```

```
110 runlist = ["01", "02", "03", "04", "05", "06", "07", "08", "09", "10"]
111
112 main(mainpath, runfolder, savepath, runlist)
```